AN EXPERIMENTALLY VALIDATED HEAT EXCHANGER REFRIGERANT CHARGE MODEL AND OPTIMIZATION OF REFRIGERANT CHARGE FOR A HEAT PUMP

By

ABRAHAM JUSEOK LEE

Bachelor of Science in Mechanical Engineering
Korea University
Seoul, South Korea
2008

Master of Science in Mechanical Engineering
Korea University
Seoul, South Korea
2010

Submitted to the Faculty of the
Graduate College of the
Oklahoma State University
in partial fulfillment of
the requirements for
the Degree of
DOCTOR OF PHILOSOPHY
May, 2023

AN EXPERIMENTALLY VALIDATED HEAT EXCHANGER REFRIGERANT CHARGE MODEL AND OPTIMIZATION OF REFRIGERANT CHARGE FOR A HEAT PUMP

Dissertation Approved:

Dr. Craig R. Bradshaw

Dissertation Adviser

Dr. Christian K. Bach

Dr. He Bai

Dr. Aaron Alexander

ACKNOWLEDGMENTS

First and foremost, I would like to extend my deepest gratitude to Jesus who saved my life and led me to Stillwater (Psalm 23:2 in KJV).

I would like to thank my wife, Seulgi, and my two daughters, Sarang and Eunhye, and my parents for their support and encouragement throughout my academic pursuits. Your patience, understanding, and sacrifice have been the driving force behind my success.

To my advisors, Dr. Christian Bach and Dr. Craig Bradshaw, thank you for your guidance, mentorship, and unwavering support. Your expertise, constructive criticism, and encouragement have helped me to shape my research and achieve my academic goals.

To my committee members, Dr. Aaron Alexander and Dr. He Bai, thank you for your valuable insights, feedback, and supports.

I would also like to acknowledge my labmates and friends at OSU, who have made my academic journey more enjoyable and meaningful. Your support and friendship have made a significant impact on me, and I am grateful for your presence in my life.

Finally, I would like to express my appreciation to all those who have supported me directly or indirectly. Your contributions have been invaluable, and I am grateful for your impact on my academic journey.

Acknowledgments reflect the views of the author and are not endorsed by committee members or Oklahoma State University.

Name: ABRAHAM JUSEOK LEE

Date of Degree: MAY, 2023

Title of Study: AN EXPERIMENTALLY VALIDATED HEAT EXCHANGER REFRIGERANT CHARGE MODEL AND OPTIMIZATION OF REFRIGERANT CHARGE FOR A HEAT PUMP

Major Field: MECHANICAL AND AEROSPACE ENGINEERING

Abstract: Refrigerant charge affects the efficiency, capacity, and reliability of a heat pump, and incorrect charge can lead to increased energy consumption and decreased performance as well as potential damage to the system. Furthermore, refrigerant charge has an environmental impact, with high Global Warming Potential (GWP) refrigerants contributing to climate change. The HVAC&R society is adopting low-GWP refrigerants to alleviate the concern. For these reasons, accurate prediction of refrigerant charge is vital in designing heat pumps, particularly for low-GWP refrigerants; this charge prediction is done by charge models.

Meanwhile, existing charge models are limited in their charge prediction accuracy due to uncertainty in void-fraction models the charge models rely on for charge prediction. Experimental charge validation data can improve the accuracy of the charge model, but such data for low-GWP refrigerant charge is rare in the open literature.

The goal of this study is to address the issue by improving the accuracy of charge prediction; that is done by creating a high-accuracy charge model that is verified by experimental charge validation data. To gather this experimental charge data, a novel charge measurement method and charge measurement facility for measuring charge is created, resulting in high-fidelity experimental charge data for heat exchangers across various operating conditions of heat pumps. This database includes multiple refrigerants, including low-GWP refrigerants, R1234yf and R468C, and additional R410A as a reference. Employing this experimental data, a high-accuracy charge model is developed and validated, which is used to optimize the charge and cooling capacity of a heat pump simultaneously on a developed multi-objective optimization framework.

TABLE OF CONTENTS

Chapter Page

Chapter Page

LIST OF TABLES

Table Page

Table Page

LIST OF FIGURES

Figure Page

Figure Page

Figure Page

Figure Page

ABBREVIATIONS

ACHP	Air Conditioning Heat Pump
ACRS	Air Conditioning and Refrigeration Systems
AHRI	Air Conditioning, Heating and Refrigeration Institute
ANN	Artificial Neural Network
ASHRAE	American Society of Heating, Refrigeration and Air Conditioning Engineers
ASME	American Society of Mechanical Engineers
BPHX	Brazed Plate Heat Exchanger
CFD	Computational Fluid Dynamics
CIBS	Center for Integrated Building Systems
CND	Condenser
COP	Coefficient of Performance
CW	Charge Sampled Weight
DAQ	Data Acquisition System
DB	Dry Bulb
DMMS	Differential Mass Measurement Scale
EES	Engineering Equation Solver
EVA	Evaporator
EXV	Expansion Valve
FPI	Fins Per Inch
GA	Genetic Algorithm
GWP	Global Warming Potential

HFC	Hydro-Fluoro-Carbon
HFO	Hydro-Fluoro-Olefin
HP	Heat Pump
HVAC	Heating, Ventilation and Air Conditioning
HVAC&R	Heating, Ventilation, Air Conditioning, and Refrigeration
IC	Indoor Coil (Heat Exchanger)
MAPE	Mean Absolute Percentage Error
MDA	Modular Duct Assembly
NIST	National Institute of Standards and Technology
NSGA-II	Non-Dominated Sorting Genetic Algorithm-II
NTU	Number of Transfer Unit
OC	Outdoor Coil (Heat Exchanger)
OD	Outside Diameter
OLS	Ordinary Least Squares
OM	Online Measurement Method
POE	Polyolester
RBF	Radial Basis Function
RH	Relative Humidity
RHXCT	Removable Heat Exchanger Charge Test Module
RMSE	Root-Mean-Square Error
RSV	Rapid Shut-Off Valve
RTD	Resistance Temperature Detector
RTPF	Round-Tube-Plate-Fin Heat Exchanger
SFCVT	Space-Filling Cross-Validation Tradeoff Method
SST	Saturated Suction Temperature
SM	Sampling Measurement Method
TW	Tare Weight

VMD	Volume-Measurement Device
WB	Wet Bulb
XFIN	In-House Heat Exchanger Model

NOMENCLATURE

VARIABLES	UNITS	DESCRIPTION
A	m^2	Area
b	-	Bias in ANN
C	-	Correction factor
c	kJ/(kg·K)	Specific heat capacity of air
G	kg/m^2·s	Mass flux
g	m/s^2	Acceleration of gravity
h	kJ/kg	Enthalpy
m	g	Charge mass unless otherwise specified
$\dot{m}$	kg/s, kg/hr	Mass flow rate
Δm	g	Mass difference
P	kPa	Pressure in absolute value, Parent population
Q	-	Offspring population
$\dot{Q}$	kW	Capacity
R	kJ/(kg·K)	Nitrogen gas constant, Combined population
r	-	Pearson correlation coefficient
Re	-	Reynolds number
SC	K	Subcooling
SH	K	Superheat
T	°C	Temperature
u	-	Uncertainty
V	m^3	Volume

w	-	Weight in ANN
We	-	Weber number
x	-	Quality
X	K	Input variable

GREEK SYMBOLS	UNITS	DESCRIPTION
α	-	Void fraction, Coefficient
β	-	Coefficient
ϵ	-	Effectiveness
η	-	Efficiency
μ	$\mathrm{Pa} \cdot \mathrm{s}$	Dynamic viscosity
ρ	$\mathrm{kg/m^3}$	Density
σ	N/m	Surface tension
φ	-	Radial basis function
Φ	-	Interpolation matrix

SUBSCRIPTS	DESCRIPTION
a, air	Air
atm	Atmosphere
aux	Auxiliary
cap	Capillary tube
$const$	Constant
cnd	Condenser
cw	Charge-sampled weight
db	Dry bulb
dry	Tare-weight state
end	End state

evp	Evaporator
f, l	Saturated liquid
g, v	Saturated vapor
i, in	Inlet, internal
liq	Liquid state
min	Minimum
o, out	Outlet
oil	POE Oil
off	Offset weight
$original$	Original
r, ref	Refrigerant
$regress$	Regression
rel	Relative value
sat	Saturated state
sc	Subcooling
sh	Superheat
$start$	Initial
sys	System
tot	Total
tp	Two-phase state
tw	Tare weight
vap	Superheated vapor state
wb	Wet bulb

CHAPTER I

INTRODUCTION

1.1 Overview

The demand for energy-efficient and environmentally-favorable Heating, Ventilation, and Air Conditioning (HVAC) systems has been growing over the past decades (Chua et al., 2013). Heat pumps are one of the most efficient HVAC systems that satisfies the needs. The heat pumps can support both cooling and heating and provide a couple of advantages, for instance, low-carbon foot prints, cost-effective running costs, and less maintenance (Chua et al., 2010).

The heat pumps are greatly affected by the refrigerant charge, which is the amount of refrigerant in the system. In other words, incorrect refrigerant charge can yield low efficiency and decreased capacity of a heat pump. An undercharged or overcharged system can cause suboptimal operation and increased energy consumption (Proctor, 1997; Goswami et al., 2001).

In addition to the performance of heat pumps, reliability of heat pumps is also affected by the refrigerant charge. When a heat pump switches the mode between cooling and heating, improper charge in the heat pump can result in a damage of the system by a charge migration (Eom et al., 2019). Another issue owing to the charge migration is a compressor failure during the off-cycle. Some refrigerant can be drawn to the compressor then saturate the oil; therefore, the compressor loses a capability of lubrication of its moving components, thus requiring an oil sump heater (Scire, 1968). Moreover, if the refrigerant charge is excessive, it can bring about an overloading of

the compressor and other components, thus causing potential damage to the system (Poggi et al., 2008). These factors demonstrate the importance of refrigerant charge in a heat pump operation.

Refrigerant charge in heat pumps is also significant in environmental impact, particularly in terms of their Global Warming Potential (GWP) (Heath, 2017). The GWP indicates the relative impact of a refrigerant to global warming compared to carbon dioxide, which has a GWP of 1. High-GWP refrigerants such as HydroFluoroCarbons (HFCs) are potent greenhouse gases, with a GWP up to thousands of times greater than carbon dioxide; therefore their contribution to climate change has become a notable concern (McLinden et al., 2017).

Historically, the Montreal Protocol, an international agreement signed in 1987, targeted to decrease the production and consumption of ozone-depleting substances, including some high-GWP refrigerants. Meanwhile, as HFCs became a common replacement for ozone-depleting refrigerant, it became obvious that their high-GWP properties needed to be addressed as well. The Kigali Amendment to the Montreal Protocol, agreed upon in 2016, summarizes a plan to phase out the use of HFCs and replace them with low-GWP refrigerants (Heath, 2017). To keep up with the regulation, the Heating, Ventilation, Air-conditioning, and Refrigeration (HVAC&R) society has been rapidly adopting low-GWP refrigerants (Wu et al., 2021).

Because of the significance of refrigerant charge, it has become essential to accurately predict refrigerant charge in a heat pump. However, due to the limitations of experimental evaluations of refrigerant charge in heat pumps, refrigerant charge analysis heavily relies on charge modeling tools (Ding et al., 2009). In other words, accurately predicting an optimal refrigerant charge in a heat pump needs a high-accuracy refrigerant charge model. For a counter example, non-optimal charge determined by the inaccurate charge model could result in degradation of performance and Coefficient of Performance (COP) of a vapor-compression system: an undercharge of 20%

from the optimal charge causes COP reduction of 8.2% and cooling capacity degradation of 14.2% in an automotive air conditioning system (Yin et al., 2021); and, Kim and Braun (2012) presented 25% of charge deficiency leads to a capacity reduction of 20% in a heat pump. In consequence, the accuracy of the charge model affects the capacity, efficiency, and reliability of a heat pump, thus resulting in demand of a development of a high-accuracy refrigerant charge model; particularly for low-GWP refrigerants.

Meanwhile, current refrigerant charge models are limited in their charge prediction accuracy while predicting charge inside heat exchangers due to the uncertainty of void fraction in the two-phase (Harms et al., 2003). For these reasons, the charge models lean on void-fraction models to estimate the charge in the two-phase refrigerant. Yet, the majority of the void-fraction models were developed without considering the actual operating condition of heat exchangers; for instance, some void-fraction models utilized straight tube configuration with water or steam as the working fluids. Some of them were developed even under adiabatic condition. As a result, the existing void-fraction models might not always produce good charge prediction in heat pump applications (Shen et al., 2006).

In that regard, an experimental charge validation data can provide sufficient information to improve an accuracy of the charge models. Meanwhile, there are few experimental charge validation data available in the open literature, see Section 2.1, thus challenging in developing a high-accuracy refrigerant charge model. Accordingly, there is a need to conduct comprehensive experimental studies to obtain high-fidelity refrigerant charge validation data.

Furthermore, while several low-GWP refrigerants have been proposed, their charge validation data is very limited in the open literature, see Section 3.1. Hence, experimental charge validation data for low-GWP refrigerants can significantly contribute to improving the charge model as well as enabling effective and reliable design of heat

pumps given the influence of charge in heat pumps, which will facilitate adoption of low-GWP refrigerants.

In conclusion, the literature review implies that refrigerant charge in a heat pump can be optimized based on the improved charge model by the experimental charge data, thus leading to optimal performance and efficiency of a heat pump. In addition, the proper refrigerant charge results in reducing the risk of system failure and energy consumption, and lowering operating costs while increasing system reliability.

1.2 Research Objectives

The previous literature review criticized the insufficient accuracy of charge models given the significance of refrigerant charge in heat pumps. This research targets with the following objectives:

- Developing high-fidelity charge measurement method and facility
- Providing high-quality experimental charge validation data
- Evaluating and improving a charge model
- Developing a framework for optimization of charge for a heat pump

1.3 Outline

The research objectives are concretized in this dissertation. A summary of outline of each of the following chapters are as follows:

- Chapter 2 details a novel charge measurement method and an associated high-reliability charge measurement facility as well as an obtained experimental charge validation data for R410A refrigerant

- Chapter 3 presents an experimental charge validation data for low-GWP refrigerants, R1234yf and R468C, and a high-accuracy tuned charge model by the obtained high-fidelity experimental data.

- Chapter 4 describes a development of multi-objective optimization framework to optimize charge and cooling capacity of a heat pump simultaneously.

- Chapter 5 explains a dissertation summary and overall conclusions as well as future work.

CHAPTER II

EXPERIMENTAL VALIDATION OF REFRIGERANT CHARGE MODELS IN ROUND-TUBE-PLATE-FIN HEAT EXCHANGERS

Abstract

Charge modeling tools require high-fidelity experimental validation data to tune their predictions. The presented study provides a set of, high-quality, R410A experimental charge data to address this need. The experimental data includes a total of 42 tests of refrigerant charge for a residential Round-Tube-Plate-Fin (RTPF) heat exchanger, operating in both evaporator and condenser mode. The validated differential mass evacuation sampling method results in 0.1% of relative uncertainty with respect to measured charge and 1.3% of charge measurement repeatability. Additionally, charge sensitivity to independent variables was analyzed; in evaporator mode, charge is most sensitive to refrigerant inlet quality followed by outlet superheat. In condenser mode, subcooling followed by refrigerant mass flow rate is strongly correlated with charge. Although this study has been developed for the purpose of measuring refrigerant charge, it is universally applicable to studies to measure mass changes in a sample.

A part of this chapter, Section 2.2 and 2.3, are published in the Science and Technology for the Built Environment in 2020 (Lee et al., 2020). The rest of the chapter will be submitted for publication in the International Journal of Refrigeration.

2.1 Introduction

A literature review on experimental validation of refrigerant and oil charge models was carried out and it shows the validation is done by comparing the measured charge masses with those predicted by the simulation. Charge measurement techniques can be divided into two classes. The first is the sampling measurement technique (SM), which isolates the charge of a sample (*e.g.* heat exchanger) within very short period of time followed by determination of the charge in the sample through differential weighing or similar technique. The second technique is the online measurement technique (OM), where the charge is directly measured in situ either indirectly by transient measurement and integration of inlet and outlet mass flows or directly by weighing the change of mass of a system or component(s).

Therefore, the importance of validation data has been widely emphasized. Ma et al. (2009) proposed an experimentally validated void fraction model by using the quasi online measurement technique (Ding et al., 2009). This model combined existing void fraction correlations based on the flow pattern for the heat exchanger of the R410A air conditioner/heat pump with 7.1 kW cooling capacity. They recommended the best combination of void fraction correlations for their evaporator in cooling-mode, which is Taitel and Barnea (1990*a*) for intermittent flow and Premoli et al. (1971) for annular flow, respectively. The combined model resulted in 2.5% mean deviation from the measured mass.

Jin and Hrnjak (2016) reported experimentally validated refrigerant and oil charge model for microchannel condenser and plate-and-fin evaporator of an 4 kW automotive air conditioning system. They employed Peuker (2010)'s sampling measurement technique to obtain experimental charge data, and the validated model predicted the refrigerant mass in both heat exchangers within 20%. The oil model predicted the oil mass within 15% for condenser and 20% for evaporator respectively.

Since the two-phase flow inside heat exchangers is strongly affected by mass flux,

configuration, and flow regime, it is crucial to use experimentally validated void fraction correlations in environments where simulations will be used in practice. In this respect, very few studies investigated the validation of charge models for unitary split systems. This led to the development of ASHRAE TRP-1785, which has the objective of collecting high-fidelity experimental data for R410A split systems to validate these charge models. Specifically this validation experiments aim to round-tube-plate-fin heat exchangers for 3 ton (10.5 kW) capacity split systems.

Björk (2005) introduced the SM based on the p–v–T relationship for a superheated refrigerant vapor. The refrigerant is entrapped by quick-closing valves and then expanded into an evacuated tank into superheated state. The volume of the tank is known, so the mass is calculated by the p–v–T relationship of the refrigerant. His method is quite simple and fast for small (35 g of charge) refrigerant charge systems, but it is not deemed suitable for larger charge systems since it requires a substantially larger tank to accommodate large volumes of superheated refrigerant vapor.

Peuker (2010) proposed the SM utilizing an evacuated sampling cylinder, a flushing technique, and a mix-and-sample method. The oil and refrigerant charge in the system are recovered by employing an evacuated sampling cylinder placed in liquid nitrogen as a recovery pump. The refrigerant and oil charge are determined respectively by removing the refrigerant and weighing the cylinder. The flushing technique and the mix-and-sample method are employed for determining oil charge. His flushing technique utilizes a solvent to flush and remove oil from the test section. This technique has an accuracy of 1.4 g (1.4% of the 100 g of oil charge) with multiple consecutive flushes. The mix-and-sample method is to fill refrigerant and circulate it inside the section in which oil remains to remove the oil from the section. The mass of oil is calculated by measuring the well-mixed oil concentration. The accuracy of this method is 0.1 g (0.6% of the 22 g oil of charge). Even though this method requires at least 12 hours of testing time per data point, overall it has an excellent accuracy,

0.3% (4.2 g) of the 1245 g charge.

An early example for an online measurement (OM) method, Miller (1985) experimentally investigated charge migration of an outdoor unit of a heat pump by using a dedicated differential mass measurement scale. This OM method used a tare weight to compensate for the weight of the unit leaving only the refrigerant charge as the residual force. Charge migration was then measured by a load cell while the unit was operated in heating mode. Miller (1985) achieved ±50 g (0.1 lb) of accuracy in the charge mass measurement for a 3-ton (10.5 kW) outdoor unit. This method allows measurement in (almost) unmodified equipment but has over an order of magnitude less accuracy compared to Peuker (2010)'s method.

Saad Yatim et al. (2017) proposed a transient/integration OM technique. That OM technique utilizes the difference between the integrated mass of oil injection and total extracted oil mass from the setup. This approach does not require sampling related procedures such as disassembling test section and recovery of refrigerant, and thus makes it much cost and time effective. However, it is difficult to validate the accuracy of their method and no comparison to other techniques was found in open literature.

Ding et al. (2009) suggested a quasi OM technique. A refrigerant charge is moved to a connected sampling cylinder, and the cylinder is weighed to determine charge. In contrast to Peuker (2010), the measured refrigerant is re-used by the refrigeration system. This process decreases measurement time and saves refrigerant. While the quasi OM has a good accuracy (0.64%), refrigerant and oil charge cannot be measured separately by this method. In addition to that, Ding et al. (2009) compared both OM and SM techniques: the SM needs more time (300 min) than the OM, and has higher accuracy with order of 0.11% of measured charge by the SM; on the other hand, the OM is instantaneous and convenient method but has low accuracy with order of 10% of measured charge.

In summary, the SM techniques are accurate but slow while the OM techniques are fast but have limited accuracy. A better compromise between accuracy and speed of the measurement technique is needed to determine refrigerant and oil charge cost-effectively. This study presents a novel measurement method, called differential mass evacuation sampling method, to obtain separate refrigerant and oil charge in heat exchangers with an accuracy similar to the SM techniques that can be collected fast enough to accommodate the development of a large experimental validation database for charge simulation of 3 ton (10.5 kW) capacity split systems.

The differential mass evacuation sampling method and its prime testing apparatuses are published in Lee et al. (2020) and later the method is validated and evaluated in terms of accuracy and precision in Lee et al. (2022).

2.2 Overall Measurement Process

This section presents the developed method that determines the charge in a sample heat exchanger by measuring the difference to the dry heat exchanger weight with a specially designed Differential Mass Measurement Scale (DMMS). The method can provide the benefits of both, the OM and SM techniques by isolating and quickly separating the heat exchanger in steady-state operation to be measured using the DMMS. Additionally, this method measures refrigerant and oil charge in the heat exchanger quasi using a multi-step evacuation process to determine both, the oil and refrigerant masses. Furthermore, it does not require usage of liquid nitrogen and does not include multiple and complicated mixing steps which could decrease actual accuracy, reduce repeatability, and result in long measurement times.

The first step is to measure the internal volume of the heat exchanger under test. Then as shown in Figure 3.1, (1) the heat exchanger under test is mounted in a Removable Heat Exchanger Test Module (RHXCT) and the tare weight is collected by the DMMS. The RHXCT is subsequently, (2), mounted in a test section and operated

to the steady-state operating condition given in the test plan. Once acquisition of steady state performance data is complete, (3) two Rapid Shut-off Valves (RSVs) at the inlet and outlet of the RHXCT are closed simultaneously to trap the charge. Then, (4) the charge of refrigerant and oil is determined by measuring differential mass of the RHXCT in a multi-step process as described in the next section.

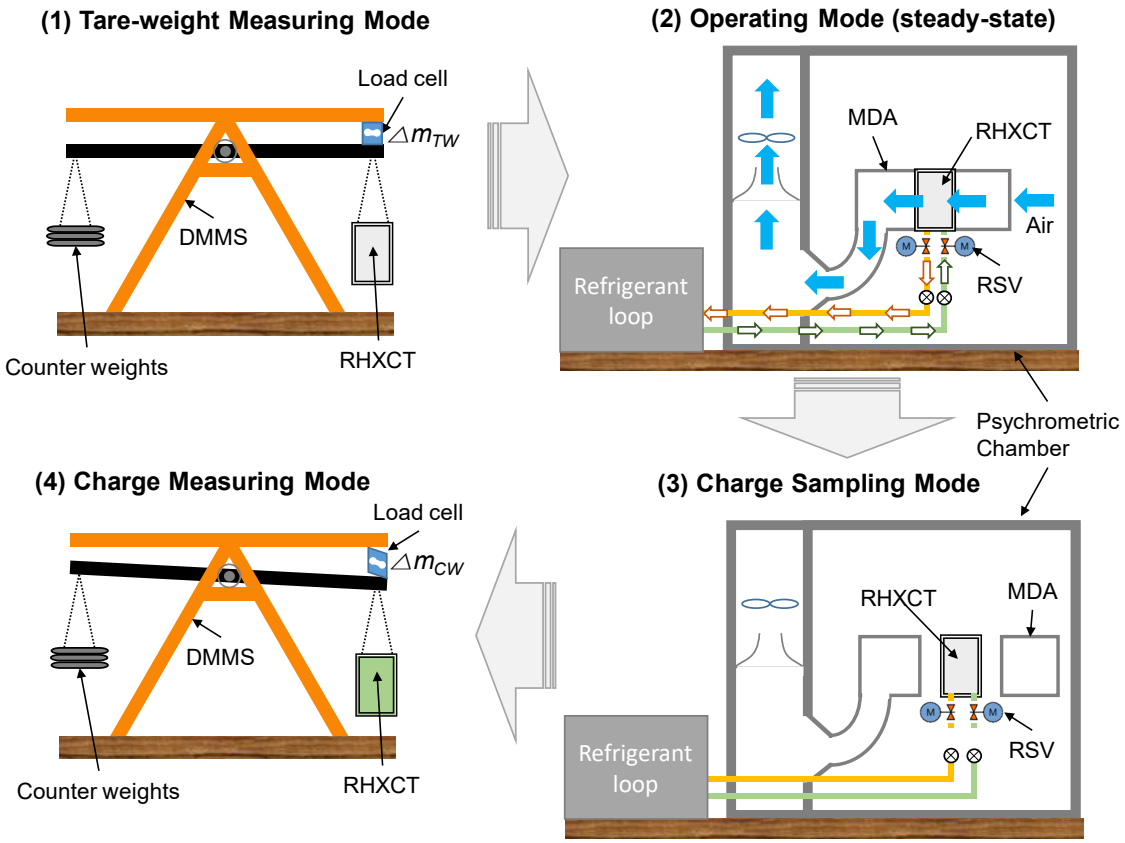

Figure 2.1: Schematic diagram of the charge measurement process for pure refrigerant (modified from Lee et al. (2020))

2.2.1 Test Procedure for Pure Refrigerant Charge

Simplified operation steps of the differential mass evacuation sampling technique for pure refrigerant (oil-free) are described:

1. Prior to weighing the RHXCT, the RHXCT is evacuated and weighed by the DMMS. This process gives the initial differential mass of the RHXCT, Δm_{dry},

which is the tare weight: the difference between a counterweight and mass of the RHXCT.

2. A developed modular duct assembly (MDA) is prepared in a psychrometric chamber. The MDA can deliver desired flow rate, temperature, and humidity of air inside a psychrometric chamber. The RHXCT is connected to the MDA and operated at a designed condition to allow refrigerant and oil flow rates to stabilize. Once a desired test condition is reached and steady-state data acquisition is complete, the refrigerant charge in the heat exchanger is sampled by simultaneously closing the RSVs on the RHXCT's inlet and outlet.

3. The RHXCT is disconnected from the MDA. Subsequently, the separated RHXCT is weighed again using the DMMS, after any condensate on the surface has evaporated. The measured differential mass is Δm_{start}. By subtracting Δm_{dry} from Δm_{start}, the total mass of refrigerant, m_{ref} enclosed between the two RSVs can be obtained. This can be expressed as

$$m_{ref} = \Delta m_{start} - \Delta m_{dry} \tag{2.1}$$

2.2.2 Test Procedure for Refrigerant and Oil Charge

Detailed operation steps of the differential mass evacuation sampling technique for refrigerant and oil charge are as follows:

1. Prior to weighing the RHXCT, oil in the separator is drained and the RHXCT is flushed with two phase pure refrigerant to remove any residual oil from previous experiments. Then, in order to measure the exact amount of refrigerant charge and oil retention in a heat exchanger, the RHXCT is evacuated and weighed by the DMMS. This process eliminates the effect of remaining oil residue on the

tare differential weight of the RHXCT, and gives the initial differential mass of the RHXCT, Δm_{dry}.

2. The RHXCT is connected to the MDA and operated at a designed condition to allow refrigerant and oil flow rates to stabilize. Once a desired test condition is reached and steady-state data acquisition is complete, the refrigerant charge and oil retention in the heat exchanger is sampled by simultaneously closing the RSVs on the RHXCT's inlet and outlet.

3. The RHXCT is disconnected from the test section by disconnecting the refrigerant and electrical connections and unclamping the RHXCT from the MDA.

4. The separated RHXCT from the test section is weighed again using the DMMS, after any condensate on the surface has evaporated. The measured differential mass is Δm_{start}. By subtracting Δm_{dry} from Δm_{start}, the total mass of refrigerant and oil, $\Delta m_{ref\&oil,tot,start}$, enclosed between the two RSVs can be obtained. This can be expressed as

$$m_{ref\&oil,tot,start} = \Delta m_{start} - \Delta m_{dry} \tag{2.2}$$

5. The refrigerant is recovered by connecting a recovery machine, leaving only the oil mass in the RHXCT. The refrigerant-oil mixture passes through a coalescent oil separator inside the RHXCT to ensure that only pure refrigerant is recovered. Thereafter, the RHXCT is evacuated by using a vacuum pump. Minimum pressure at the end of the evacuation process is set higher than the vapor pressure of the oil; the exact value will be determined based on the oil which will be used in the test. This will ensure that all oil remains in the RHXCT. During the evacuation process, water condensate might be generated on the surface of the RHXCT; therefore fans are utilized to blow air toward the RHXCT to reduce

condensate generation and evaporate any condensate prior to the next step.

6. After completing the refrigerant recovery, the DMMS is utilized to measure Δm_{end}. By subtracting Δm_{dry} from Δm_{end}, the mass of oil, the refrigerant that is dissolved in the oil, and the residual refrigerant in the vapor state are determined as

$$m_{ref\&oil,tot,end} = \Delta m_{end} - \Delta m_{dry} \tag{2.3}$$

7. $m_{ref\&oil,tot,end}$ contains the actual oil mass, the mass of refrigerant dissolved in the oil, $m_{ref,solub}$, and the mass of refrigerant within the test section $m_{ref,sh}(V_{tot}, T, P)$ at the given total volume of all components of the test section as well as given pressure and temperature. Thus the actual oil mass can be expressed as

$$m_{oil} = m_{ref\&oil,tot,end} - m_{ref,solub} - m_{ref,sh}(V_{tot}, T, P) \tag{2.4}$$

In this study, we anticipate that $m_{ref,solub}$, $m_{ref,sh}(V_{tot}, T, P)$ are neglected due to the negligible solubility of refrigerant in oil at low evacuation pressure and negligible mass of superheated refrigerant. Therefore, actual oil mass can be simplified as follows:

$$m_{oil} \approx m_{ref\&oil,tot,end} \tag{2.5}$$

8. Refrigerant mass is determined by subtracting the oil mass, m_{oil} from the total initial mass of refrigerant and oil, $m_{ref\&oil,tot,start}$:

$$m_{ref} = m_{ref\&oil,tot,start} - m_{oil} \tag{2.6}$$

2.3 Supporting Test Apparatus

The experimental apparatus used for this test method is classified into three types. The first are devices for providing test conditions such as a fluid conditioning loop and an air-side apparatus. The second are devices for obtaining charge samples, the RHXCT, and the third is a DMMS for determining the charge in the heat exchanger. The following subsections provide descriptions of the design and operation of the RHXCT and air and refrigerant conditioning apparatus.

2.3.1 Removable Heat Exchanger Charge Test Module (RHXCT)

The RHXCT is a paramount piece of infrastructure that requires precise instrumentation of the refrigerant and air-side of the heat exchanger to determine the thermodynamic performance at a given operating condition with enough control to ensure a useful test. Additionally, to supplement the charge information, accurate internal volume of the RHXCT is required to ensure the mass data is of maximum utility from the experiments. The following section outlines how the design of the RHXCT supports these objectives and how accurate volume measurements are obtained.

To focus on investigating the charge, simplified Round Tube Plate Fin Heat Exchangers (RTPF) have been designed with face-split four circuits having uniform circuit length, which minimize internal heat transfer: Indoor Coil 1 (IC1) and Outdoor Coil 1 (OC1) as shown in Table 2.1 and Figure 2.2.

The inlet and outlet of the RHXCT each have one refrigerant distributor. A schematic diagram and picture of the RHXCT for IC1 and OC1 are displayed in Figure 2.3, Figure 2.4, and Figure 2.5.

They show the overall concept of the RHXCT: first to be equipped with necessary measurement devices such as the upstream temperature and pressure sensor for determining the liquid temperature, the downstream temperature and pressure sensor for determining the outlet superheat, and the pressure sensor after the electronic

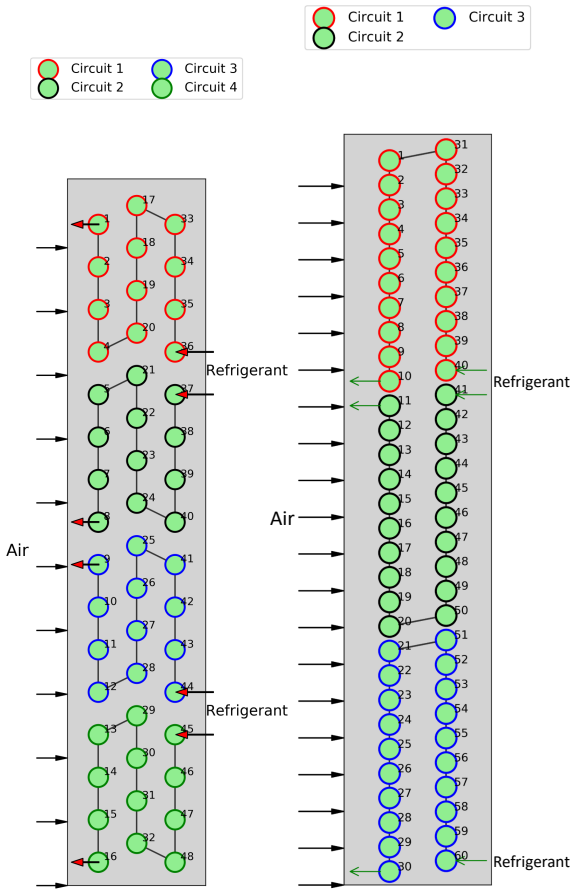

Figure 2.2: Schematic circuit diagram of the RTPFs: (left) IC1, (right) OC1

expansion valves for determining the evaporation pressure of the refrigerant; and second to be removable using a combination of rapid shut-off valves, Rotolock valves, and electrical disconnects; and third to be controlling refrigerant flow rate of individual circuits of the heat exchanger to ensure equal exit superheats for evaporator tests by using individual circuits' electronic expansion valves and differential pressure transducers.

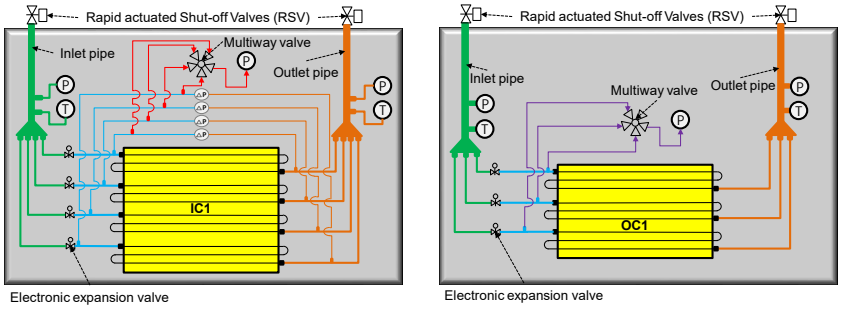

Figure 2.3: Schematic diagram of the RHXCT that is the unit to be weighed: (left) the RHXCT for IC1, (right) the RHXCT for OC1

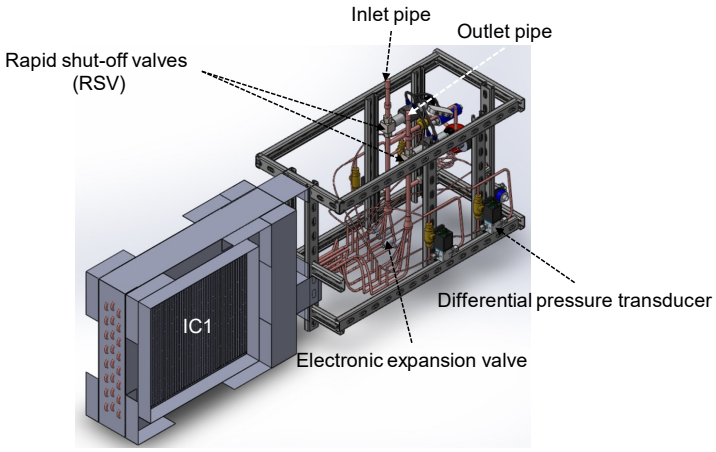

Figure 2.4: 3D model of the RHXCT for IC1

The most significant components in the RHXCT are the RSVs at the inlet and outlet pipes. The synchronized RSVs allow to sample charge accurately. The RSVs use a plug valve (Swagelok P6T) due to its low friction, low mass inertia, high working pressure, and easy maintenance.

Table 2.1: Geometrical parameters of the RTPFs: Indoor Coil1 (IC1) and Outdoor Coil1 (OC1)

	IC1	OC1
Number of tubes per bank	16	30
Number of bank	3	2
Number of circuits	4	3
Length of tubes	0.445 m	1.219 m
Outer diameter of tube	0.0095 m	0.0095 m
Inner diameter of tube	0.0089 m	0.0085 m
Tube spacing in air flow direction	0.0219 m	0.0191 m
Tube spacing orthogonal to air flow direction	0.0254 m	0.0254 m
Number of fins per inch	14	20
Amplitude of wavy fin	0.001 m	0.001 m
Half period of wavy fin	0.001 m	0.001 m
Fin thickness	0.0001 m	0.0001 m
Fin type	Sine wave fins	Sine wave fins
Internal tube type	Smooth	Smooth

To control refrigerant flow rate of individual circuit, electronic expansion valves (Danfoss ETS6-10 for IC1 and ETS6-14 for OC1) are installed at the entrance to each circuit. The expansion valve openings are adjusted to obtain an equal circuit-exit superheat, by checking temperature of surface mounted thermocouples and differential pressure on each individual circuit. In oil measurement mode, a coalescent oil separator (Temprite Model320) is installed inside the RHXCT to separate oil from the oil and refrigerant mixture for measuring charge respectively.

2.3.1.1 Instrumentation and Uncertainty of the RHXCT

To minimize oil entrapment and retention inside the RHXCT, the module is designed to minimize the number of inlet and outlet pipe's bends. In this regard, the oil injection point to the RHXCT is at top of the module, and the inlet and outlet pipes of the RHXCT are vertical and straight. In addition, 90° bent resistance temperature detectors (RTDs) have been custom made and inserted in the both vertical inlet and outlet pipes without sacrificing RTD's flow contact area and direction; furthermore this vertical design of pipes promotes uniform refrigerant distribution by reducing

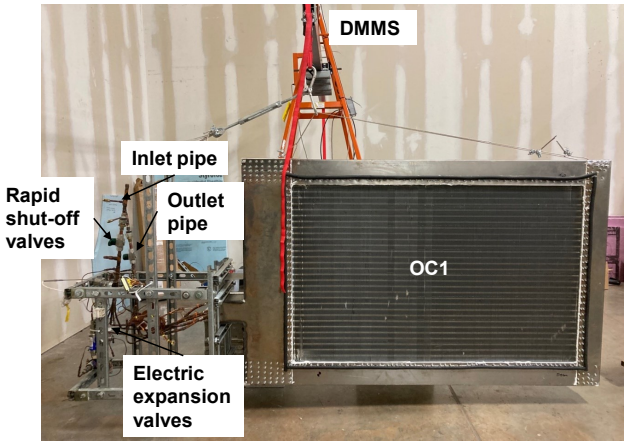

Figure 2.5: RHXCT for OC1 with the DMMS

interference to flow through the refrigerant distributor. The RTDs have been calibrated in house, and have an accuracy within 0.04 °F (0.02 °C) of the reference thermometer's reading. Thermocouples have been calibrated in house, and have an accuracy within 0.4 °F (0.22 °C) of reference thermometer's reading. The accuracy of the calibration reference thermometer (Thermoprobe, TL1A) is 0.1 °F (0.06 °C).

The RHXCTs require all connections to be disconnected for each charge measurement. Therefore, all sensors, controllers, and pipes have quick-disconnects. Thermocouples are grouped on Omega SMTC series D-SUB style disconnects, which each accommodate 25 thermocouples. The differential pressure transducers were installed on each individual circuit to check pressure drop across the circuit. They have been calibrated in house and have an accuracy within 0.055 psig (0.38 kPa) of the reference pressure sensor's reading. The accuracy of the calibration reference pressure sensor (GE, Druck DPI 612) is 0.0075 psig (0.05 kPa).

Two pressure sensors have been installed to before and after the refrigerant distributor in the inlet pipe, having a rated accuracy of 0.25 psig (1.72 kPa) with NIST traceable calibration. The outlet pipe has an in-house calibrated pressure sensor, with accuracy within 0.3 psig (2.07 kPa) of the reference pressure sensor's reading. The accuracy of the reference pressure sensor utilized in the calibration is 0.375 psig

(2.59 kPa).

2.3.1.2 Volume Measurement of the RHXCT

Charge-prediction models utilizing void fraction are significantly affected by volume; according to Jin and Hrnjak (2016), volume data containing charge is needed to calculate charge inventory of refrigerant and oil. Hence, highly accurate volume data is needed in order to achieve high fidelity charge prediction. A Volume-Measurement Device (VMD) has been developed for accurate volume measurement, and its principle is shown in Figure 2.6. The operation steps of the VMD are as follows:

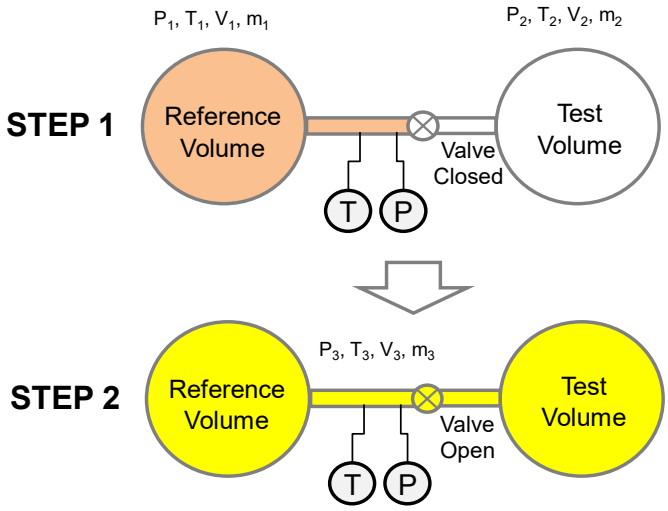

Figure 2.6: Principle and operating process of the Volume-Measurement Device (VMD)

1. Two volume tanks are connected via a ball valve: one tank is a test-volume-tank whose volume to be measured, and another is a reference-volume-tank utilized to calculate volume of the test-volume-tank. A thermometer (ThermoProbe Inc., TL1-A) having an accuracy of ±0.1 °F (±0.06 °C) and pressure sensor (GE, Druck DPI 612) having an accuracy of ±0.0075 psig (0.05 kPa) are installed at the connection between the two tanks as illustrated in Figure 2.6.

2. The two tanks are placed at equilibrium by opening the valve; then temperature and pressure are measured. The pressure and the temperature are P_2, T_2 respectively. After that the valve is closed, and the isolated volume and the mass in the test volume are V_2, m_2 respectively.

3. Inert gas (*e.g.* Nitrogen) is injected into the reference volume, which increases the pressure. Once equilibrium is reached, the pressure (P_1) and the temperature (T_1) are measured. The isolated volume and the mass in the reference-volume are V_1, m_1 respectively.

4. The valve is opened to re-join the reference and test volumes. After equilibrium is reached, the pressure (P_3) and the temperature (T_3) of the combined volume are measured. The total volume and mass in the combined volume are V_3, m_3 respectively.

5. The test volume to be known is calculated by using ideal-gas equations described in the next paragraphs.

By employing the ideal gas equation of state to each state and volume we obtain: $P_1 V_1 = m_1 R T_1$, $P_2 V_2 = m_2 R T_2$, $P_3 V_3 = m_3 R T_3$, *and* $P_3 V_3 = (m_1 + m_2) R T_3$. By substituting m_1, m_2, and rearranging, the previous equation becomes:

$$P_3 (V_1 + V_2) = \frac{P_1 V_1 T_3}{T_1} + \frac{P_2 V_2 T_3}{T_2} \tag{2.7}$$

To obtain V_2 (volume to be known), rearranging Equation 2.7 then:

$$Test\ volume = V_2 = \frac{\left[\left(\frac{P_1 T_3}{T_1} - P_3\right) \cdot V_1\right]}{P_3 - \frac{P_2 T_3}{T_2}} \tag{2.8}$$

As described in Equation 2.8, V_2 (volume to be known) can be calculated if the volume of the reference tank, all the temperatures, and the pressures are known.

The target charge uncertainty for this test method is 1 g, which requires a heat exchanger volume measurement accuracy smaller than the volume corresponding to this charge value. For this reason, the target uncertainty of volume measurement was reversely calculated from the accuracy of the charge to determine the maximum uncertainty of volume measurement allowed to ensure the total charge uncertain would not exceed the target of 1 g.

The approximate volume of the RHXCT for IC1 was calculated by measuring internal dimensions of the RHXCT, which is 2181.1 ml. Using R410A as the working fluid, it was assumed that it has constant quality (0.5) and evaporating temperature (50 °F (10 °C)), thus resulting in 176.3 g estimated charge. Then the target accuracy of charge, 1 g, was added to the estimated charge, leading to an updated charge estimation, 177.3 g. As a result, the updated charge estimation yields a revised volume, 2193.0 ml. Therefore, the volume difference between the original estimated volume and the revised volume becomes the target accuracy of the VMD at evaporating mode which is 12.4 ml, accounting for 1 g of the charge accuracy.

In the same manner, the target accuracy of volume for condenser test was obtained. Using R410A as the working fluid again, it is assumed that it has a constant quality (0.5) across the heat exchanger and constant condensing temperature (110 °F (43.3 °C)), thus resulting in 445.2 g estimated charge. Then the target accuracy of charge, 1 g, is added to the value: 446.2 g. Therefore the charge yields a revised volume, 2186.0 ml. The volume difference between the original volume and the revised volume becomes the target accuracy of the VMD, 4.9 ml, accounting for 1 g of the charge accuracy. As a result, the final target accuracy of the VMD becomes 4.9 ml, and the target percentage error of the accuracy for the volume measurement becomes 0.2 %: *e.g.* 4.9 ml is divided by 2181.1 ml and multiplied by 100%.

The VMD's accuracy was validated using comparison to a water-filling-method. First, all the volumes inside the RHXCT, as shown in Figure 2.7, were determined

by filling water carefully and measuring the water with graduated cylinders. As a result of the water-filling-method, the test volume measured 1079.4 ml as a mean value with ±0.8 ml total uncertainty as shown in Figure 2.8 (left). Second, the test volume was calculated by the VMD as described in the aforementioned procedure. The result of the validation is described in Figure 2.8 (right): the test volume by the VMD measured 1079.2 ml as a mean value with ±2.5 ml uncertainty. The mean value's difference between the water-filling-method and the VMD yields 0.2 ml, and the percentage error is 0.02%. Accordingly, it was verified that the accuracy of the VMD is within the target accuracy (4.9 ml) as illustrated in Figure 2.8 (right). Low pressure, under 30 psig, was used in the VMD to minimize the effect of temperature change on the measurement outcome. It was observed that maximum temperature change was 0.6°F in the five attempts of the VMD. The high accuracy (±0.0075 psig (±0.052 kPa)) of the pressure sensor additionally contributes to the VMD's volume measurement accuracy.

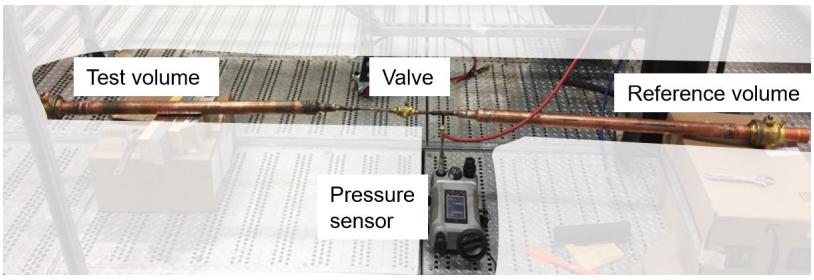

Figure 2.7: Test setup used for validation of the VMD. The thermometer is not shown in this figure

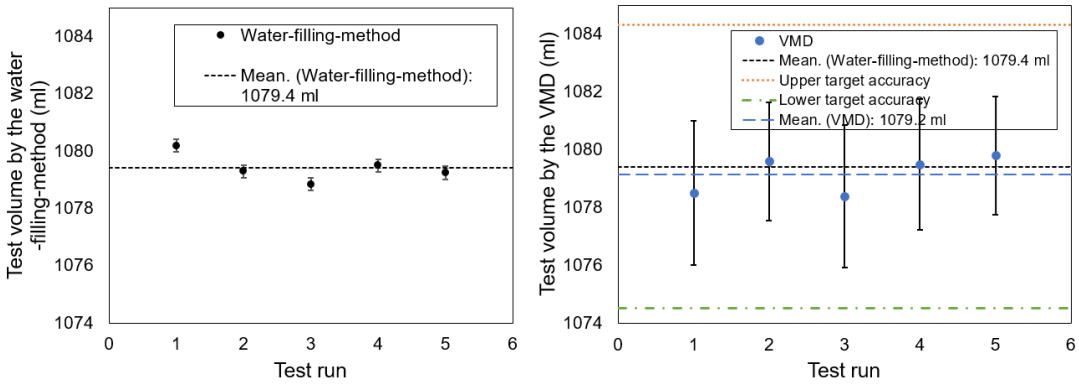

Figure 2.8: Validation result of the VMD: the test volume by the water-filling method as a baseline (left), the test volume by the VMD (right) shown with the target accuracy of the volume.

Using the developed VMD, the internal volume of the RHXCT's subcomponents was determined as shown in Figure A.1-A.4 in Appendix.

The uncertainty propagated from measurement as specified in ASME-PTC-19.1 (2013) was calculated using Engineering Equation Solver (EES; (Klein and Alvarado, 1992)) for the VMD in IC1: ±5.4 ml uncertainty, which is equivalent to ±2 g of mass-accuracy, reversely calculated in the same way as the target accuracy of the VMD was analyzed in the condenser test mode. This measured volume of the RHXCT can be used to predict charge by charge simulation programs.

2.3.2 Refrigerant and Oil-Side Experimental Apparatus

The RHXCT was connected to a refrigerant-side conditioning apparatus developed by Saleem et al. (2020). The refrigerant-side apparatus capacity is 5 tons (17.52 kW); a variable speed refrigerant gear pump allows to change the refrigerant mass flow rate, a tank-less water heater was installed inside the hot water loop to control inlet conditions of test section, and a Coriolis-type mass flow meter was connected to the liquid line to measure the refrigerant flow rate. Two heat pumps act as coolers or heaters depending on the test requirements. Additional detail of the refrigerant conditioning system for pure refrigerant tests (oil free) can be found in Saleem et al.

(2020).

An integrated data acquisition software, shown in Figure 2.9, was developed in LabVIEW for the accurate control of the experimental setup. This software covers collection and display of raw and processed data, controlling the testing apparatuses, reducing and analyzing data, and saving data.

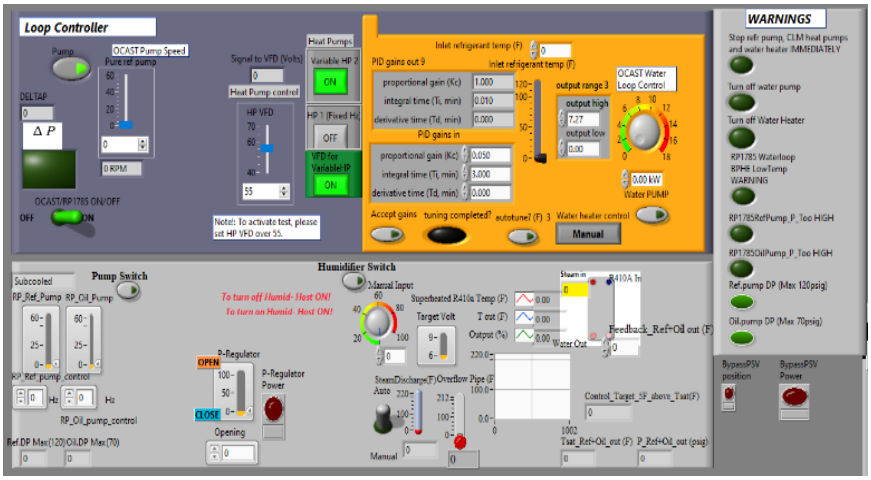

(a) testing apparatuses control

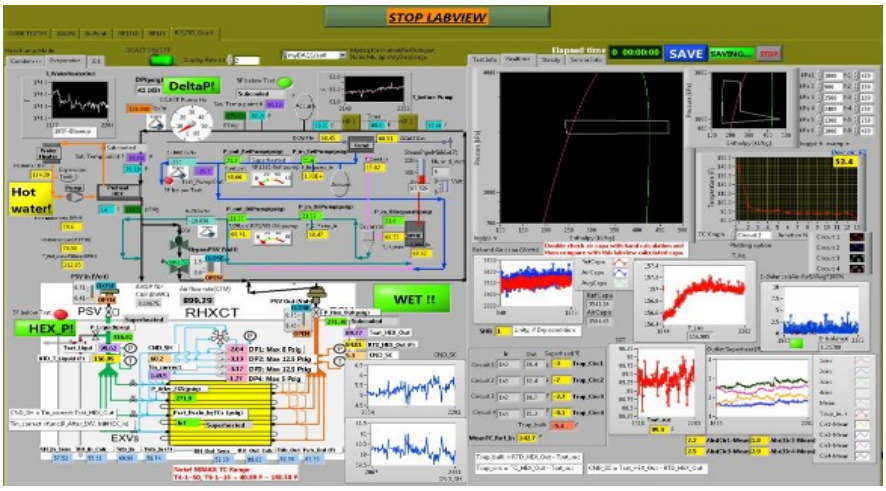

(b) data monitoring/saving

Figure 2.9: Screen captures of the integrated data software based on LabVIEW

For oil and refrigerant mixture tests, Figure 2.10 illustrates a pumped oil conditioning loop and a superheating and oil separation system, which enable controlling

oil and refrigerant flowrate independently to obtain oil circulation ratios between 0-5% by mass.

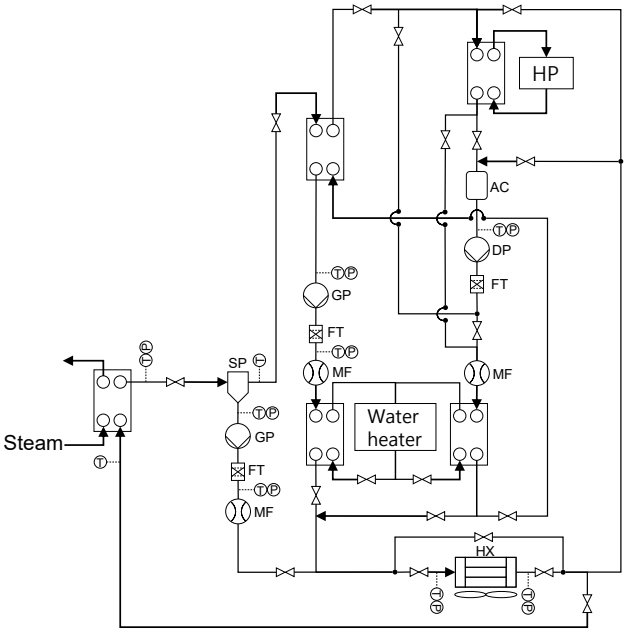

MF	Mass flow meter
GP	Gear pump
DP	Diaphragm pump
HX	Heat exchanger (test section)
FT	Filter-drier
AC	Accumulator
SP	Oil separator
HP	Heat pump

Figure 2.10: Schematic diagram of the overall fluid (refrigerant and oil mixture) side's experimental setup, modified from Saleem et al. (2020)

2.3.3 Air-Side Experimental Apparatus

The RHXCT is assembled with the MDA inside a psychrometric chamber as shown in Figure 2.11. A simplified diagram of the air circulation of the psychrometric chamber used for this study is detailed in Figure 2.11. Air enters the MDA that includes the RTPF under test through the inlet duct (Figure 2.11, left). The flow then passes by the heat exchanger under test and the flow measurement bay (Figure 2.11, right).

The flow measurement bay is located in between the two conditioning bays. The air that goes through the flow measurement bay is then divided to flow through two conditioning bays. The conditioned air is then returned to the room through the chamber's perforated floor. Some of the air re-enters the modular duct assembly, the remainder rises to the ceiling and is brought back to the conditioning bays through the ceiling plenum.

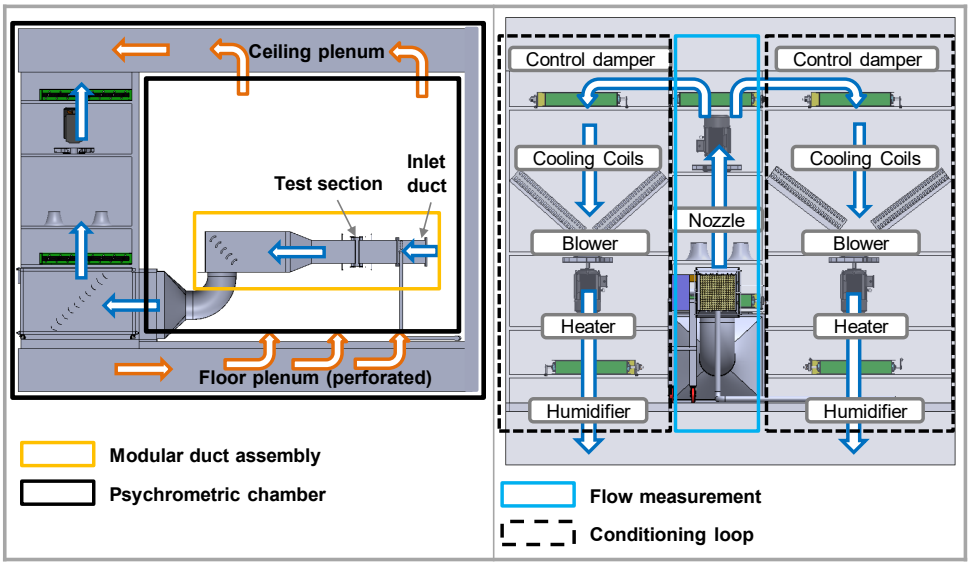

Figure 2.11: Air circulation within the psychrometric chamber used for this study; cross-section of psychrometric room along duct flow direction. Note that the chamber has a perforated floor and ceiling (left) and perpendicular to duct flow direction (right)

The air that goes through the ceiling is merged with the air that goes through the flow measurement bay, and the air circulation process mentioned above is repeated during the psychrometric chamber operation. Full details of these chambers' operation can be found in Lifferth (2009) and Worthington (2011).

It is essential for the MDA to have a uniform airflow since it is the basis for accurate charge measurements. As part of a preliminary analysis presented in Lee et al. (2018), an analysis of how to obtain comparatively uniform airflow on a large outdoor heat exchanger was performed using CFD as shown in Figure 2.12. Heat exchanger inlet air

velocity distribution for the duct inside the psychrometric chamber was investigated. The first heat exchanger under test, IC1, is a single-slab of a representative indoor A-coil for a 3 ton (10.55 kW) heat pump with details provided in Table 2.1.

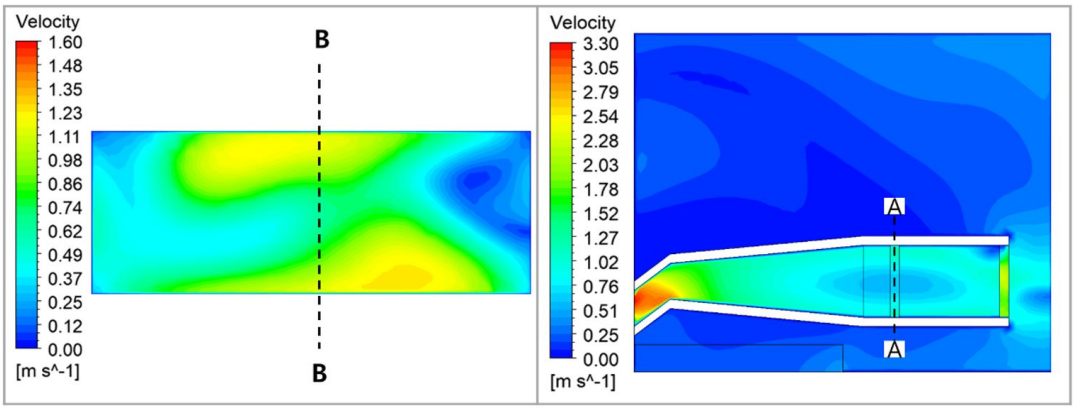

Figure 2.12: CFD case study by Lee et al. (2018): Velocity contour, (Left) Front view on the heat exchanger (A-A), (Right) Side view at the center of the heat exchanger (B-B). The dotted line represents the positions of the cross-sectional areas of each other. (1.60 m/s = 314.96 fpm, 3.30 m/s = 649.61 fpm)

Using the results from the aforementioned CFD analysis, the duct design for IC1 was developed as shown in Figure 2.13. The completed MDA is shown in Figure 2.13 and Figure 2.14. It is noted that the duct assembly is modular to allow for the easy change of heat exchanger adaption duct sections, and a flexible tube with 20 in (0.508 m) diameter was used to connect the duct to the code tester/nozzle box. As a result, the position of the duct can be freely changed. For example, the height of the duct and the distance between the inlet duct and the wall can be adjusted to acquire uniform air flow.

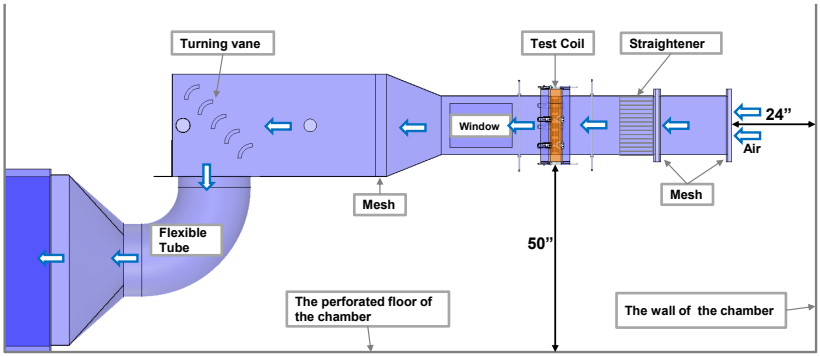

Figure 2.13: Schematic design for the MDA as informed by the CFD analysis (50 in = 1.270 m, 24 in = 0.610 m)

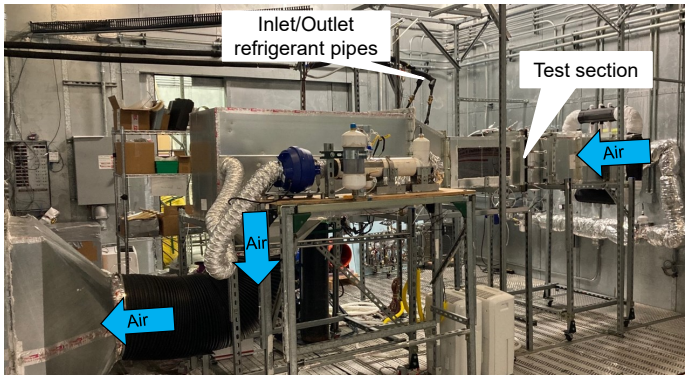

Figure 2.14: Picture of the completed MDA for the IC1. The duct insulations are not shown in this figure.

Since the MDA and the flexible tube are connected at right angles, turning vanes

are used to reduce air pressure losses. A psychrometer was installed next to the duct, and an air sampler tree was inserted inside the duct to sample downstream air. Three settling means were installed inside the duct with 58% open area, 0.25 in (0.006 m) hole size, staggered pattern, and 0.0291 in (0.739 mm) thickness: two were located upstream of the RHXCT and another was located downstream of the RHXCT. The pressure class of the duct is 2 in w.g. (497.68 Pa).

The test section was connected using the upstream duct and the downstream duct by flanges with clamps so that the duct assembly can be easily separated. Approximately 2,000 thin walled polymer tubes (8.3 in (0.211 m) long, 3/8 in (0.010 m) outside diameter, 0.37 in (0.009 m) inside diameter) inside the duct were used as airflow straightener. In order to prove uniform air flow, the MDA—shown in Figure 2.15—has been tested: the uniformity of the air velocity was within ASHRAE standard 33's 20% limit, and similarly the uniformity of the air temperature was within the standard's 0.56 K (1.0 R) limit, thus yielding the verification of air uniformity of the duct. A more detailed description of the uniformity tests previously is presented in Lee et al. (2019).

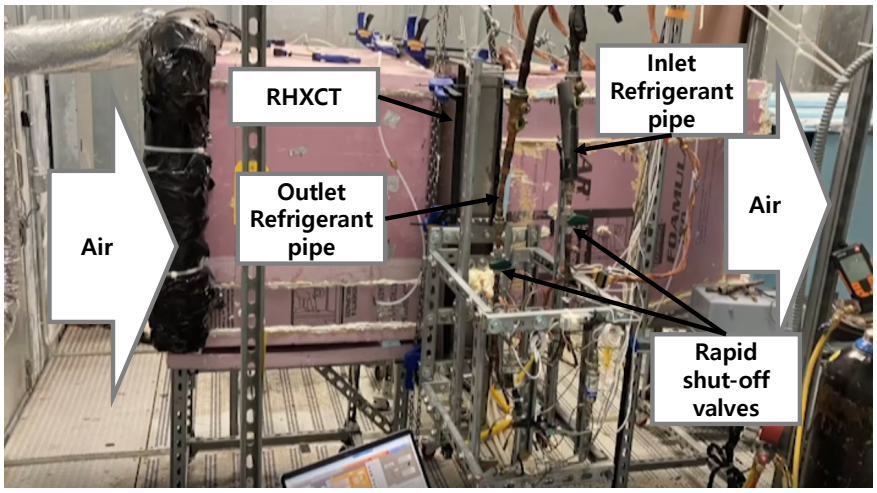

Figure 2.15: Picture of the completed MDA for the OC1

2.3.4 Differential Mass Measurement Scale (DMMS)

Drawing inspiration from Miller (1985)'s differential mass measurement scale, an improved DMMS is presented and shown in Figure 2.16.

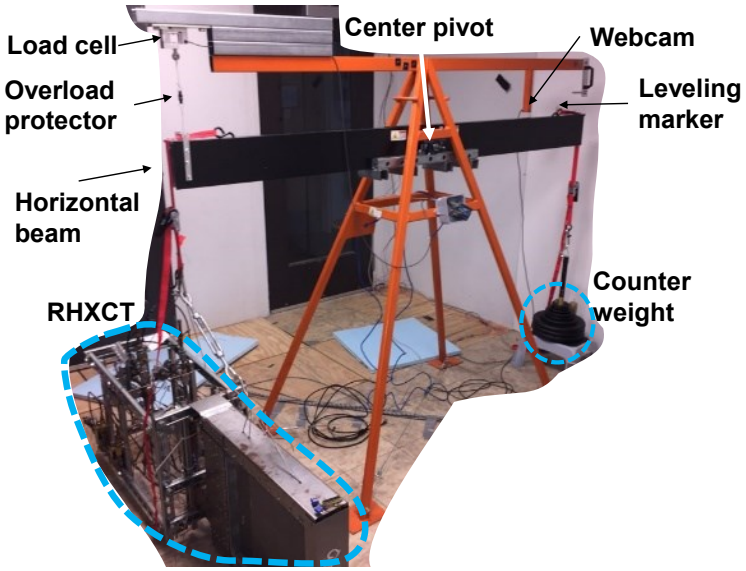

Figure 2.16: Picture of the DMMS with the RHXCT

First, the refrigerant hoses and electrical lines are removed from the updated DMMS during the charge measurement process to improve the accuracy. This separation removes any line and instrumentation weight biases from the measurement. Second, as the length of the horizontal beam is increased, the torque applied to the center pivot increases, which reduces the measurement error caused by the friction force of the center pivot. Accordingly, the DMMS utilizes a horizontal beam of a length maximized for the given apparatus space size. The apparatus space is designed to protect from uncontrolled airflow due to HVAC systems and/or personnel.

The center pivot is further improved by using four low-friction, self-aligning pillow block bearings that enable a rotating shaft, reducing hysteresis. Structurally, the four bearings connect the horizontal beam and the support frame which can hold up to 280 kg; and a 12.7 mm shaft connects the four concentric bearings as exhibited Figure 2.17. Third, Miller (1985) used a load cell with an accuracy of 50 g; this study employs a high accuracy load cell (HBM-S2M-10N) with a maximum capacity of 1,000 g, with a 0.02% full scale accuracy, translating to an accuracy of 0.2 g. Fourth, the load cell includes an internal mechanical overload protection mechanism to prevent loss of calibration. Additionally, a mechanical overload protector, two in-line permanent magnet disks holding up to 1 kg before separation, are used between the load cell and the horizontal beam to protect the load cell as displayed in Figure 2.17. Lastly, the output signals of the load cell are amplified and converted to digital signals using an HX711 amplifier and an analogue to digital converter and then are sent to a LabVIEW program which saves and displays data. The load cell and signal processing units are calibrated *in-situ*.

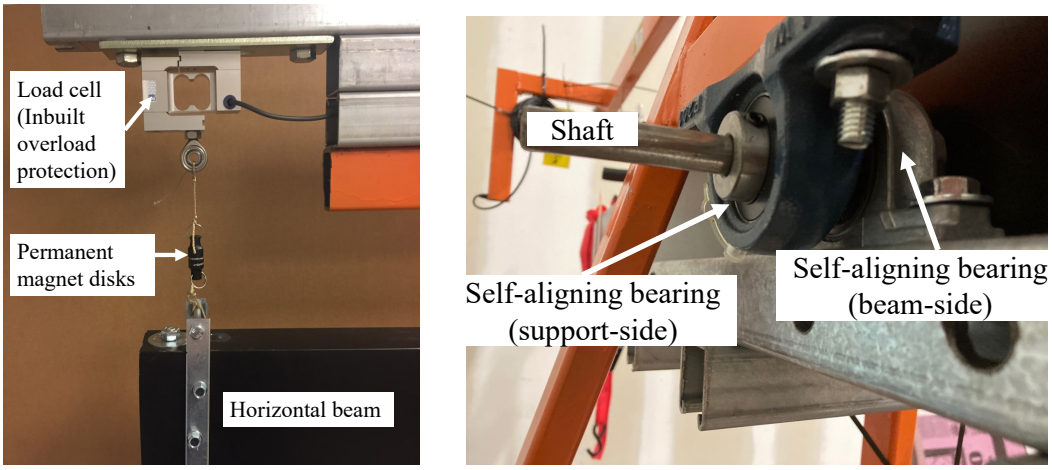

Figure 2.17: Mechanical overload protector (left) and center pivot (right) of the DMMS

The accuracy of the DMMS was validated by a series of measurements with a standard mass. Figure 2.18 describes the process to acquire the accuracy of the

DMMS as follows:

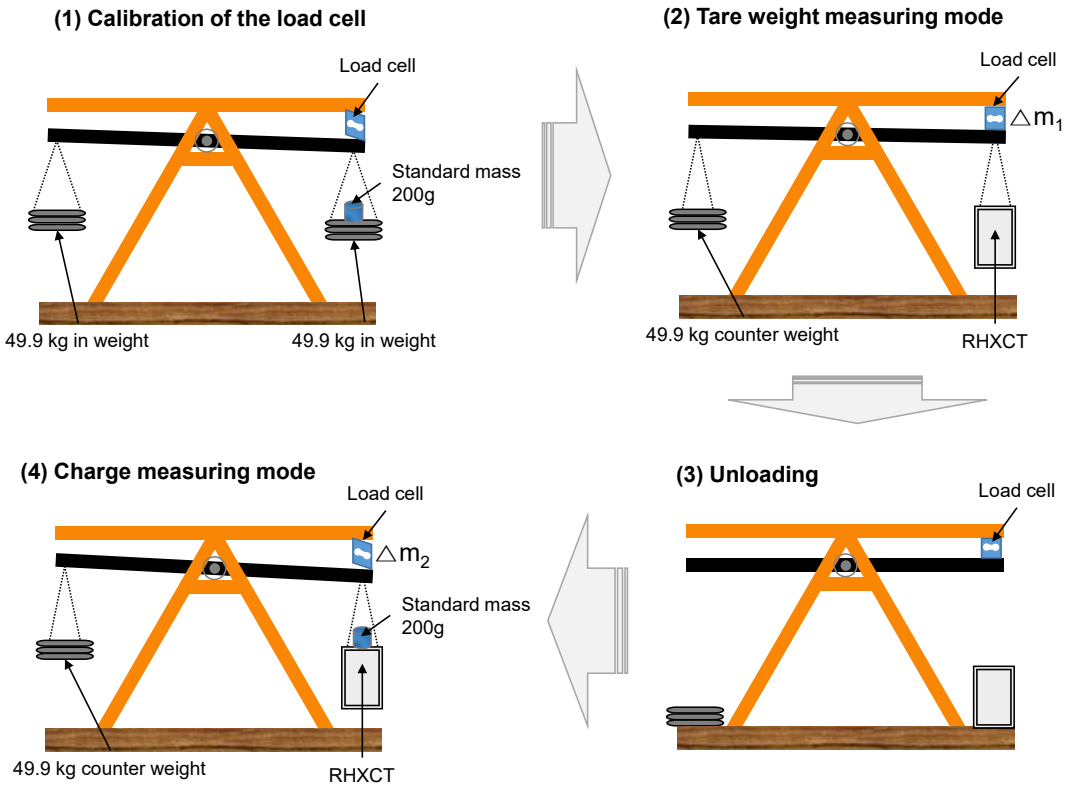

Figure 2.18: Schematic diagram of the measurement process to determine the accuracy of the DMMS. The movement of the horizontal beam is exaggerated for illustration purposes.

(1) Two weights were suspended from each side of the DMMS, and 200 g of the standard mass was added onto the weight on the load cell side. The calibration of the load cell was performed with the 200 g of the standard mass *in-situ*.

(2) With the RHXCT and a counterweight suspended from the DMMS, a tare weight (Δm_1) was measured by the load cell after the horizontal beam was leveled.

(3) Thereafter, to simulate the real charge measurement process, the RHXCT was unloaded from the DMMS and re-loaded to the DMMS

(4) Subsequently the standard mass (200 g) was added onto the RHXCT to simulate a charge weight. The charge weight including the tare weight (Δm_2) was measured

by the load cell after the beam was leveled. The final charge (*e.g.* change of mass) was then calculated by subtracting the measured Δm_1 from the measured Δm_2.

(5) The process from (2) to (4) was repeated 7 times, and the comparison between the standard mass (200g) and the measured change of mass is demonstrated in Figure 2.19.

Figure 2.19 describes the comparison result between the standard mass and the 7 measurements by the DMMS; the mean value of the DMMS's reading to the 200 g of standard mass was recorded as 200.6 ± 1.4 g with a 95% confidence interval of calculated using a student-t distribution. The maximum absolute error of the DMMS was 3.2 g (1.6% of the relative error with 200 g of the known standard mass), translating to a 0.006% of relative accuracy of 49.9 kg tare weight of the RHXCT. In addition, a threshold of less than 1 g of random error is used as criteria before saving data, indicating that periodic fluctuations of the measured data, caused by any residual movement, are sufficiently small. The random errors are obtained from a standard deviation of measurements; it is estimated as twice of the standard deviation of the readings at 95% confidence interval.

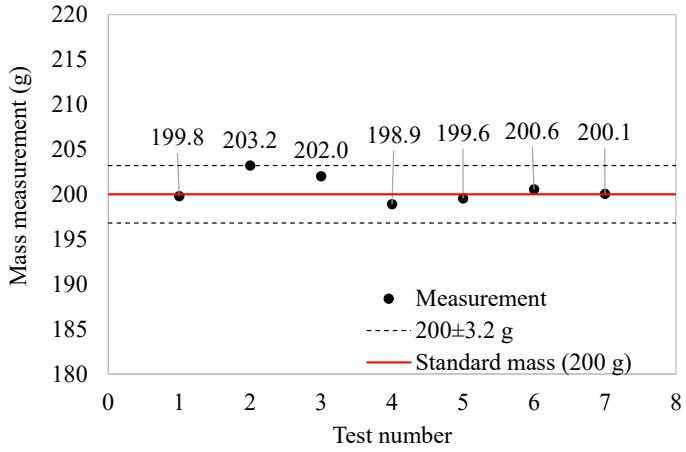

Figure 2.19: Measurements of the DMMS with the added known mass (200 g) after reloading the RHXCT

Along with accuracy, a precision of the DMMS was assessed by repeatability of

weighing the same tare weight of the RHXCT repeatedly. The weighing process by the DMMS was repeated four times, and the relative deviations for the first measured weight are plotted in Figure 2.20. The maximum absolute deviation among the four measurements was 1.6 g which is equivalent to 0.003% of repeatability relative to our 49.9 kg tare weight of the RHXCT for IC1. Consequently, the developed DMMS allows acquiring high-quality experimental charge validation data for a variety of testing conditions in an RTPF.

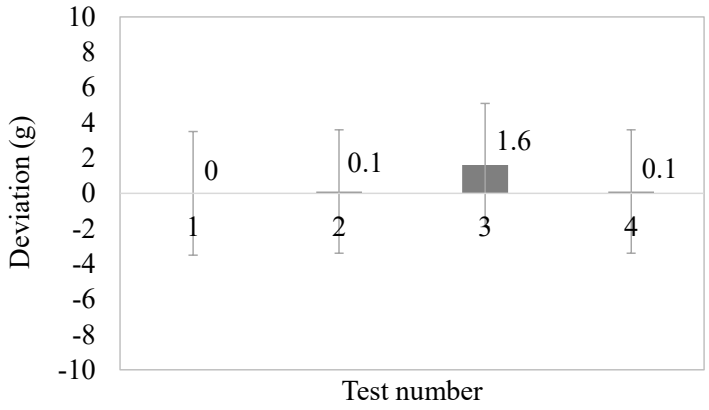

Figure 2.20: Deviations of the dry-weight measurement of the RHXCT by the DMMS: the first attempt (*i.e.* Test number 1) is the baseline for others in terms of the indicated deviations. The error bars indicate the uncertainties of the DMMS measurements.

2.4 Validation of Charge Measurement Method

A validation of the differential mass evacuation sampling method was carried out by measuring the same amount of refrigerant on a commercial refrigerant scale (TIF9020A) and the DMMS respectively and comparing each measurement with the other. The whole charge measurement processes and comparisons were repeated four times to ensure credibility of the validation. The validation results are given in Figure 2.21.

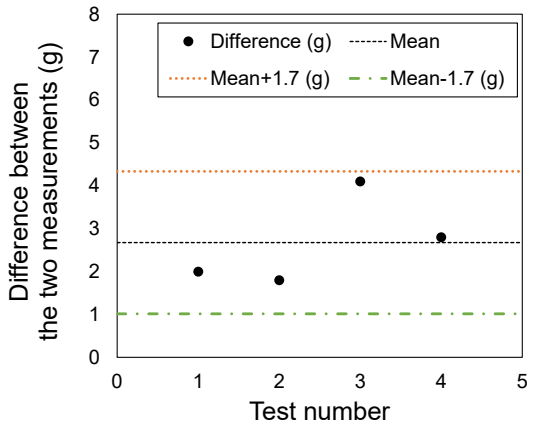

(a) Difference between the DMMS measurement and the refrigerant scale measurement

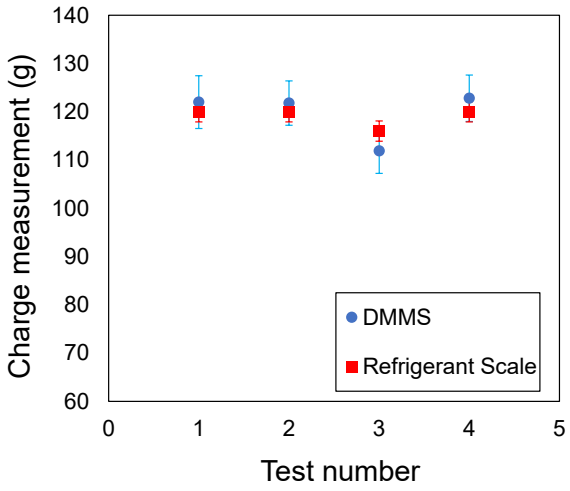

(b) Charge measurement by the DMMS and the refrigerant scale

Figure 2.21: Validation result of the charge-measurement method. The error bars indicate the measurement uncertainties.

The mean difference between the measurements of the DMMS and the refrigerant scale was calculated using student-t distribution, the continuous probability distribution obtained from Excel's built-in TINV function; it was 2.7 ± 1.7 g at 95% confidence interval with respect to 119 g of the mean measured charge by the refrigerant scale. For further explanation, the DMMS has some advantages over the refrigerant scale; the DMMS can weigh up to 280kg while the refrigerant scale weigh up to 100 kg. Moreover, the DMMS has higher accuracy; Lee, Bach and Bradshaw (2021) reported the DMMS's accuracy of 0.006% with 49.9 kg load, whereas the refrigerant scale has 0.5% of accuracy of reading. In this study, the validated charge measurement method is applied to measure charge of R410A refrigerant.

2.5 Experiment Description

2.5.1 Test Matrix

Utilizing this validated test method, experimental charge measurement tests were executed for both IC1 and OC1 in both evaporator and condenser mode. Table 2.2 and 2.3 show the test matrix using R410A refrigerant. In evaporator mode, refrigerant mass flow rate, $\dot{m}_{ref}$ and outlet superheat, $\Delta T_{sh,out}$ were selected as independent variables. To avoid undesirable charge errors by water condensation, all evaporator tests were conducted under dry conditions, cooling conditions without dehumidification (*e.g.* without condensation on the fins). The condenser tests use a Box-Behnken design of experiments, where refrigerant mass flow rate, $\dot{m}_{ref}$, inlet superheat, $\Delta T_{sh,in}$, and outlet subcooling, $\Delta T_{sc,out}$ were chosen as independent variables at three equally spaced levels (-1, 0, +1). It consists of basic tests designed by Box-Behnken and additional random tests. The combination of indoor and outdoor RTPFs in the test matrix implies operations of both a heat pump and air-conditioner. Accordingly air inlet temperatures are maintained at 21.1℃ dry bulb and 15.4℃ wet bulb temperature in condenser mode for IC1 and 8.3∼13.3 ℃ dry bulb temperature for OC1 in

evaporator mode, representing heat pump operations. Likewise, air inlet temperatures are controlled at 35.0℃ dry bulb and 23.9℃ wet bulb temperature for OC1 in condenser mode and 26.7 ℃ dry bulb temperature for IC1 in evaporator mode, referring to air-conditioner operations.

Table 2.2: Test matrix for IC1

Test number	Test mode	$\dot{m}_{ref}$		ΔT_{sh}		ΔT_{sc}		Note
		level	(kg/h)	level	(K)	level	(K)	
IC1-1	Evaporator	-1	34.0	0	2.8	-	-	
IC1-2		-1	34.0	+1	11.1	-	-	
IC1-3		0	79.4	0	2.8	-	-	
IC1-4		0	79.4	+1	11.1	-	-	
IC1-5		+1	113.4	0	2.8	-	-	
IC1-6		+1	113.4	+1	11.1	-	-	
IC1-7	Condenser	-1	22.7	-1	16.7	0	6.9	Box-Behnken Design of Experiment
IC1-8		-1	22.7	+1	33.3	0	6.9	
IC1-9		-1	22.7	0	25.0	-1	2.8	
IC1-10		+1	90.7	0	25.0	-1	2.8	
IC1-11		+1	90.7	-1	16.7	0	6.9	
IC1-12		+1	90.7	+1	33.3	0	6.9	
IC1-13		-1	22.7	0	25.0	+1	11.1	
IC1-14		+1	90.7	0	25.0	+1	11.1	
IC1-15		0	56.7	-1	16.7	-1	2.8	
IC1-16		0	56.7	-1	16.7	+1	11.1	
IC1-17		0	56.7	+1	33.3	-1	2.8	
IC1-18		0	56.7	+1	33.3	+1	11.1	
IC1-19		0	56.7	0	25.0	0	6.9	
IC1-20		59.4		17.8		5.6		Random Points
IC1-21		77.1		18.9		2.8		
IC1-22		52.6		26.7		9.4		

Table 2.3: Test matrix for OC1

Test number	Test mode	$\dot{m}_{ref}$		ΔT_{sh}		ΔT_{sc}		Note
		level	(kg/h)	level	(K)	level	(K)	
OC1-1	Evaporator	-1	45.4	0	2.8	-	-	
OC1-2		-1	45.4	+1	11.1	-	-	
OC1-3		0	136.1	0	2.8	-	-	
OC1-4		0	136.1	+1	11.1	-	-	
OC1-5		+1	181.4	0	2.8	-	-	
OC1-6		+1	181.4	+1	11.1	-	-	
OC1-7	Condenser	-1	68.0	-1	16.7	0	6.9	Box-Behnken Design of Experiment
OC1-8		-1	68.0	+1	33.3	0	6.9	
OC1-9		-1	68.0	0	25.0	-1	2.8	
OC1-10		+1	226.8	0	25.0	-1	2.8	
OC1-11		+1	226.8	-1	16.7	0	6.9	
OC1-12		+1	226.8	+1	33.3	0	6.9	
OC1-13		-1	68.0	0	25.0	+1	11.1	
OC1-14		+1	226.8	0	25.0	+1	11.1	
OC1-15		0	147.4	-1	16.7	-1	2.8	
OC1-16		0	147.4	-1	16.7	+1	11.1	
OC1-17		0	147.4	+1	33.3	-1	2.8	
OC1-18		0	147.4	+1	33.3	+1	11.1	
OC1-19		0	147.4	0	25.0	0	6.9	
OC1-20		135.7		27.4		9.3		Random Point

2.5.2 Data Reduction

This section introduces the data reduction processes for determining the charge of the RTPF, uncertainties associated with it, and other variables of interest. The paramount quantity of interest is the charge in an RTPF, m_{RTPF}; it is calculated as

$$m_{RTPF} = m_{RHXCT} - m_{AUX} \tag{2.9}$$

where m_{RHXCT} is the charge inside the RHXCT and m_{AUX} is the charge inside the RHXCT excluding the charge m_{RTPF} in the RTPF.

Depending on charge weight, m_{RHXCT} is defined differently to allow extending the range of the DMMS's load cell.

In the simplest case, when the charge is expected within the load cell's limit (1,000

g), m_{RHXCT} is given as

$$m_{RHXCT} = \Delta m_{CW} - \Delta m_{TW} \tag{2.10}$$

where Δm_{CW} is the measured differential mass of charge sampled RHXCT's weight by DMMS and Δm_{TW} is the tare weight of the measured differential mass of RHXCT by the DMMS.

When the expected charge exceeds the load cell's limit (1,000 g), m_{RHXCT} is given as

$$m_{RHXCT} = \Delta m_{CW} + m_{off} - \Delta m_{TW} \tag{2.11}$$

where m_{off} is an offset weight, a standard mass, to offset the counter weight allowing an increase in measured charge range. Figure 2.22 depicts the measurement process of Δm_{CW} and Δm_{TW} depending on charge weight, and Table A.6-A.8 in Appendix list the refrigerant charge in the RTPF, RHXCT, intermediate charges, and the associated uncertainties in both evaporator and condenser mode.

The DMMS determines the differences between mass (Δm); thus m_{RHXCT} is obtained by the difference between the two differential mass measurements as shown in Equation 2.10 or 2.11. Note that, with the same m_{RHXCT}, Δm_{CW} and Δm_{TW} can change depending on the counter weight (*e.g.* if instrumentation or other mass is added to the RHXCT between tests).

Next, m_{AUX} comprises the sum of multiple charges according to each refrigerant state as listed in Table A.5-A.8 in Appendix; and they are defined as the product of each density and volume, given in Figure A.1-A.4 in Appendix. The internal volumes are obtained from the validated volume measurement method.

For evaporator mode, m_{AUX} is calculated as

$$m_{AUX} = m_{vap} + m_{vap,cap} + m_{liq} + m_{tp} \tag{2.12}$$

while for condenser mode, m_{AUX} is calculated as

$$m_{AUX} = m_{vap} + m_{liq} + m_{liq,cap} \tag{2.13}$$

where m_{vap} is the charge in superheated vapor state, m_{liq} is the charge in subcooled liquid state, m_{tp} is the charge in two-phase state, and $m_{vap,cap}$ and $m_{liq,cap}$ are the charges inside capillary pipes in vapor and liquid state respectively.

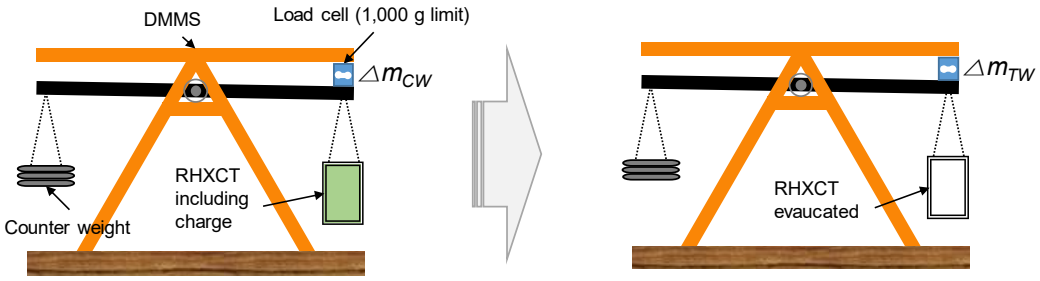

(a) Charge within the load cell's limit

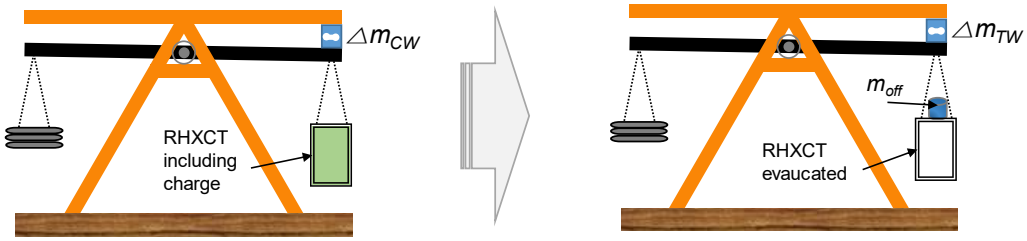

(b) Charge out of the load cell's limit

Figure 2.22: Schematic diagram of Δm_{CW} and Δm_{TW} measurement depending on charge weight

The capillary pipe charges are estimated as single phase (*e.g.* superheated or subcooled) because of the temperature relative to the ambient air temperature. The small internal volume of the capillary pipe leads to an estimated mass of less than 0.2% in evaporator mode (*e.g.* IC-1) and less than 1.1% in condenser mode (*e.g.* IC-13), relative to m_{RTPF} .

The uncertainties associated with the RTPF charge, $u_{m_{RTPF}}$ are defined as follows:

$$u_{m_{RTPF}} = \sqrt{(u_{m_{RHXCT}})^2 + (u_{m_{AUX}})^2}. \tag{2.14}$$

where $u_{m_{RHXCT}}$, $u_{m_{AUX}}$ are the uncertainties associated with m_{RHXCT} and m_{AUX} respectively.

The uncertainty of m_{RHXCT},$u_{m_{RHXCT}}$, is expressed as

$$u_{m_{RHXCT}} = \sqrt{(u_{\Delta m_{TW}})^2 + (u_{\Delta m_{CW}})^2 + (u_{m_{RSV}})^2} \tag{2.15}$$

The uncertainty of the charge inside the RHXCT, $u_{m_{RHXCT}}$, results from the measurement of the tare weight and charge sampled weight and the RSV. The resulting charge uncertainty caused by actuation of the RSV, $u_{m_{RSV}}$, is calculated by multiplying the refrigerant flow rate and a mean closing time difference between the two RSVs. To estimate this time difference, slow motion video of repeated manual closing of the two RSVs was recorded. It was found that the mean closing time difference between the two RSVs was 0.02 seconds; this value is applied to calculate the $u_{m_{RSV}}$. The uncertainty of the measured differential mass of RHXCT's tare weight by DMMS, $u_{\Delta m_{TW}}$, is determined by a root sum squared of the measurement's random uncertainty and the maximum absolute error of the DMMS which was found in validation process of the DMMS. Similarly, the uncertainty of the measured differential mass of charge sampled RHXCT's weight by DMMS, $u_{\Delta m_{CW}}$, is also determined the same way as $u_{\Delta m_{TW}}$.

$u_{m_{AUX}}$ is determined depending on testing mode. For the evaporator mode, $u_{m_{AUX}}$ is calculated as

$$u_{m_{AUX}} = \sqrt{(u_{m_{vap}})^2 + (u_{m_{liq}})^2 + (u_{m_{tp}})^2} \tag{2.16}$$

For the condenser mode, $u_{m_{AUX}}$ is calculated as

$$u_{m_{AUX}} = \sqrt{(u_{m_{vap}})^2 + (u_{m_{r,liq}})^2} \tag{2.17}$$

Uncertainties in each refrigerant phase are given using a relative uncertainty of each volume corresponding to each refrigerant state, and the following is an example for $u_{m_{vap}}$:

$$u_{m_{vap}} = \frac{u_{V_{vap}}}{V_{vap}} \cdot m_{vap} \tag{2.18}$$

where $u_{V_{vap}}$ is the measurement uncertainty of the volume occupied by the vapor refrigerant in m_{AUX}, V_{vap} is the volume occupied by the vapor refrigerant in m_{AUX}, and m_{vap} is the vapor-refrigerant mass in m_{AUX}.

Uncertainties of charge inside the capillary pipes are neglected due to their small amount: ± 0.002 g in evaporator mode, ± 0.04 g in condenser mode, applying average relative uncertainty of the RHXCT volume to the capillary charge.

Vital heat exchanger testing variables are presented: the refrigerant side capacity, $\dot{Q}_{ref}$, air side capacity, $\dot{Q}_{air}$, outlet superheat, SH_{out}, inlet superheat, SH_{in}, outlet subcooling, SC_{out}, are expressed as

$$\dot{Q}_{ref} = \dot{m}_{ref} \cdot (h_{r,o} - h_{r,i}) \tag{2.19}$$

$$\dot{Q}_{air} = \dot{m}_{air} \cdot c_p \cdot (T_{db,i} - T_{db,o}) \tag{2.20}$$

$$\Delta T_{sh,out} = T_{r,o} - T_{r,sat,o} \tag{2.21}$$

$$\Delta T_{sh,in} = T_{r,i} - T_{r,sat,o} \tag{2.22}$$

$$\Delta T_{sc,out} = T_{r,sat,o} - T_{r,o} \tag{2.23}$$

where $\dot{m}_{ref}$ is the refrigerant flow rate, $h_{r,o}$ is the refrigerant enthalpy at the RTPF outlet, $h_{r,i}$ is the refrigerant enthalpy at the RTPF inlet, $\dot{m}_{air}$ is the air flow rate, c_p is the specific heat at constant pressure of air-water vapor mixture, $T_{db,i}$ is the inlet air dry-bulb temperature, $T_{db,o}$ is the outlet air dry-bulb temperature, $T_{ref,o}$ is the refrigerant temperature at the RTPF outlet, $T_{r,sat,o}$ the saturated refrigerant temperature at the RTPF outlet, and $T_{ref,i}$ the refrigerant temperature at the RTPF inlet.

The developed charge measurement method is validated and sufficiently reliable to produce experimental charge validation data repeatedly. The following chapters present experimental results obtained using this method.

2.6 Experimental Test Results

The validated differential mass evacuation sampling method was used to produce experimental charge validation data. The refrigerant and air side test results and the corresponding RTPF charges are presented in Tables A.9-A.12. They were reduced in accordance with the predefined data reduction method. Figures 2.23 and 2.24 display the measured charges of IC1 and OC1 RTPF, respectively.

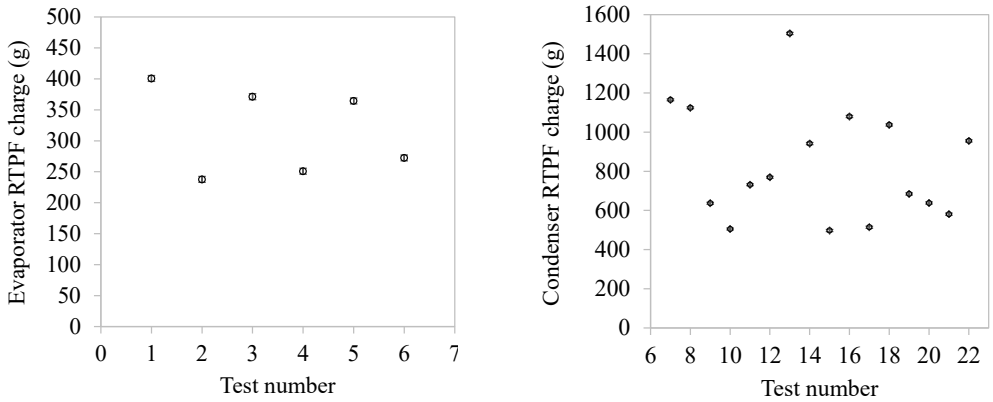

(a) (b)

Figure 2.23: Measured IC1 RTPF charges: (**a**) evaporator mode, (**b**) condenser mode. Error bars are similar to marker size, zoom in for detail

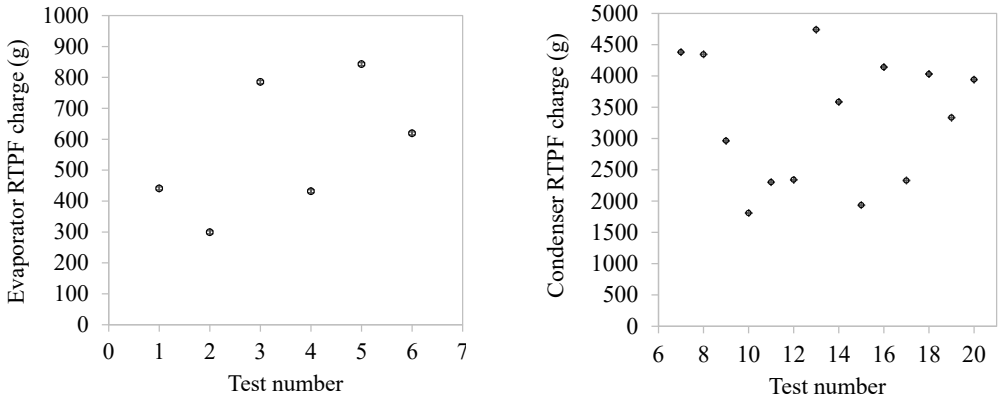

(a) (b)

Figure 2.24: Measured OC1 RTPF charges: (**a**) evaporator mode, (**b**) condenser mode. Error bars are similar to marker size, zoom in for detail

2.6.1 Energy Balance and Uncertainties

All the conducted tests fulfill the 5% energy balance requirement of ASHRAE Standard 33 (ASHRAE, 2016) as presented in Figure 2.25. Table 2.4 presents the obtained uncertainties of all test data; and the uncertainties of air mass flowrate and refrigerant and air capacity are calculated by a Python code which is developed by Saleem et al. (2020) based on ASME PTC 19.1 (ASME-PTC-19.1, 2013).

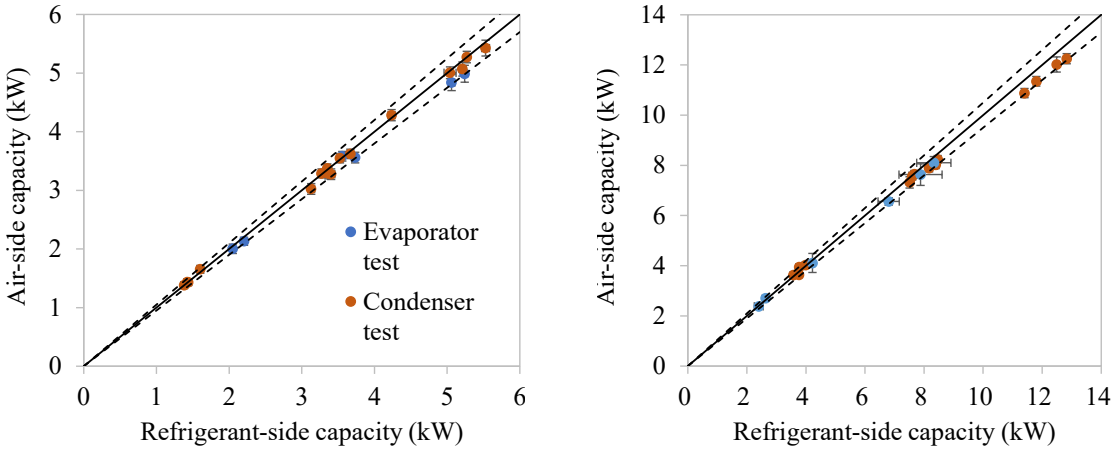

(a) IC1 (b) OC1

Figure 2.25: Measured capacities. The error bars and the dotted lines indicate measurement uncertainties and 5% energy balance limit, respectively.

Table 2.4: Maximum uncertainties of the experimental tests

Parameter	Symbol	Uncertainty
Pressure	P	±1.7 kPa
Temperature	T	±0.06 °C
Refrigerant mass flow rate	$\dot{m}_{ref}$	±0.05% of measured
Air mass flow rate	$\dot{m}_{air}$	±2.0% of measured
Refrigerant capacity	$\dot{Q}_{ref}$	±0.73 (kW)
Air capacity	$\dot{Q}_{air}$	±0.43 (kW)
Evaporator RTPF charge	$u_{m,RTPF,eva}$	±6.6 (g)
Condenser RTPF charge	$u_{m,RTPF,cnd}$	±6.9 (g)

An uncertainty of charge in an RTPF, $u_{m,RTPF}$ (g) is determined by the predefined method in section 2.5.2. The result discloses that 0.01% of relative uncertainty with

respect to the OC1 RHXCT weight (68.0 kg), 0.2% of relative uncertainty with respect to the measured charge of OC1 found in Table A.4, and 2.0% of maximum relative uncertainty with respect to the measured RTPF charge of IC1, shown in Table A.1, which is considered sufficiently accurate for model validation purposes by the author. Further details on the uncertainties of air mass flowrate, refrigerant, and air capacity are previously presented in Saleem et al. (2020).

2.6.2 Repeatability of Charge Measurement

Repeatability (*i.e.* precision) is a significant measure for experiment capability of reproducing data under the same testing condition; a repeatability of charge measurement is calculated as

$$Repeatability = 100 \times \frac{abs(m_{RHXCT-1st} - m_{RHXCT-2nd})}{mean(m_{RHXCT-1st}, m_{RHXCT-2nd})} \,(\%) \tag{2.24}$$

where $m_{RHXCT-1st}$ is the first measurement of m_{RHXCT}; likewise $m_{RHXCT-2nd}$ is the second measurement of m_{RHXCT} for the same test point.

A low repeatability indicates high precision of experimental charge validation data. Repeatability of charge measurement in both condenser and evaporator mode were evaluated by repeatedly testing the same test points, including an entire testing-sampling-measurement process.

The results are tabulated in Tables 2.5 $\sim$ 2.8 for both testing mode and RTPFs; the results prove high-quality of experimental data, producing up to 1.3% of repeatability. In general, condenser tests tend to has better repeatability compared to evaporator tests since charges in condenser are greater than that in evaporator. Besides, IC1 tests' repeatability shows better precision than that of OC1 tests; it is deemed that the repeatability of IC1 is improved because IC1 RHXCT is lighter than OC1 RHXCT (*i.e.* 49.9 kg of IC1 RHXCT and 68.0kg of OC1 RHXCT).

Table 2.5: Repeatability of charge measurement for IC1 in evaporator mode

Variable	**Unit**	**IC1-4**	**Repeated test on IC1-4**	**Absolute difference**	**Repeatability (%)**
$\dot{m}_{ref}$	kg/hr	75.8	75.8	0	-
$\dot{m}_{air}$	kg/s	0.437	0.435	0	-
$\dot{Q}_{ref}$	kW	3.56	3.56	0	-
$\dot{Q}_{air}$	kW	3.58	3.45	0.1	-
$\Delta T_{sh,out}$	K	11	11	0	-
m_{RHXCT}	g	355	345	11	2.9

Table 2.6: Repeatability of charge measurement for IC1 in condenser mode

Variable	**Unit**	**IC1-19**	**Repeated test on IC1-19**	**Absolute difference**	**Repeatability (%)**
$\dot{m}_{ref}$	kg/hr	56.6	56.6	0	-
$\dot{m}_{air}$	kg/s	0.31	0.311	0	-
$\dot{Q}_{ref}$	kW	3.4	3.4	0	-
$\dot{Q}_{air}$	kW	3.28	3.29	0	-
$\Delta T_{sh,in}$	K	25.5	25.5	0	-
$\Delta T_{sc,out}$	K	6.7	6.8	0.1	-
m_{RHXCT}	g	971	984	13	1.3

Table 2.7: Repeatability of charge measurement for OC1 in evaporator mode

Variable	**Unit**	**OC1-1**	**Repeated test on OC1-1**	**Absolute difference**	**Repeatability (%)**
$\dot{m}_{ref}$	kg/hr	58.5	58.7	0.2	-
$\dot{m}_{air}$	kg/s	0.816	0.818	0	-
$\dot{Q}_{ref}$	kW	2.64	2.61	0	-
$\dot{Q}_{air}$	kW	2.71	2.61	0.1	-
$\Delta T_{sh,out}$	K	3.9	3.1	0.8	-
m_{RHXCT}	g	509	572	63	11.7

Table 2.8: Repeatability of charge measurement for OC1 in condenser mode

Variable	**Unit**	**OC1-19**	**Repeated test on OC1-19**	**Absolute difference**	**Repeatability (%)**
$\dot{m}_{ref}$	kg/hr	147.4	147.9	0.5	-
$\dot{m}_{air}$	kg/s	0.962	0.962	0	-
$\dot{Q}_{ref}$	kW	8.17	8.19	0	-
$\dot{Q}_{air}$	kW	7.89	7.95	0.1	-
$\Delta T_{sh,in}$	K	25.6	25.4	0.2	-
$\Delta T_{sc,out}$	K	7.4	7.5	0.1	-
m_{RHXCT}	g	3501	3550	49	1.4

2.6.3 Charge Sensitivity

Charge sensitivity on refrigerant charge was investigated from experimental data. The Pearson correlation coefficient is applied to analyze inter-relation strength between charge and variables. According to Meng-ting et al. (2019), the Pearson correlation coefficient, also known as r value, indicates correlation intensity; it is expressed as

$$r = \frac{\sum (x - \overline{x})(y - \overline{y})}{\sqrt{\sum (x - \overline{x})^2 \sum (y - \overline{y})^2}} \tag{2.25}$$

Where X_i and Y_i are *i-th* sample of variable X and Y, $\overline{X}$ and $\overline{Y}$ are averages for X and Y, respectively. The minimum value of Pearson correlation coefficient is -1 and represents a complete negative correlation; inversely, the maximum value of Pearson correlation coefficient is 1 and denotes a complete positive correlation; when the value is 0, there is no correlation between the two variables (*i.e.* the variables vary in a random manner with respect to each other).

2.6.3.1 IC1 in Evaporator Mode

Figure 2.26 shows the result of charge sensitivity on $\Delta T_{sh,out}$ and $\dot{m}_{ref}$ as well as X_{in} from IC1 evaporator tests. According to the result, the IC charge, m_{RTPF} has a strong correlation to both X_{in} and $\Delta T_{sh,out}$ as presented in Figure 2.27.

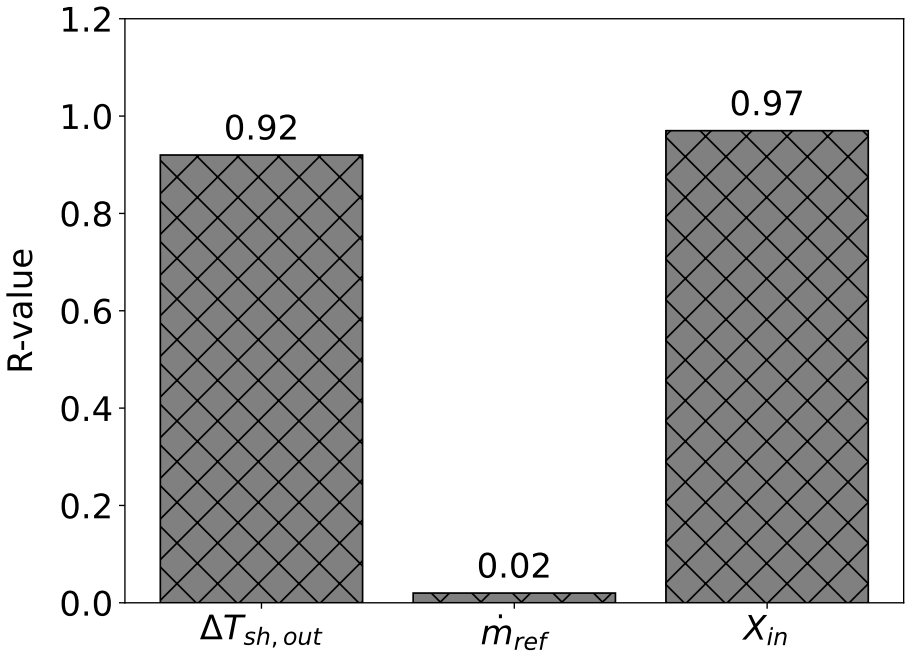

Figure 2.26: Absolute Pearson correlation coefficients for m_{RTPF} from the IC1 test results in the evaporator mode

In contrast, $\dot{m}_{ref}$ has a weak correlation to the IC charge, m_{RTPF}; to be specific, Figure 2.28 demonstrates an intensive correlation between $\dot{m}_{ref}$ and X_{in} regardless of variations of $\dot{m}_{ref}$.

As a result, it is found that increase in $\Delta T_{sh,out}$ and X_{in} yields charge reduction. This effect on charge can be explained considering contraction of two-phase region in an evaporator since two-phase region has higher density than that of superheated region (Hervas-Blasco et al., 2018).

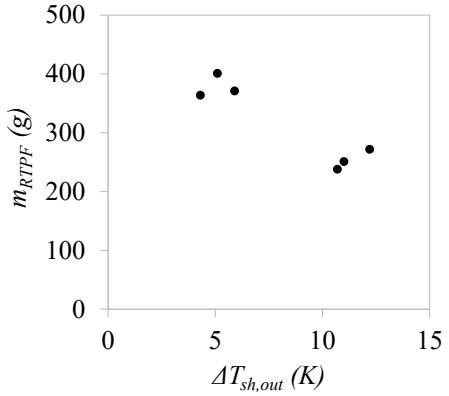

(a) Charges with respect to $\Delta T_{sh,out}$

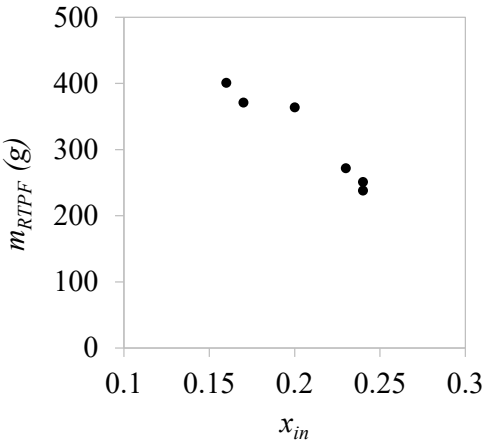

(b) Charges with respect to X_{in}

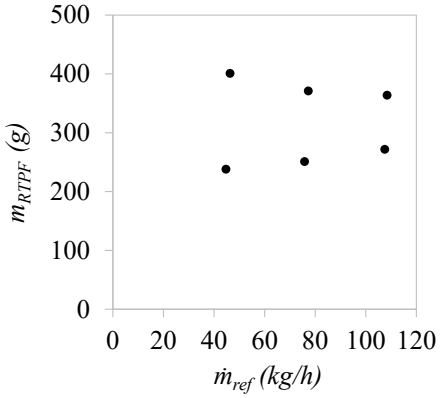

(c) Charges with respect to $\dot{m}_{ref}$

Figure 2.27: IC1 m_{RTPF} variations to variables in evaporator mode of pure R410A

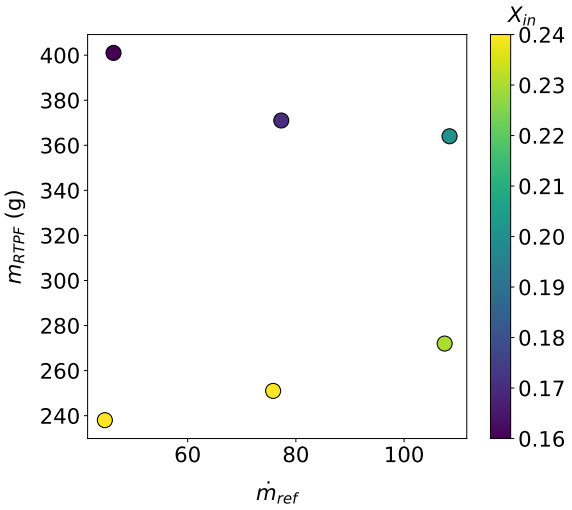

Figure 2.28: IC1 m_{RTPF} and $\dot{m}_{ref}$ with respect to X_{in} in evaporator mode of pure R410A

2.6.3.2 IC1 in Condenser Mode

For IC1 condenser tests, Figure 2.29 presents a charge sensitivity result about effects of $\Delta T_{sh,in}$, $\Delta T_{sc,out}$, and $\dot{m}_{ref}$ on charge.

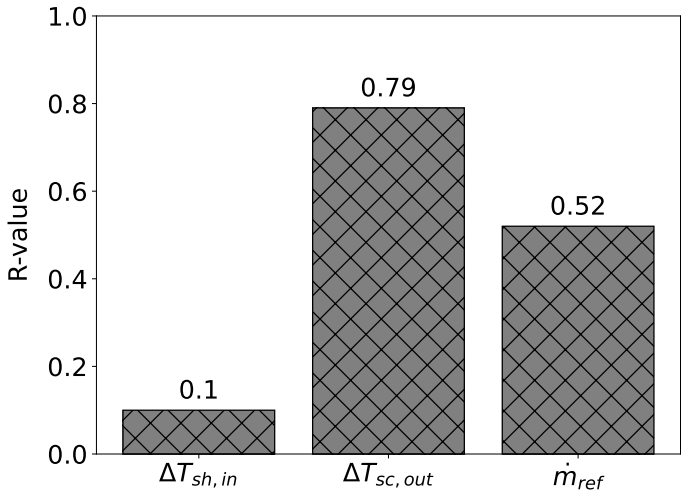

Figure 2.29: Absolute Pearson correlation coefficients for m_{RTPF} from the IC1 test results in the condenser mode

It is observed that the IC1 charge, m_{RTPF} has a strong positive correlation to $\Delta T_{sc,out}$ and $\dot{m}_{ref}$ and a weak correlation to $\Delta T_{sh,in}$, as indicated in Figure 2.30. In accordance with the calculated Pearson correlation coefficients, $\Delta T_{sc,out}$ is a dominant

factor to dictate charge in condenser mode; it is known that higher $\Delta T_{sc,out}$ induces larger subcooled region, thus leading a higher charge (Li et al., 2020).

Besides, the charge is influenced by $\dot{m}_{ref}$ as well. Pereira et al. (2019) also reported a lower charge trend along with higher $\dot{m}_{ref}$ in a coaxial tube condenser. According to their claim, this trend could be led by a flow-pattern change since higher $\dot{m}_{ref}$ promote a transition of flow pattern to an annular flow which has higher void fraction (Wojtan et al., 2005). Therefore, it can be seen that the high $\dot{m}_{ref}$ leads to low charge.

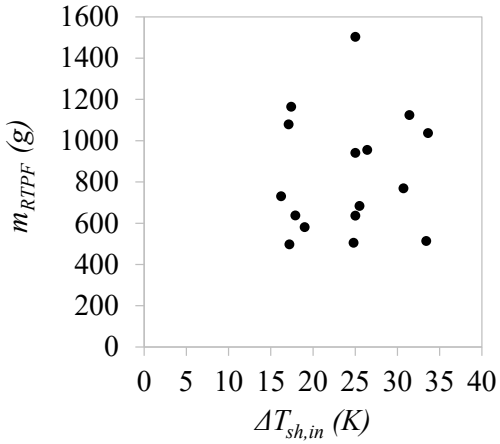

(a) Charges with respect to $\Delta T_{sh,in}$

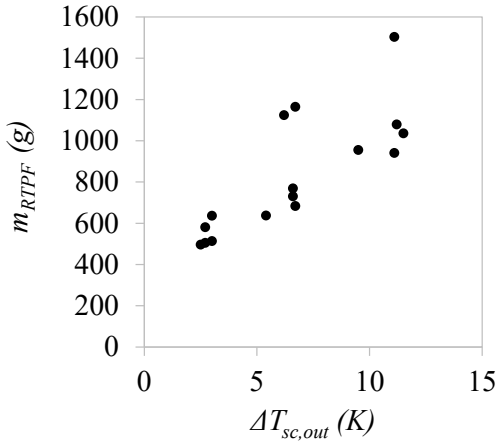

(b) Charges with respect to $\Delta T_{sc,out}$

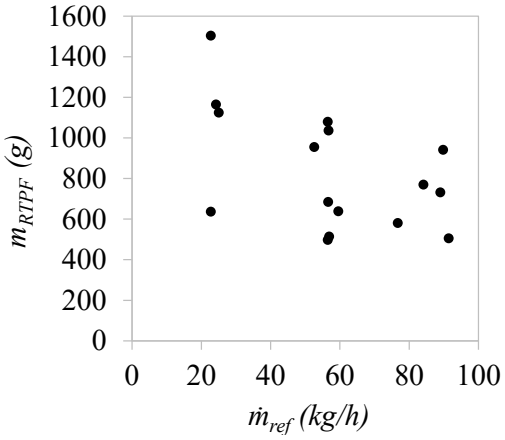

(c) Charges with respect to $\dot{m}_{ref}$

Figure 2.30: IC1 m_{RTPF} variations to variables in condenser mode of pure R410A

2.6.3.3 OC1 in Evaporator Mode

As with the IC1 evaporator test results, the OC1 evaporator tests confirm that the most charge-correlated variable is a refrigerant inlet quality, X_{in} followed by refrigerant mass flow rate, $\dot{m}_{ref}$ and outlet superheat, $\Delta T_{sh,out}$ as shown in Figure 2.31 and 2.32.

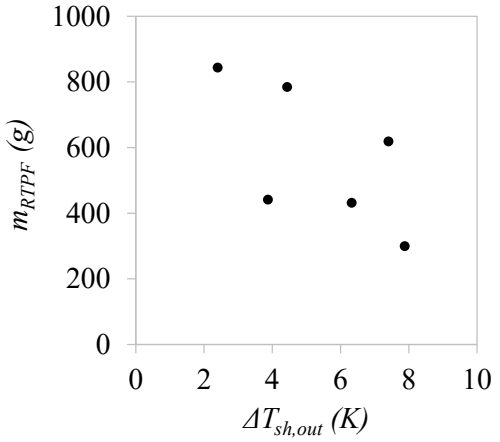

(a) Charges with respect to $\Delta T_{sh,out}$

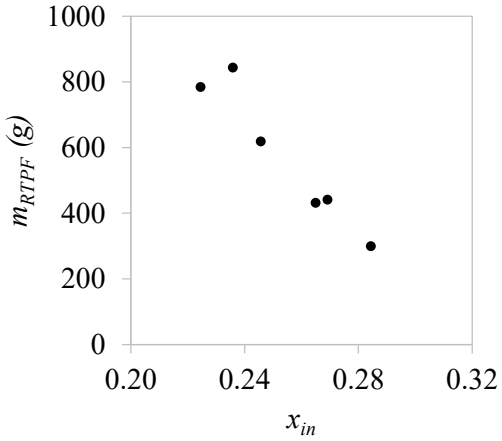

(b) Charges with respect to X_{in}

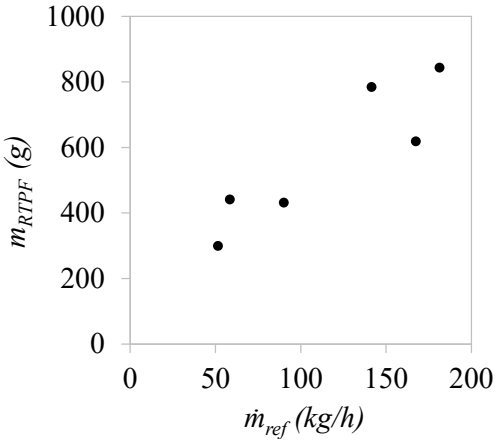

(c) Charges with respect to $\dot{m}_{ref}$

Figure 2.31: OC1 m_{RTPF} variations to variables in evaporator mode of pure R410A

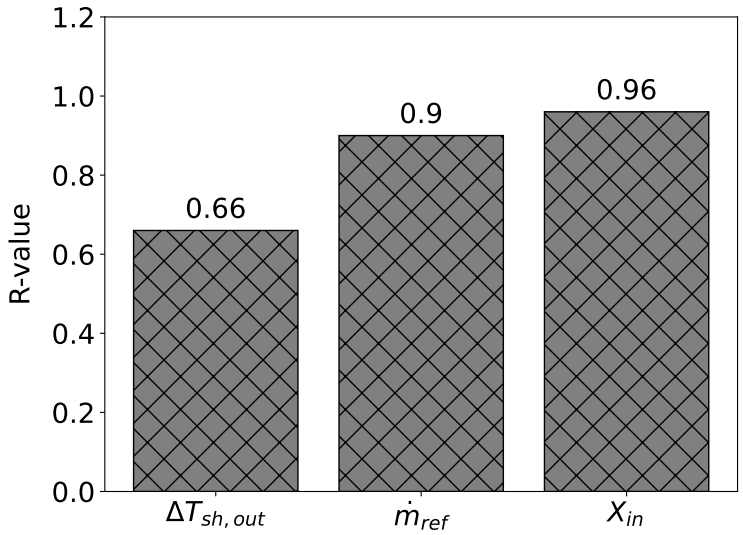

Figure 2.32: Absolute Pearson correlation coefficients for m_{RTPF} from the OC1 test results in the evaporator mode

2.6.3.4 OC1 in Condenser Mode

The charge sensitivity on the variables for IC1 condenser tests continues to OC1 condenser test results as depicted in Figure 2.33 and 2.34.

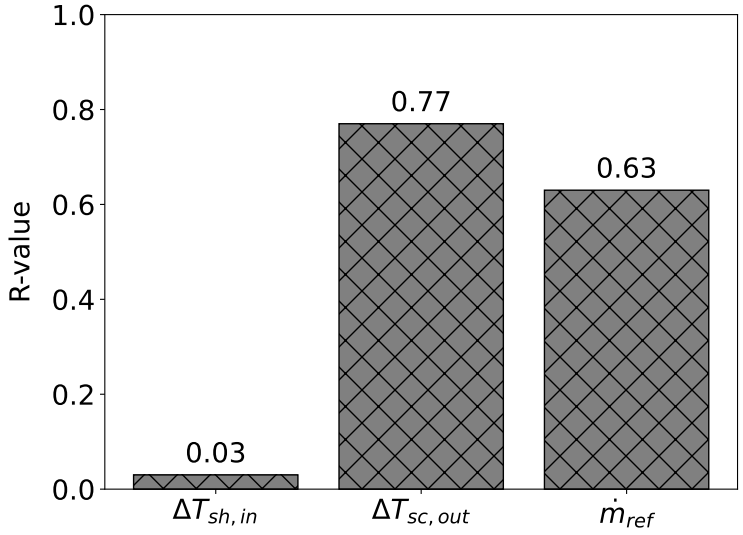

Figure 2.33: Absolute Pearson correlation coefficients for m_{RTPF} from the OC1 test results in the condenser mode

As the calculated Pearson correlation coefficients indicate, $\Delta T_{sc,out}$ is a main factor with strong positive correlation, followed by $\dot{m}_{ref}$ with negative correlation. $\Delta T_{sh,in}$ has a weak correlation to the charge.

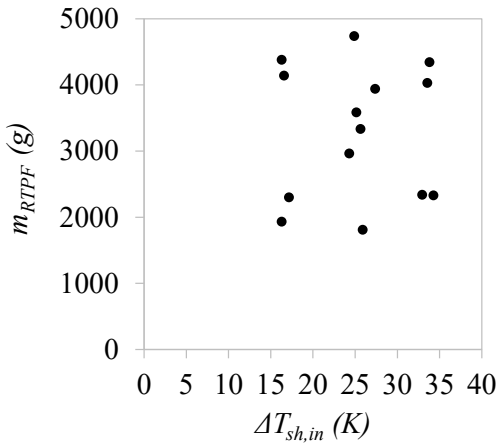

(a) Charges with respect to $\Delta T_{sh,in}$

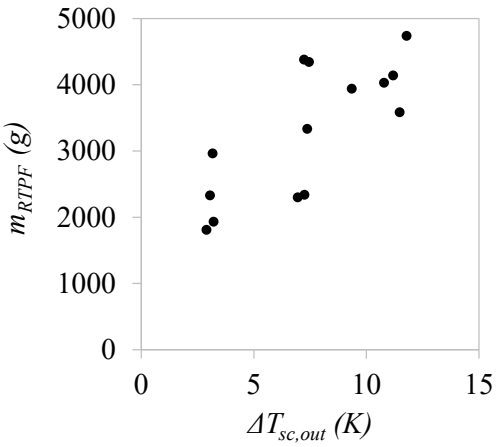

(b) Charges with respect to $\Delta T_{sc,out}$

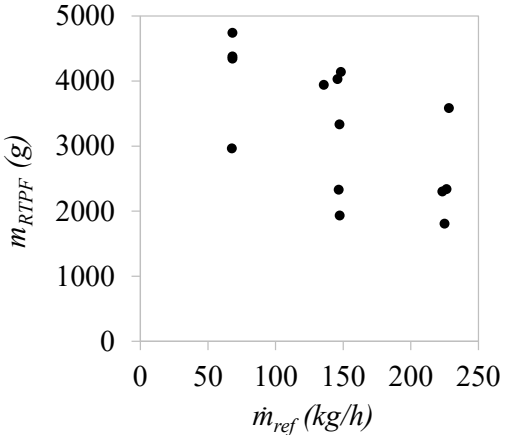

(c) Charges with respect to $\dot{m}_{ref}$

Figure 2.34: OC1 m_{RTPF} variations to variables in condenser mode of pure R410A

The obtained high-fidelity charge data for the RTPFs is crucial to improve accuracy of charge model that will be addressed in the following sections; moreover, the charge validation data is a stepping stone to further investigate charge prediction and optimization.

2.7 Conclusion

A differential mass evacuation sampling method is developed that can quickly (*i.e.* within an hour) capture high-fidelity charge measurements for experimental validation of the charge simulation. This method embraces the advantages of the existing charge measurement methods (OM and SM) such as independent charge determination of refrigerant and oil and simple/fast measurement to accommodate large number of data points. Main testing apparatuses were developed: the RHXCT to enable rapid charge sampling, individual circuit control, repetitive weighing, and oil separation, the MDA to generate a uniform airflow, and the DMMS for accurate measurement of weight. A validation of the differential mass evacuation sampling method was performed and it disclosed an error of 2.7 ± 1.7 g at 95% confidence interval with respect to 119 g of the mean measured charge by a refrigerant scale. Using the validated method, a total of 42 experimental charge tests were carried out according to the test matrix using R410A refrigerant, producing up to a 0.01% of relative uncertainty with respect to the OC1 RHXCT weight, 0.1% of relative uncertainty with respect to measured charge of OC1, and 1.3% of charge measurement repeatability with respect to measured charge of IC1; it is considered sufficiently accurate for charge validation purposes by the author.

The conducted charge sensitivity study reveals correlation intensities between charge and variables in different operating mode; X_{in} is strongly correlated with charge in evaporator mode. In condenser mode, $\Delta T_{sc,out}$ followed by $\dot{m}_{ref}$ are main factors to affect charge. The collected experimental charge validation data addresses the need, lack of charge validation data; and leads to a development of an experimentally validated charge model.

CHAPTER III

AN EXPERIMENTAL DATA-DRIVEN CHARGE MODEL FOR ROUND-TUBE-PLATE-FIN HEAT EXCHANGERS USING LOW-GWP REFRIGERANTS

Abstract

Heat pumps can be switched between cooling and heating mode, requiring accurate charge modelling capabilities to enable design of heat exchangers for near optimum efficiency in both operating modes. The charge modeling tools also require high-fidelity experimental validation data to tune their predictions. However, very few experimental charge validation data are available in the open literature. This study addresses this need by providing complete and high-fidelity experimental charge data of Round Tube Plate Fin Heat Exchangers (RTPF) with ±2.2% of relative-charge measurement uncertainty of measured and 0.8% of charge-measurement repeatability. Especially, in addition to R410A data, two low-Global Warming Potential (GWP) refrigerants charge data are collected such as R1234yf and R468C. Furthermore, an accurate data-driven charge model is developed, tuned by the high-fidelity experimental charge data with 12.3%, 12.8%, and 12.9% of the Mean Absolute Percentage Error (MAPE) based on the Taitel-Barnea, the Zivi, and the Baroczy void-fraction model, respectively. This experimentally validated charge model can contribute to enable effective designs of heat pumps with high-accuracy charge predictions.

This chapter will be submitted for publication in the International Journal of Refrigeration.

3.1 Introduction

Refrigerant charge plays a significant role in air-conditioning and refrigeration systems directly affecting efficiency and capacity of the systems (Poggi et al., 2008). A considerable of studies reported changes in capacity and efficiency affected by charge. 20% of capacity reduction and 15% of efficiency degradation led by 25% of charge deficiency in a heat pump were reported (Kim and Braun, 2012). It was found that optimizing refrigerant charge can reduce energy consumption in cooling mode by 5 to 11% for packaged rooftop air conditioning units installed in California (Cowan et al., 2004). Also, heat pumps can be utilized for both space heating and cooling by switching the mode; in the meantime, maintaining proper charge in the heat pump is crucial for capacity and efficiency as well as reliability of the heat pump (Eom et al., 2019).

Furthermore, current refrigerants have high-Global Warming Potential (GWP) such as 2088 of R410A. As a result, worldwide effort has been made to reduce carbon footprint with respect to refrigerants; Kigali Amendment to the Montreal Protocol includes the common Hydrofluorocarbon (HFC) refrigerants to progressively lower their production and consumption (Heath, 2017). To keep pace with this, the Heating, Ventilation, Air-conditioning, and Refrigeration (HVAC&R) society is rapidly adopting low-GWP refrigerants. For these reasons, accurate prediction of charge is vital for air-conditioning and refrigeration systems (Poggi et al., 2008). The refrigerant charge in an air-conditioning and refrigeration system can be predicted by charge modeling tools (Harms, 2002; Ding et al., 2009; Jin and Hrnjak, 2016).

Major difficulties in charge predictions are uncertainties of the ratio of vapor to liquid in two-phase flow, *e.g.* void fraction (Harms et al., 2003). To account for the void fraction, early charge models assumed equal liquid and vapor velocities, *i.e.* a slip ratio of 1, also known as the homogeneous void-fraction model (MacArthur, 1984). Subsequently, researchers introduced a wide variety of slip ratios using either

empirical or analytical derivations to deal with the void fraction (Abdelaziz et al., 2008); yet the majority of them were developed by water and steam flow; some of them are developed even under adiabatic conditions, thus they might not be always proper for refrigerants (Shen et al., 2006).

Meanwhile, before 1980s, system performance was the prime factor of interest in the HVAC&R society; and there is little attention to refrigerant charge inventory. Rice (1987)'s study is one of the early studies to draw attention of HVAC&R society to the experimentally validated charge model. Through the study (Rice, 1987), importance of the void-fraction model was recognized and then Hughmark (Hughmark et al., 1962), Premoli (Premoli et al., 1971), Tandon (Tandon et al., 1985), and Baroczy (Baroczy, 1963) model were recommended for their good agreement with measured charge.

Followed by Rice (1987), extensive void-fraction models were experimentally evaluated in various test conditions and capacity for an accurate charge model used in unitary air-conditioners with R22 and R407C (Harms et al., 2003). This investigation on void-fraction models presented that underprediction of charge by the homogeneous slip ratio model and overprediction of charge by the Hughmark model as well as the best agreement with measured charge of the Baroczy void-fraction model. In addition, the simple Zivi void-fraction model (Zivi, 1964) was recommended for its easy implementation and acceptable accuracy of 10% with measured data (Harms et al., 2003).

A charge tuning method assisted by charge measurements to reduce dependency of void-fraction models was developed (Shen et al., 2006); it is a practical two-point charge tuning method to utilize two measurements at two operating conditions, along with a development of charge-tuning coefficients. The two-point tuning method was validated against experimental charge data obtained from a series of test conditions with two different unitary equipment, revealing excellent charge errors within 1%

regardless of void-fraction models. Once a charge model is tuned by this method, the charge model behaves nearly independent of the selected void-fraction model, whereas this two-point tuning method requires experimental charge data and calculations of the charge-tuning coefficients.

Recent charge studies investigated charge distributions in a vapor compression system and developed experimentally validated charge models (Jin and Hrnjak, 2016; Li and Hrnjak, 2021). Jin and Hrnjak (2016) reported that a developed charge model for an air-conditioner using R1234yf and R134a, and presented the error of the refrigerant charge model is reduced from 20% to 15% by accounting for the observed liquid channels in the microchannel heat exchanger and applying a constant correction factor to the Zivi model (Zivi, 1964). Followed by Jin and Hrnjak (2016), R134a refrigerant distributions in a residential heat pump were analyzed by employing the Coddington and Macian (Coddington and Macian, 2002) and the Woldesemayat and Ghajar (Woldesemayat and Ghajar, 2007) void-fraction models (Li and Hrnjak, 2021). It was observed that the heat exchangers hold most of the charge in the heat pump. The study presented 9.1% of charge prediction error evaluated by the experimental charge in the evaporator.

The aforementioned charge studies in HVAC&R are listed in Table 3.1. In summary, the literature review suggests unlike rapid adoption of low-GWP refrigerants by HVAC&R society, experimentally validated charge models are insufficient, particularly on low-GWP refrigerants.

Table 3.1: Selected charge studies in HVAC&R

	Rice (1987)	Harms et al. (2003)	Jin and Hrnjak (2016)	Li and Hrnjak (2021)
Recommended void-fraction models	(Hughmark et al., 1962) (Premoli et al., 1971) (Tandon et al., 1985) (Baroczy, 1963)	(Baroczy, 1963) (Zivi, 1964)	(Jassim et al., 2006) (Zivi, 1964)	(Coddington and Macian, 2002) (Woldesemayat and Ghajar, 2007)
Achieved charge prediction error	19%	10%	15%	9.1%
Discussed refrigerant	R12, R22	R407C, R22	R134a, R1234yf	R134a

The proposed study fills this gap by providing experimental charge validation data

and an experimentally validated charge model on the low-GWP refrigerants, R468C and R1234yf. The charge model is not only validated, but also provides comparison of void-fraction models. The charge model is tuned by the high-fidelity experimental data-informed tuning methods in which the accuracy of the charge model is appreciably improved by a combination of crucial dimensionless numbers and the data-driven method adaptable to various conditions to be simulated.

An additional unique contribution of this investigation is the novel charge data of R468C. Any charge validation data of R468C has not been reported in the open literature to the best of the author's knowledge. R468C is a significantly promising alternative to R410A due to the fact that R468C has similar thermodynamic and transport properties to those of R410A as well as notably low-GWP (285), 13.6% of R410A GWP as indicated in Table 3.2 (Ghadiri et al., 2022).

Table 3.2: Comparison of characteristics of selected refrigerants

Refrigerant	**GWP**	**Normalized GWP**	**ASHRAE safety class**	**Composition**
R1234yf	4	0.2%	A2L	-
R468C	285	13.6%	A2L	6% R1132a/42% R32/ 52% R1234yf
R410A	2088	100%	A1	50% R32/ 50% R125

3.2 Experimental Methodology

The differential mass evacuation sampling method (Lee et al., 2020) is applied to obtain experimental charge validation data; the method determines the charge in a Round Tube Plate Fin Heat Exchangers (RTPF) by measuring the difference to the dry RTPF weight with a custom designed Differential Mass Measurement Scale (DMMS). The overall measurement process is illustrated in Figure 3.1.

The following sections detail the related testing apparatus and testing procedure of the method, followed by the test matrix and data reduction. Further details on the methodology of the differential mass evacuation sampling method was previously presented in (Lee et al., 2020, 2022) .

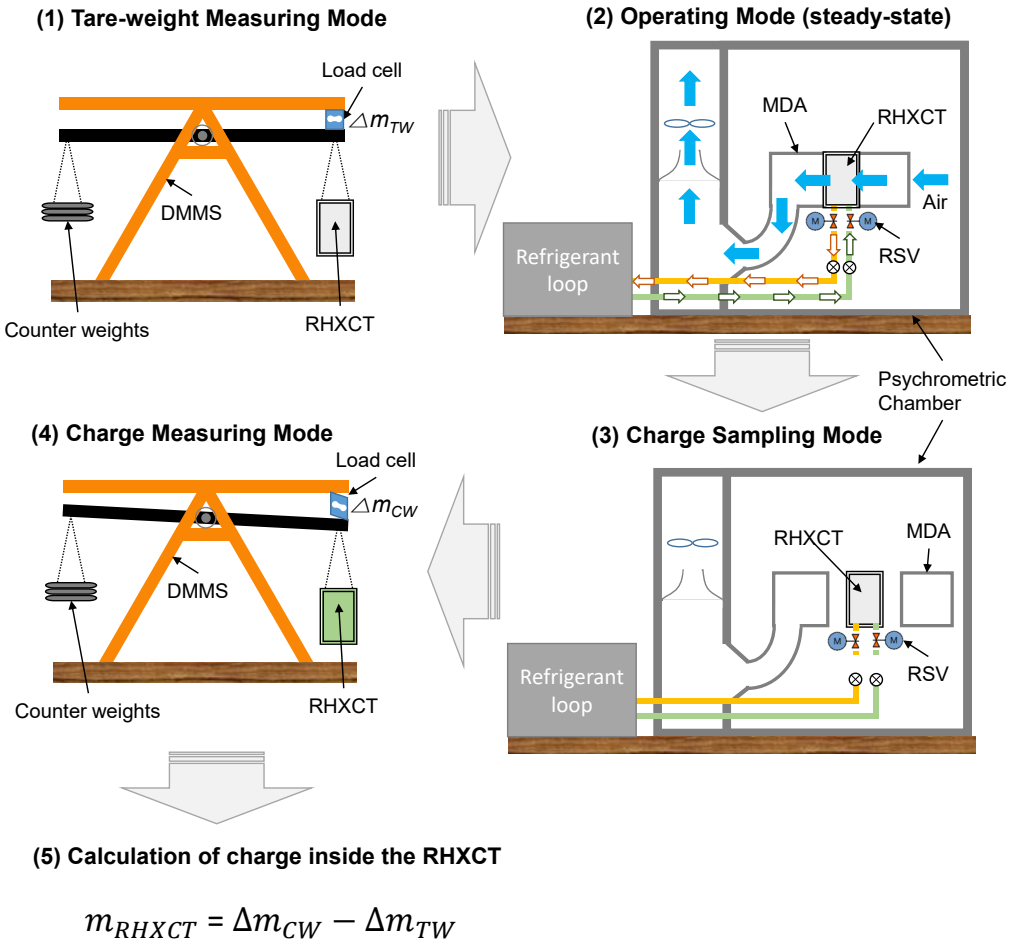

Figure 3.1: Schematic diagram of the overall measurement process (modified from Lee et al. (2020))

3.2.1 Experimental Testing Apparatus

The experimental testing apparatus is divided into three main parts. The first are devices for supplying test conditions such as an air-side conditioning apparatus and a pumped-refrigerant loop. The second is a device for acquiring charge samples and

the third is a scale to determine charge measurements. A schematic diagram of the pumped-refrigerant loop is depicted in Figure 3.2. The refrigerant condition to the inlet of the test section is controlled by the pumped-refrigerant loop equipped with a variable speed diaphragm pump with 7.7 l/m flow capacity at 172 bar, 21.1 kW of heat pumps, and a 18 kW of variable-capacity water heater. These are developed by Saleem et al. (2020).

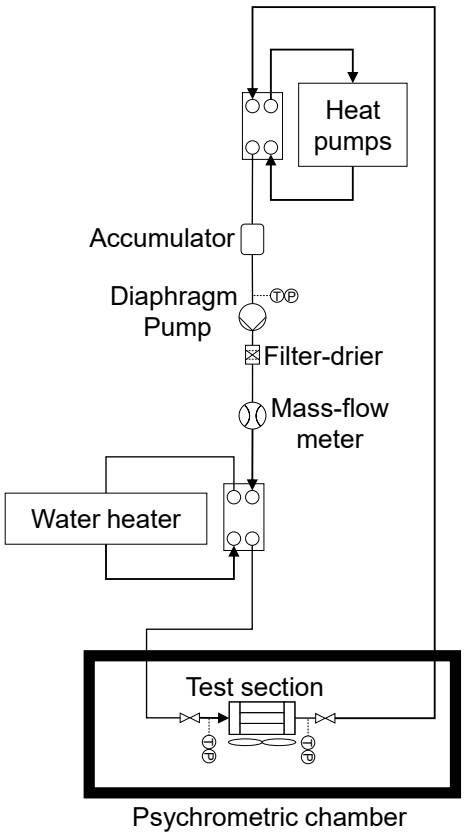

Figure 3.2: Schematic diagram of the pumped-refrigerant loop (modified from Saleem et al. (2020))

The air-side condition is controlled by a psychrometric chamber (Lifferth, 2009), allowing precise control of humidity and temperature of air as well as air flowrate. The conditioned air flowrate is delivered through a Modular Duct Assembly (MDA) — modified from Saleem et al. (2020) — to the Removable Heat Exchanger Charge

Test Module (RHXCT), the test section, as shown in Figure 3.1 and 3.3.

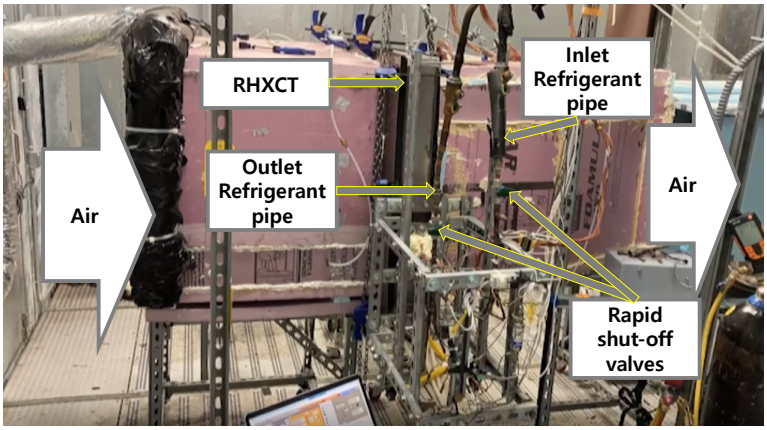

Figure 3.3: Modular Duct Assembly (MDA) combined with the Removable Heat eXchanger Charge Test module (RHXCT) inside a psychrometric chamber

The Removable Heat Exchanger Charge Test Module (RHXCT) that includes the RTPF under test is the principal device to sample charges; it is equipped with pressure and temperature sensors, electronic expansion valves, Rapid Shut-off Valves (RSVs) on both inlet and outlet refrigerant pipes in the RHXCT for quick charge sampling. Figure 3.4 shows a simplified schematic diagram of the RHXCT.

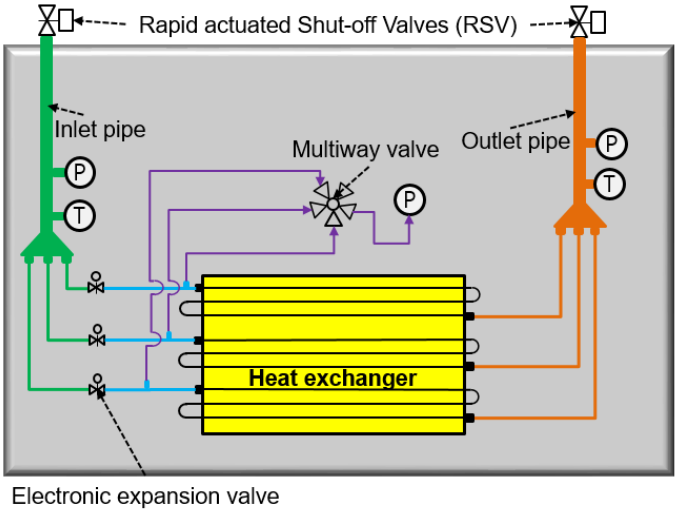

Figure 3.4: Simplified schematic diagram of the removable heat exchanger charge test module (RHXCT)

Detailed information of the RTPF are presented: itemized specifications in Table

3.3 and a schematic diagram of the circuits in Figure 3.5.

Table 3.3: The Round-Tube-Plate-Fin Heat Exchanger (RTPF) specifications

Number of tubes per bank	30
Number of bank	2
Number of circuits	3
Length of tubes	1.219 m
Outer diameter of tube	0.0095 m
Inner diameter of tube	0.0085 m
Tube spacing in air flow direction	0.0191 m
Tube spacing orthogonal to air flow direction	0.0254 m
Number of fins per inch	20
Amplitude of wavy fin	0.001 m
Half period of wavy fin	0.001 m
Fin thickness	0.0001 m
Fin type	Sine wave fins
Internal tube type	Smooth

The sampled charge inside the RHXCT is measured by the Differential Mass Measurement Scale (DMMS) exhibited in Figure 3.6. A high-accuracy load cell with a maximum capacity of 1,000 g and a 0.02% full scale accuracy is employed for the DMMS. As a result, the high-fidelity DMMS produces continual accurate charge measurements with a 3 g of error for the 49.9 kg tare weight of the RHXCT (Lee, Bach and Bradshaw, 2021).

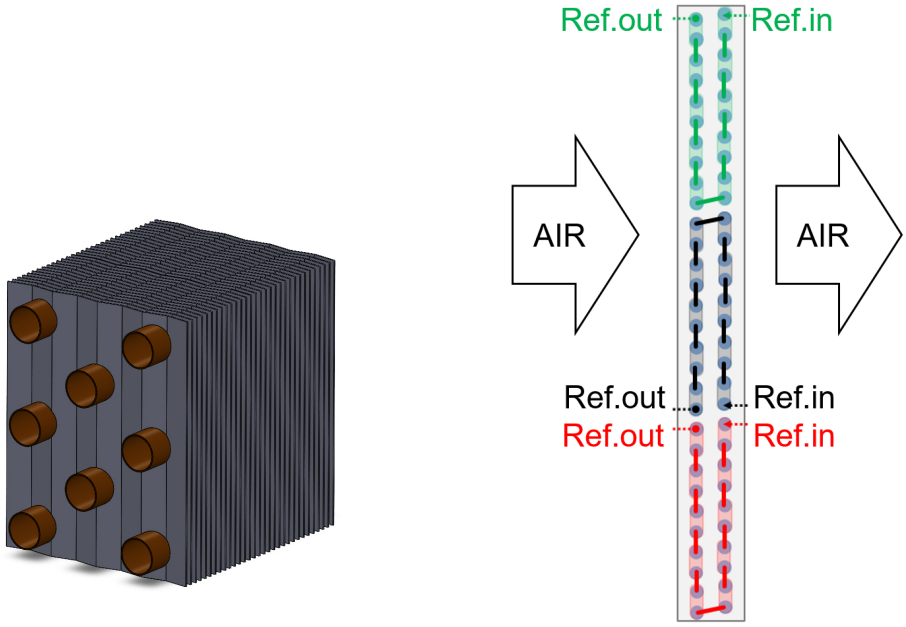

(a) Schematic diagram of the RTPF (b) Circuit information

Figure 3.5: Round-Tube-Plate-Fin Heat Exchanger (RTPF)

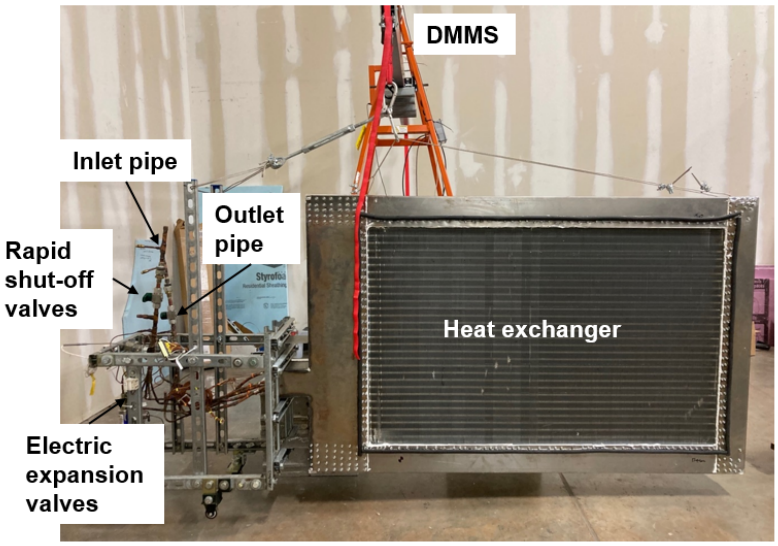

Figure 3.6: Differential Mass Measurement Scale (DMMS) with the Removable Heat Exchanger Charge Test module (RHXCT)

3.2.2 Testing Procedure

The overall operation steps of the differential mass evacuation sampling method (Lee et al., 2020) are illustrated in Figure 3.1; and the details are as follows:

1. Prior to weighing the RHXCT, the RHXCT is evacuated and weighed by the DMMS. This process gives an initial differential weight of the RHXCT, which is the Tare Weight (Δm_{TW}): the difference between a counter weight and weight of the RHXCT.

2. The Modular Duct Assembly (MDA) is prepared in a psychrometric chamber. The MDA can deliver desired flow rate, temperature, and humidity of air to the RHXCT. The RHXCT is connected to the MDA and operated at a steady state condition to allow refrigerant flow rates to stabilize. Once a desired test condition is reached and steady-state data acquisition is complete, the refrigerant charge in the RHXCT is sampled by simultaneously closing two Rapid Shut-off Valves (RSVs) on the RHXCT's inlet and outlet.

3. The RHXCT is disconnected from the MDA. Subsequently, the separated RHXCT

is weighed again using the DMMS, after any condensate on the surface has evaporated. The measured differential mass of the RHXCT in this step, is termed Charge-Sampled Weight (Δm_{CW}). The total charge in the RHXCT, enclosed between the two RSVs, is determined by the difference between the Δm_{CW} and Δm_{TW}. The charge in the RTPF of interest (*e.g.* heat exchanger tubes and return bends) is acquired by removing auxiliary charge inside RHXCT from the total charge in the RHXCT.

3.2.3 Experimental Test Matrix

An experimental test matrix is tabulated in Table 3.4. Two charge-sensitive parameters (Mei et al., 2005) are selected for developing an efficient test matrix: an outlet superheat, ΔT_{sh} and inlet liquid-line temperature of refrigerant, T_{liquid}. The experimental tests are carried out on the test matrix in evaporator mode under dry condition. The working fluids include two Low-GWP refrigerants, R1234yf and R468C, as well as R410A for reference. In air-side conditions, air inlet temperatures are maintained at 26.7 °C of dry-bulb and 15.0 °C of wet-bulb temperature. To evaluate precision of charge measurements, repeat tests are performed for both refrigerants as indicated in Table 3.4. The R410A test-condition range is given separately in Table E.4.

Table 3.4: Test matrix

Refrigerant	**Test ID**	ΔT_{sh} **(K)**	T_{liquid} **(°C)**	**Note**
R1234yf	yf-1	4.4	32.2	
	yf-2	4.4	43.3	
	yf-3	10	32.2	
	yf-4	10	43.3	
	yf-5	7.2	37.8	Repeat test
R468C	c-1	4.4	32.2	
	c-2	4.4	43.3	
	c-3	10	32.2	
	c-4	10	43.3	
	c-5	7.2	37.8	Repeat test
R410A	a-1	2.4 $\sim$ 7.4	32.2 $\sim$ 39.1	
	a-2			
	a-3			
	a-4			
	a-5			
	a-6			

3.2.4 Experimental Data Reduction

In this section, experimental data reduction is introduced. The charge of interest inside the RTPF, m_{RTPF} is calculated as

$$m_{RTPF} = m_{RHXCT} - m_{AUX} \tag{3.1}$$

where m_{RHXCT} is the measured charge inside the RHXCT, and m_{AUX} is the separately calculated charge, given in Equation E.3, inside the RHXCT excluding m_{RTPF}. As demonstrated in Figure 3.1, m_{RHXCT} is measured as follows:

$$m_{RHXCT} = \Delta m_{CW} - \Delta m_{TW} \tag{3.2}$$

where Δm_{CW} is the measured differential mass of charge-sampled RHXCT weight by the DMMS and Δm_{TW} is the measured differential mass of RHXCT tare weight by the DMMS. Those intermediate terms to obtain m_{RTPF} are detailed in Appendix E.

Primary heat exchanger testing variables are presented; the refrigerant-side capac-

ity, $\dot{Q}_{ref}$, air-side capacity $\dot{Q}_{air}$, and outlet superheat of evaporator, ΔT_{sh} are defined as

$$\dot{Q}_{ref} = \dot{m}_{ref} \cdot (h_{r,o} - h_{r,i}) \tag{3.3}$$

$$\dot{Q}_{air} = \dot{m}_{air} \cdot c_p \cdot (T_{db,i} - T_{db,o}) \tag{3.4}$$

$$\Delta T_{sh} = T_{r,o} - T_{r,sat,o} \tag{3.5}$$

where $\dot{m}_{ref}$ is the refrigerant flow rate, $h_{r,o}$ is the refrigerant enthalpy at the RTPF outlet, $h_{r,i}$ is the refrigerant enthalpy at the RTPF inlet, $\dot{m}_{air}$ is the air mass flow rate, c_p is the specific heat at constant pressure of air-water vapor mixture, $T_{db,i}$ is the inlet air dry-bulb temperature, $T_{db,o}$ is the outlet air dry-bulb temperature, $T_{r,o}$ is the refrigerant temperature at the RTPF outlet, $T_{r,sat,o}$ the saturated refrigerant temperature at the RTPF outlet. To avoid undesirable charge errors by water condensation, all tests were carried out under dry conditions without dehumidification, *i.e.* without condensation on the fins.

3.3 Experimental Results

3.3.1 Measured Charge

The experimental charge validation data was collected according to the test matrix given in Table 3.4. All tests were conducted under 5% limit of energy balance between refrigerant-side and air-side (ASHRAE, 2016). In addition, the collected data are high-fidelity charge measurements along with low uncertainty, $u_{m_{RTPF}}$, up to ±2.2% relative uncertainty of measured, $u_{m,rel_{RTPF}}$ as indicated Table 3.5.

Table 3.5: Refrigerant charge information in m_{RTPF} and the associated uncertainties

Test ID	m_{RTPF} (g)	$u_{m_{RTPF}}$ ±(g)	$u_{m,rel_{RTPF}}$ ±(%)	ΔT_{sh} (K)	T_{liquid} (°C)
yf-1	1072	4.3	0.4	3.4	31.5
yf-2	733	4.2	0.6	5.1	43.0
yf-3	484	5.7	1.2	10.1	31.5
yf-4	341	6.9	2.0	9.7	42.8
yf-5	372	6.6	1.8	7.3	37.5
c-1	605	4.5	0.7	4.2	32.4
c-2	480	5.1	1.1	4.8	42.7
c-3	338	4.1	1.2	10.0	32.3
c-4	353	4.1	1.2	8.9	42.0
c-5	419	4.5	1.1	7.6	37.8
a-1	441	6.6	1.5	2.4 ∼7.4	32.2 ∼39.1
a-2	299	6.6	2.2		
a-3	785	5.3	0.7		
a-4	432	4.6	1.1		
a-5	843	5.4	0.6		
a-6	619	4.3	0.7		

3.3.2 Repeatability

Additional repeat tests provide confidence on the collected charge measurements in terms of precision. Each repeat test was conducted on the same test point repeatedly as indicated in Table 3.4 and Figure 3.7. These repeat tests confirmed high-accuracy charge measurements consecutively, producing repeatability of 0.8% on R468C and

4.0% on R1234yf. It is noted that the repeat test includes entire measurement process such as acquiring steady condition - sampling - measurement process.

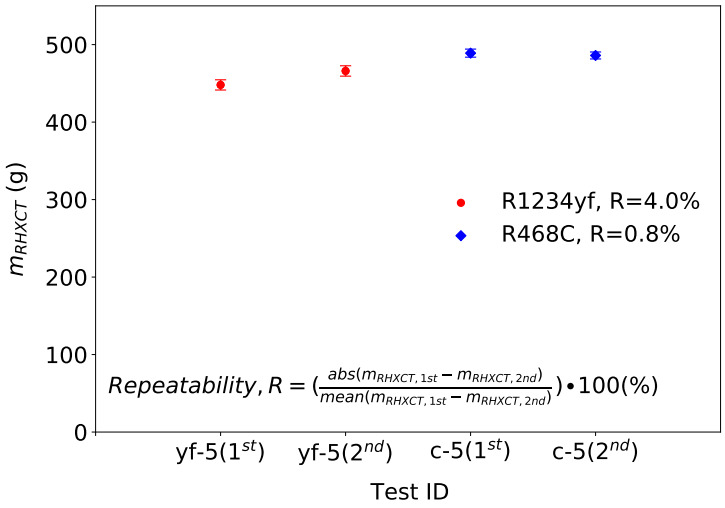

Figure 3.7: Repeatabilities of charge measurement in RHXCT, m_{RHXCT} on both test points, yf-5 and c-5.

3.3.3 Uncertainty Limit

Uncertainties of measurements are evaluated and enumerated in Table 3.6. The maximum uncertainties of charge inside the RTPF, $u_{m_{RTPF}}$ is ±6.9 g as displayed in Table 3.5. The detailed process to calculate $u_{m_{RTPF}}$ are separately described in Appendix E. In the Table 3.6, the uncertainties of calculated variables such as air-mass flowrate and capacities in both refrigerant and air sides are estimated according to the uncertainty propagation analysis (ASME-PTC-19.1, 2013; Saleem et al., 2020).

Table 3.6: Uncertainty limits of all the experimental tests

Parameter	**Symbol**	**Uncertainty**
Pressure	P	±3.8% of measured
Temperature	T	±0.33 °C
Refrigerant mass flow rate	$\dot{m}_r$	±0.05% of measured
Air mass flow rate	$\dot{m}_{air}$	±2.0% of measured
Refrigerant capacity	$\dot{Q}_r$	±1.2% of measured
Air capacity	$\dot{Q}_{air}$	±5.3% of measured

3.4 Charge Model

A detailed segment-by-segment heat exchanger model (Xfin) including a charge model was developed using void-fraction correlations (Sarfraz et al., 2019). The following sections explain descriptions and validations of the charge model.

3.4.1 Model Description

In the Xfin model, the mass of refrigerant in single phase is given as a product of density and volume. The density in single phase is retrieved from the property data; and the volume information used in the study is shown in Figure E.1. In two-phase, the separate masses of refrigerant in each vapor and liquid phase are calculated using the mean void fraction in a segment of interest, which is expressed in Equation 3.6 and 3.7:

$$m_v = \rho_v \cdot \alpha \cdot V \tag{3.6}$$

$$m_l = \rho_l \cdot (1 - \alpha) \cdot V \tag{3.7}$$

where m_g and m_f are the masses of refrigerant in vapor and liquid phase, respectively, ρ_g and ρ_f are the densities of refrigerant in vapor and liquid phase, respectively, α is the mean void fraction in a segment, V is the segment volume.

As can be seen in Equation 3.6 and 3.7, the void fraction is significant to determine charge inside the RTPF. Accordingly the void fraction is of interest to be corrected in this study to improve accuracy of the charge prediction.

Along with charge calculations, heat transfer and pressure drop in each segment are calculated. Also, phase change of refrigerant in a segment is captured by a moving boundary method (Sarfraz et al., 2018). Assumptions applied to the Xfin model are as follows:

1. Uniform distribution of air flow

2. Uniform distribution of refrigerant flow

3. Steady state flow

4. Uniform fluid property in each segment

5. Neglected tube to tube conduction through fins

Refrigerant properties are updated by employing REFPROP (Lemmon et al., 2018), while CoolProp (Bell et al., 2014) is used to calculate humid-air properties. When the property is retrieved, a lookup table of refrigerant is generated and then used for saving time of retrieving property (Sarfraz, 2020).

The heat transfers on the refrigerant, $\dot{Q}_{ref}$ and airside, $\dot{Q}_{air}$ are estimated by applying ε-NTU method in each segment on a lumped basis. They are defined as

$$\dot{Q}_{air}=\eta_f \cdot \varepsilon_{air} \cdot \ \dot{m}_{air} \cdot c_{p,air} \cdot (T_{air,i}-T_w)\,, \tag{3.8}$$

$$\dot{Q}_{ref}=\varepsilon_{ref} \cdot \ \dot{m}_{ref} \cdot c_{p,ref} \cdot (T_{ref,i}-T_w)\,, \tag{3.9}$$

where $\dot{m}$ is the mass flow rate, ε is the effectiveness, c_p is the heat capacity, and T_w is the segment wall temperature (Sarfraz, 2020). The correlations employed in the ε-NTU method are provided in Table 4.2.

Table 3.7: Correlations used in the Xfin model

Fluids	**Correlations**	**References**
Air	Heat transfer	Wavy fin correlations (Wang et al., 1997)
	Pressure drop	Wavy fin correlations (Wang et al., 1997)
Refrigerant	Heat transfer in single phase	Gnielinski (Gnielinski, 1976)
	Heat transfer in two-phase	Shah (Shah, 1982)
	Pressure drop in single phase	Blasius (Blasius, 1913)
	Pressure drop in two-phase	Lockhart-Martinelli (Lockhart and Martinelli, 1949)

3.5 Experimental Validation of the Xfin Model

Prior to tuning the Xfin model, it was experimentally validated against the obtained high-fidelity experimental validation data.

3.5.1 Evaluation of the Xfin Model

The prediction capability of the Xfin model in terms of $\dot{Q}$ and m_{RTPF} is evaluated against all the obtained experimental data given in Table 3.5 by a Mean Absolute Percentage Error (MAPE) expressed as

$$MAPE = \sum_{i=1}^{n} \left| \frac{Y_i - \hat{Y}_i}{Y_i} \right| \cdot \frac{100(\%)}{n} \tag{3.10}$$

where n is the number of data, i is an index of the data, Y denotes the measured data, $\dot{Q}$ or m_{RTPF}, and $\hat{Y}$ is the predicted data.

For charge prediction, a variety type of void-fraction models were employed; Zivi (Zivi, 1964), Lockhart-Martinelli(L-M) (Lockhart and Martinelli, 1949), Baroczy (Baroczy, 1963), Thom (Thom, 1964), and Taitel-Barnea (T-B) (Taitel and Barnea, 1990*b*) are recommended by previous charge studies in the literature with good agreement against experimental data (Harms, 2002; Ma et al., 2009; Abdelaziz et al., 2008). In addition, the Homogeneous model (Harms et al., 2003) was included for comparison. These void-fraction models are classified in sub-categories (Shen et al., 2006) as the mass-flux-dependent-mechanistic model (T-B), the slip-ratio-based model (Zivi, Thom, Homogeneous), and the Lockhart-Martinelli-parameter-based model (Baroczy, L-M). Those void-fraction models are defined as

$$Homogeneous: \ \alpha = \frac{1}{1 + \left(\frac{1-x}{x}\right)\left(\frac{\rho_v}{\rho_l}\right)} \tag{3.11}$$

$$Zivi: \ \alpha = C \cdot \frac{1}{1 + \left(\frac{1-x}{x}\right)\left(\frac{\rho_v}{\rho_l}\right)^{\frac{2}{3}}} \tag{3.12}$$

$$Thom: \ \alpha = \frac{1}{1 + \left(\frac{1-x}{x}\right)\left(\frac{\rho_v}{\rho_l}\right)^{0.89}\left(\frac{\mu_l}{\mu_v}\right)^{0.18}} \tag{3.13}$$

$$L-M: \ \alpha = \frac{1}{1 + 0.28\left(\frac{1-x}{x}\right)^{0.64}\left(\frac{\rho_v}{\rho_l}\right)^{0.36}\left(\frac{\mu_l}{\mu_v}\right)^{0.07}} \tag{3.14}$$

$$Baroczy: \ \alpha = C \cdot \frac{1}{1 + \left(\frac{1-x}{x}\right)^{0.74}\left(\frac{\rho_v}{\rho_l}\right)^{0.65}\left(\frac{\mu_l}{\mu_v}\right)^{0.13}} \tag{3.15}$$

$$T-B: \ \alpha = C \cdot \frac{1}{1.2 + 1.2\left(\frac{1-x}{x}\right)\left(\frac{\rho_v}{\rho_l}\right) + 0.35\left(\frac{\rho_v (gD_i)^{0.5}}{xG}\right)} \tag{3.16}$$

where C is the correction factor, x is the quality given as $\dot{m}_v/\dot{m}$, α is the void fraction, D_i is the inner diameter, g is the acceleration of the gravity, and G is the massflux.

Figure 3.8 shows the result of the predictions on both $\dot{Q}$ and m_{RTPF} without correction. The predicted capacities are well agreed with the measured data with 0.85% of MAPE; meanwhile, the predicted charges are fairly deviated from the measured charges.

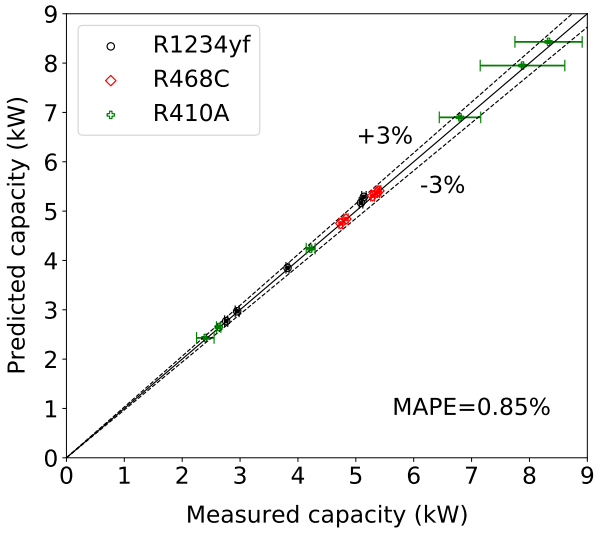

(a)

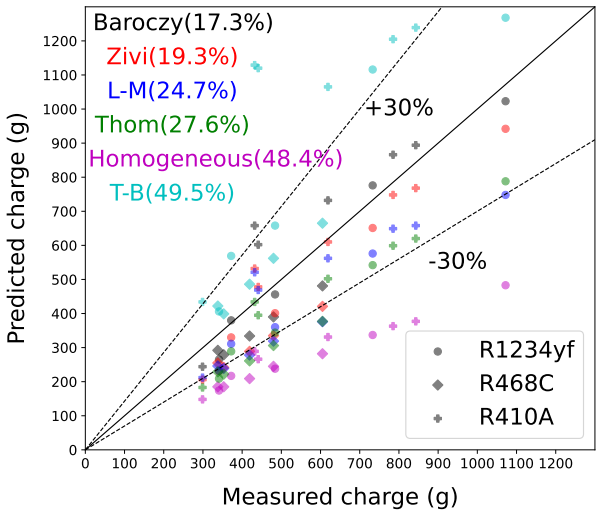

(b)

Figure 3.8: Comparison of prediction results with experimental data: (**a**) Cooling capacity, $\dot{Q}$ (**b**) Charge inside the RTPF, m_{RTPF}; the six void-fraction models are illustrated in different colors and the corresponding MAPEs are given in the parentheses.

Among the void-fraction models used, the Baroczy model provides the best capa-

bility of charge prediction with 17.3% of MAPE, followed by the Zivi, the L-M, the Thom, the Homogeneous, and the T-B void-fraction model.

Accordingly, the following section introduces a tuning method for charge prediction to improve the accuracy.

3.6 Tuning of the Charge Model

This section details the approach of tuning the charge model to improve accuracy of the charge model. Basically, the charge model is tuned by applying a correction factor to a void-fraction model. The correction factor is derived from the obtained experimental charge data through a constant correction factor method or a data-driven method by either a polynomial regression equation or Artificial Neural Network (ANN).

To generate the correction factor, initially charge predictions are carried out on each test point in the test matrix given in Table 3.4, while iteratively solving the charge model to have the charge model predict the same charge as the measured charge, m_{RTPF} corresponding to each test point as listed in Table 3.5. During this process, an original correction factor, $C_{original}$ for each test point is acquired; in other words, if the obtained original correction factor is multiplied to the void fraction, then the charge model that utilizes the void-fraction model can produce charge prediction without an error with respect to a corresponding measured charge. As a result, a $C_{original}$ is estimated according to each test point as summarized in Table 3.8 using the Zivi, the Baroczy, and the T-B model representing each mechanism of void fraction model.

Table 3.8: Estimated original correction factors, $C_{original}$

Test ID	Zivi	Baroczy	T-B
yf-1	0.963	0.986	1.062
yf-2	0.978	1.012	1.120
yf-3	0.959	0.986	1.097
yf-4	0.902	0.931	1.068
yf-5	0.974	1.005	1.141
c-1	0.895	0.927	1.040
c-2	0.905	0.939	1.064
c-3	0.928	0.959	1.085
c-4	0.895	0.927	1.052
c-5	0.903	0.935	1.058
a-1	1.010	1.044	1.215
a-2	0.930	0.957	1.124
a-3	0.991	1.021	1.118
a-4	1.025	1.058	1.202
a-5	0.982	1.013	1.106
a-6	0.998	1.032	1.139

3.6.1 Constant Correction Factor

A constant correction factor, C_{const} is suggested as the most simple correction method in this study by simply averaging the $C_{original}$ to acquire C_{const}. The Zivi model is taken into account to evaluate the capability of this constant-correction-factor method. Therefore 0.952 is selected as the C_{const} by averaging $C_{original}$ of the Zivi model as listed in Table 3.8; in other words, C inside Equation 3.12 is replaced with 0.952 of C_{const} for tuning the charge model.

Charge predictions are conducted using the constant-correction-factor method on the whole test points and they are compared with the experimental charge data. Figure 3.9 shows the result of the constant-correction-factor method; the un-corrected model struggles to predict charge in some low-charge points with over 20% errors.

Through the constant-correction-factor method, the errors are improved; however some outliers are generated and there is no significant improvement found in terms of the MAPE, an improvement of 0.1% point of MAPE compared to the result of the un-corrected model.

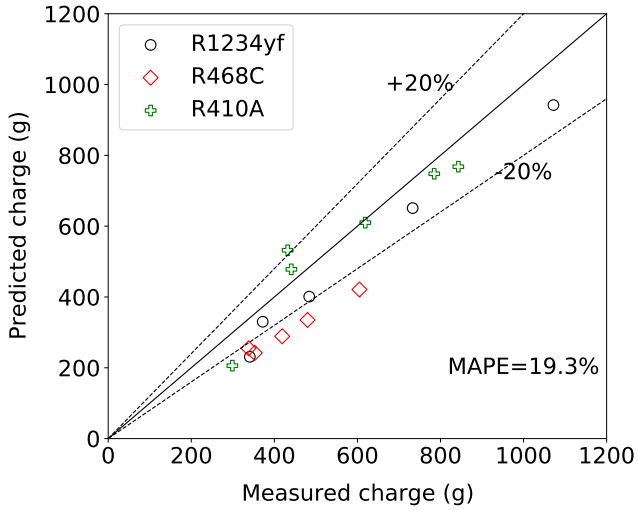

(a) Un-corrected model

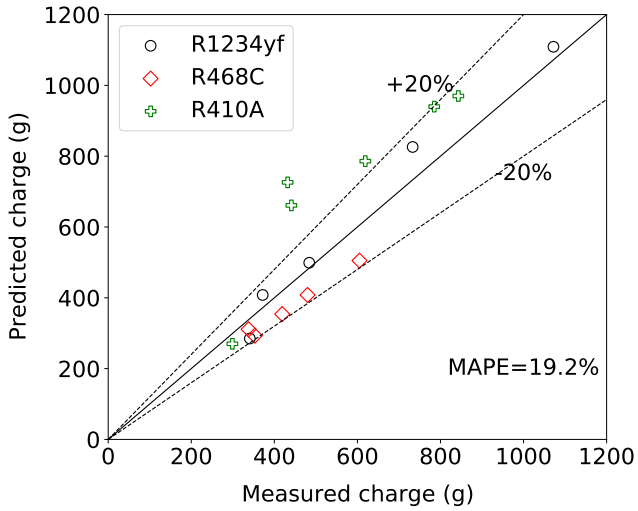

(b) Corrected model

Figure 3.9: Effect of the correction method by C_{const} on the Zivi model. The uncertainties are separately given in Table 3.5.

Therefore this method might not be sufficient to improve accuracy of the charge model, thus leading to a development of data-driven-correction method introduced in the following section for further improvement of the charge model.

3.6.2 Regression Equation Correction Factor

As stated previously, improvement of charge-prediction accuracy by the C_{const} is limited to address diverse conditions, given it is a fixed value. This results in a development of an adjusted correction factor that is estimated by one of our experimental data-driven method, a polynomial regression equation.

A polynomial regression equation is proposed for producing a correction factor to improve an adaptability of the correction factor in various simulation conditions such as various evaporating temperatures and outlet superheats. Specifically, the correction factor to be implemented in Equation 3.12, 3.15, and 3.16 is estimated as an output of the polynomial regression equation.

In the similar way as the C_{const} is calculated, the correction factor from the polynomial regression equation, $C_{regress}$ also requires the $C_{original}$ — presented in Table 3.8 — as the response variable to be modeled in the regression equation.

The next step is to choose crucial input parameter for the polynomial regression equation. The previous literature review on void-fraction models suggests a couple of charge-sensitive dimensionless numbers found in widely used void-fraction models in a vapor-compression cycle (Harms et al., 2003; Cioncolini and Thome, 2012; Jin and Hrnjak, 2016), which includes a saturated vapor to liquid density ratio, ρ_v/ρ_l, a saturated vapor to liquid viscosity ratio, μ_v/μ_l as well as liquid Reynolds number, Re_l and liquid Weber number, We_l expressed as

$$Re_l = \frac{GD_i}{\mu_l} \tag{3.17}$$

$$We_l = \frac{G^2 D_i}{\sigma \rho_l} \tag{3.18}$$

where G is the massflux, D_i is the inner diameter, μ_l, ρ_l, and σ are the dynamic viscosity, density, and surface tension of the liquid refrigerant, respectively, defined at the suction pressure.

Accordingly, these dimensionless numbers are taken into account as the candidate input parameters of the polynomial regression equation. Those values are tabulated in Table 3.9 along with the $C_{original}$ according to the corresponding experiment test point.

Table 3.9: Candidate input parameters and the response variable ($C_{original}$), developed on each void-fraction models used, for the polynomial regression equation according to each test point

Test ID	$C_{original,Zivi}$	$C_{original,Baroczy}$	$C_{original,T-B}$	ρ_v/ρ_l	μ_v/μ_l	Re_l	We_l
yf-1	0.963	0.986	1.062	0.0269	0.0657	11300	52.7
yf-2	0.978	1.012	1.120	0.0287	0.0679	9588	37.8
yf-3	0.959	0.986	1.097	0.0237	0.0618	10390	45.0
yf-4	0.902	0.931	1.068	0.0243	0.0625	6436	17.2
yf-5	0.974	1.005	1.141	0.0268	0.0656	6724	18.7
c-1	0.895	0.927	1.040	0.0408	0.0889	11152	29.6
c-2	0.905	0.939	1.064	0.0402	0.0883	10839	28.0
c-3	0.928	0.959	1.085	0.0308	0.0778	9808	23.4
c-4	0.895	0.927	1.052	0.0332	0.0806	10055	24.4
c-5	0.903	0.935	1.058	0.0346	0.0822	10748	27.8
a-1	1.010	1.044	1.215	0.0289	0.0791	5188	7.8
a-2	0.930	0.957	1.124	0.0237	0.0725	4272	5.4
a-3	0.991	1.021	1.118	0.0242	0.0731	11823	41.4
a-4	1.025	1.058	1.202	0.0243	0.0732	7528	16.8
a-5	0.982	1.013	1.106	0.0265	0.0761	15618	71.6
a-6	0.998	1.032	1.139	0.0252	0.0744	14163	59.2

Subsequently the input parameters of the polynomial regression equation are selected among the candidates by evaluating correlation strength with $C_{original}$ for each void-fraction model. For this purpose, a sensitivity analysis for each $C_{original}$ is conducted with the Pearson correlation coefficient, r known for choosing significant parameters among variables by evaluations of linear correlation strength between variables (Meng-ting et al., 2019; Kim et al., 2020). The r is defined as

$$r = \frac{\sum_{i=1}^{n}(X_i - \overline{X})(Y_i - \overline{Y})}{\sqrt{\sum_{i=1}^{n}(X_i - \overline{X})^2}\sqrt{\sum_{i=1}^{n}(Y_i - \overline{Y})^2}} \tag{3.19}$$

where X and Y are variables, n is the number of data, i is an index of the data, and

$\overline{X}$ and $\overline{Y}$ indicate the mean value of X and Y, respectively. The r varies between -1 and 1, indicating negative and positive perfect linear correlation, respectively. When r is 0, it represents no correlation between the two variables.

On the basis of Table 3.9, a r of each candidate input parameter for each $C_{original}$ is calculated according to Equation 3.19 as summarized in Table 3.10. The result of the sensitivity analysis presents a strong correlation strength of the ρ_v/ρ_l for both Zivi and Baroczy model, followed by μ_v/μ_l. Accordingly, the ρ_v/ρ_l and μ_v/μ_l are selected as the input parameters for both Zivi and Baroczy model. Similarly, the ρ_v/ρ_l and Re_L are chosen as the input parameter of the polynomial regression equation for the correction factor of the T-B void-fraction model.

Table 3.10: Absolute Pearson correlation coefficients (r)

	ρ_g/ρ_f	μ_g/μ_f	Re_L	We_L
$C_{original,Zivi}$	0.623	0.367	0.035	0.242
$C_{original,Baroczy}$	0.588	0.324	0.041	0.230
$C_{original,T-B}$	0.532	0.223	0.381	0.233

With the selected input parameters and the response value, $C_{original}$, a polynomial regression equation is built to generate a correction factor for each corresponding void-fraction model. The general formulation of the polynomial regression equation is originated from a multiple-linear regression format with an addition of one interaction for the input parameters, which is expressed as

$$Y = \beta_1 X_1 + \beta_2 X_2 + \beta_3 X_1 X_2 \tag{3.20}$$

where Y denotes the $C_{regress}$, X represents the input parameters, β represents an estimated coefficient.

The Ordinary Least Squares (OLS) solver built in Minitab program (Minitab, 2021) applies to the Equation 3.20 in order to obtain the coefficients; specifically, an estimated equation is calculated by determining the equation that minimizes the

sum of the squared errors between the data points and the values estimated by the equation, thus resulting in the βs. This process is carried out under the k-fold cross-validation method with 8-folds data set to decrease overfits.

The fitted polynomial regression equations for the Zivi, the Baroczy, and the T-B model are given as, respectively,

$$C_{regress,Zivi} = 29.28(\rho_v/\rho_l) + 14.43(\mu_v/\mu_l) - 442.30(\rho_v/\rho_l)(\mu_v/\mu_l) \tag{3.21}$$

$$C_{regress,Baroczy} = 29.76(\rho_v/\rho_l) + 14.85(\mu_v/\mu_l) - 449.0(\rho_v/\rho_l)(\mu_v/\mu_l) \tag{3.22}$$

$$C_{regress,T-B} = 45.07(\rho_v/\rho_l) + 0.000115(Re_l) - 0.00463(\rho_v/\rho_l)(Re_l) \tag{3.23}$$

The polynomial regression equations produce $C_{regress}$ for each corresponding void-fraction model as tabulated in Table 3.11.

Table 3.11: Calculated $C_{regress}$ for each test point according to each void-fraction model used

Test ID	$C_{regress,Zivi}$	$C_{regress,Baroczy}$	$C_{regress,T-B}$
yf-1	0.954	0.983	1.105
yf-2	0.958	0.988	1.122
yf-3	0.938	0.965	1.123
yf-4	0.942	0.970	1.111
yf-5	0.954	0.982	1.146
c-1	0.874	0.906	1.015
c-2	0.881	0.914	1.041
c-3	0.965	0.996	1.117
c-4	0.951	0.983	1.107
c-5	0.941	0.974	1.074
a-1	0.977	1.009	1.204
a-2	0.980	1.010	1.091
a-3	0.981	1.012	1.125
a-4	0.981	1.012	1.114
a-5	0.982	1.013	1.074
a-6	0.982	1.013	1.113

Thereafter, the Zivi, Baroczy, and T-B model are corrected by replacing the C inside Equation 3.12, 3.15, and 3.16 with the corresponding $C_{regress}$. The effect of the correction by $C_{regress}$ is evaluated by comparing the measured charge and the charge prediction of the tuned charge model for all the test points.

Figure 3.10, 3.11, and 3.12 present the results of the tuned Zivi, Baroczy, and T-B void-fraction model, respectively.

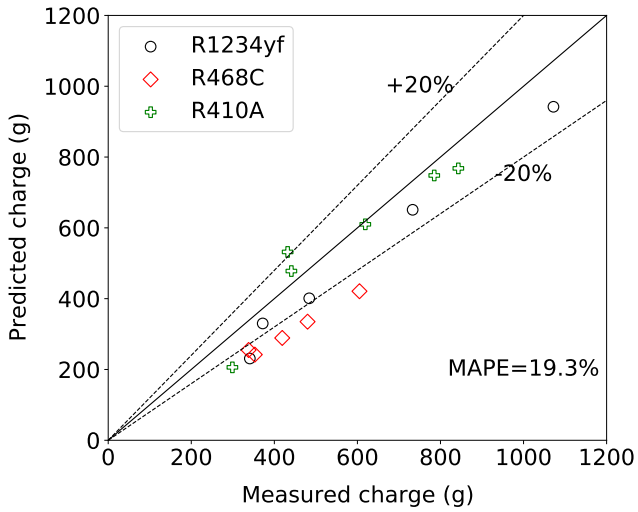

(a) Un-corrected model

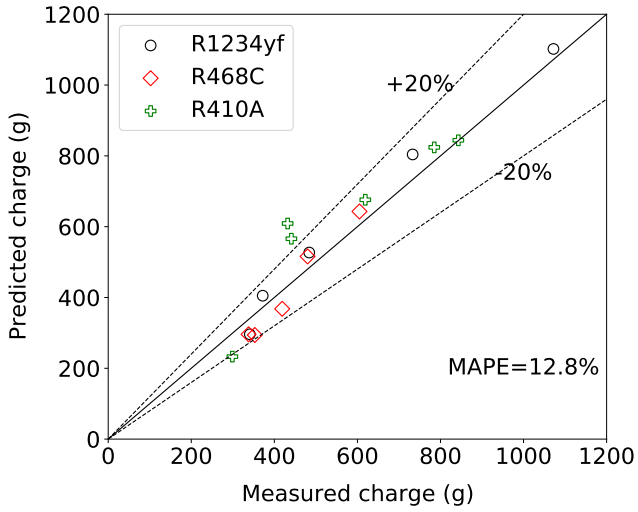

(b) Corrected model

Figure 3.10: Effect of the correction method by $C_{regress}$ on the Zivi model. The uncertainties are separately given in Table 3.5

Each void-fraction model is significantly improved by the $C_{regress}$ as indicated in Table3.12. In terms of the MAPE, the errors are reduced regardless of the type of the void-fraction model: from 19.3% to 12.8% for the Zivi, from 17.3% to 12.9% for the Baroczy, and from 49.5% to 12.3% for the T-B void-fraction model.

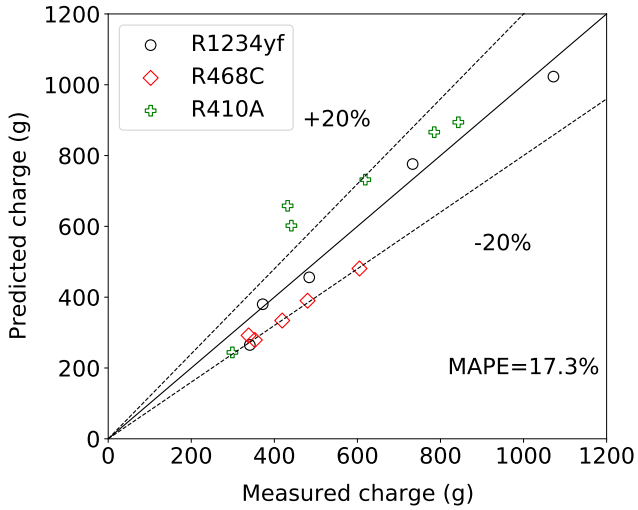

(a) Un-corrected model

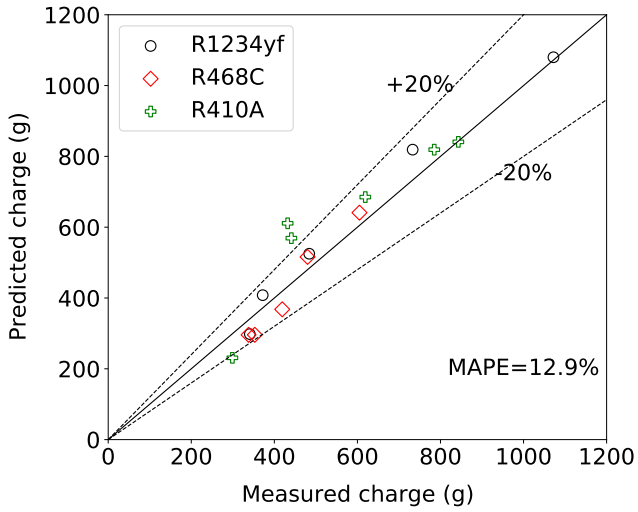

(b) Corrected model

Figure 3.11: Effect of the correction method by $C_{regress}$ on the Baroczy model. The uncertainties are separately given in Table 3.5.

Likewise, for all the void-fraction models used, the charge-prediction errors are

also diminished with respect to the Root Mean Square Errors (RMSE) defined as

$$RMSE = \sqrt{\sum_{i=1}^{n} \frac{(\hat{Y}_i - Y_i)^2}{n}} \tag{3.24}$$

where Y_i is an experimental validation data, $\hat{Y}_i$ is a predicted value and n is the number of test points used in the evaluation.

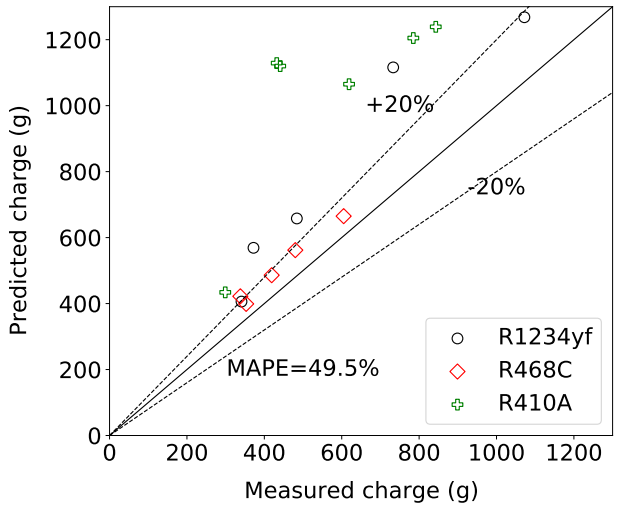

(a) Un-corrected model

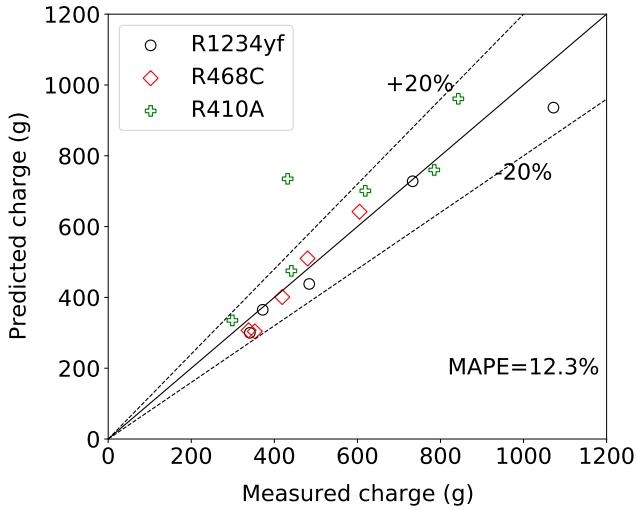

(b) Corrected model

Figure 3.12: Effect of the correction method by $C_{regress}$ on the T-B model. The uncertainties are separately given in Table 3.5.

Besides, the tuned charge models agree fairly well with the measured data in terms

of the goodness of fit, showing improvement of the Coefficient of Determination, r^2 for all the void-fraction models used as demonstrated in Table3.12.

Table 3.12: Improvement of accuracy by $C_{regress}$

	Un-corrected model			**Corrected model**		
	Zivi	**Baroczy**	**T-B**	**Zivi**	**Baroczy**	**T-B**
MAPE (%)	19.3	17.3	49.5	12.8	12.9	12.3
RMSE (g)	100.8	97.2	333.5	69.7	71.2	94.8
r^2	0.90	0.85	0.63	0.93	0.92	0.82

The T-B void-fraction model improved the most in accuracy of all the void-fraction models used. For further improvement of the T-B model, another data-driven method, the ANN, is applied to develop the correction factor, described in the next section.

3.6.3 ANN Correction Factor

The other type of the data-driven tuning method is to use the ANN, thus estimating the correction factor in the similar manner as the regression equation does. The ρ_v/ρ_l and Re_L as well as the $C_{original,T-B}$ are selected as the input parameters and the output variable of the ANN model for tuning the T-B model, respectively, following the same selection process given in the previous section. A feed-forward back-propagation neural network (Mousavi et al., 2013) is used for developing the correction factor for the T-B void-fraction model, $C_{ANN,T-B}$.

Prior to setting up the ANN model, the data set including ρ_v/ρ_l, Re_L, and $C_{original,T-B}$ given in Table 3.9 is normalized for improving the speed and convergence of the ANN as suggested by (Ma et al., 2020). The normalized each input parameter is fed into each neuron in the input layer, whereas the neuron in the output layer produces the normalized correction factor, $C_{ANN,T-B}$ to be estimated. While training the ANN model on the whole experimental test points, the weights and biases of the ANN model are updated by the Adam optimization algorithm (Kingma and Ba, 2014).

The hyperparameters of the ANN model are obtained by the K-fold cross-validation method (Pedregosa et al., 2011) to reduce overfitting given the size of data. The selected hyperparameters and architecture of the ANN model are presented in Table E.5 and E.6. Once the $C_{ANN,T-B}$ is obtained, the T-B model is tuned by replacing the C inside Equation 3.16 with the $C_{ANN,T-B}$.

For evaluation of the tuned T-B model, the measured charges are compared with the predictions of the tuned T-B model. Figure 3.13 displays the comparison result.

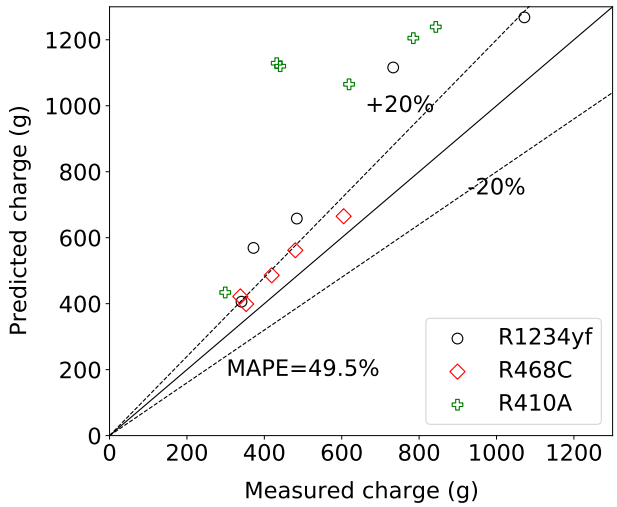

(a) Un-corrected model

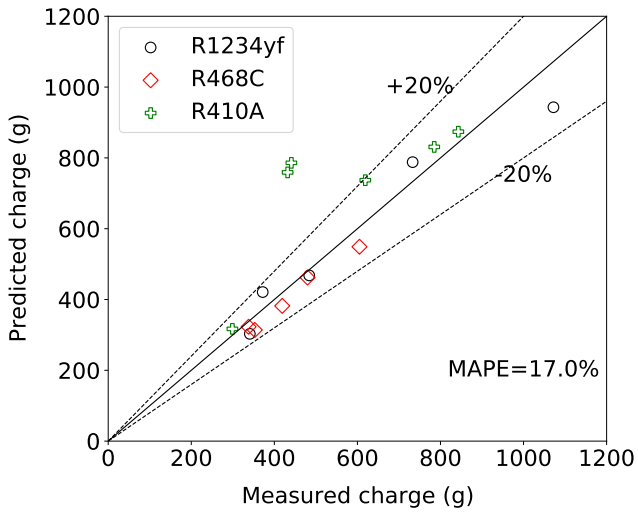

(b) Corrected model

Figure 3.13: Effect of the correction method by C_{ANN} on the T-B void-fraction model. The uncertainties are separately given in Table 3.5.

The C_{ANN} also proves the capability of improvement in the charge-prediction accuracy. In most cases, the tuned charge model predicts reasonably well within 20% of error compared to the measured charge. However, there are more outliers than the $C_{regress}$, and as a result, it shows lower prediction capability than the $C_{regress}$ in all of the accuracy indicators as presented in Table 3.13.

Table 3.13: Effect of C_{ANN} and $C_{regress}$ on the T-B void-fraction model

	Un-corrected	**Corrected by $\mathbf{C_{regress}}$**	**Corrected by $\mathbf{C_{ANN}}$**
MAPE (%)	49.5	12.3	17.0
RMSE (g)	333.5	94.8	130.7
r^2	0.63	0.82	0.70

3.7 Conclusions

This study presents high-fidelity and high-precision experimental charge data of the RTPF along with 0.8% of charge-measurement repeatability and ±2.2% of relative-charge measurement uncertainty of measured. Particularly the charge data includes two Low-GWP refrigerants of interest, R1234yf and R468C, in addition to R410A refrigerant for reference.

This high-quality database for experimental charge validation contributes to evaluate and tune the charge model.

The accuracy of the charge model was evaluated with a total of six different void-fraction models. The Baroczy model shows the best agreement with the measured charge data with 17.3% of the MAPE, followed by Zivi, L-M, Thom, Homogeneous, and T-B void-fraction model. In fact, none of the void-fraction models are sufficiently accurate for the charge estimation. It is found that all of the void-fraction models need a correction for accurate charge prediction.

To improve the accuarcy of the charge prediction, an accurate tuned charge model is developed. This tuning process is done by applying a correction factor to each selected void-fraction model. Unlike the constant correction factor, the adjusted cor-

rection factor generated by the data-driven method including the regression equation and the ANN proves notable improvement of the charge prediction accuracy with respect to all the used criteria in MAPE, RMSE, and r^2.

In terms of the MAPE, the tuned T-B model by the $C_{regress}$ shows the best agreement with the experimental validation data with 12.3% of MAPE, followed by the Zivi with 12.8% of MAPE and the Baroczy with 12.9% of MAPE.

In conclusion, the developed tuned charge model is validated with the high-fidelity experimental charge data using Low-GWP refrigerants and confirms the improved charge-prediction accuracy. This allows an effective design of heat exchangers and heat pumps with confident prediction of charge.

Future work will include taking into account flow patterns of refrigerant flow in two-phase and geometrical effects as well as other promising Low-GWP refrigerants for further improvement of charge prediction.

CHAPTER IV

DEVELOPMENT OF MULTI-OBJECTIVE OPTIMIZATION FRAMEWORK FOR REDUCING REFRIGERANT CHARGE AND INCREASING COOLING CAPACITY OF A HEAT PUMP

Abstract

A validated optimization framework is developed to satisfy multiple objectives simultaneously with multi-input variables and provide optimal solutions. The developed framework addresses two objectives, minimizing refrigerant charge and maximizing cooling capacity of a heat pump, and two input variables of the heat pump, subcooling in a condenser and superheat in an evaporator playing a decisive role in performance and charge of a heat pump. Reducing the refrigerant charge, not to mention maximizing cooling capacity, is an issue that must be addressed in terms of environment, safety, and economy when designing heat pumps.

The best solution is selected based on the Coefficient of Performance (COP) after selecting a set of optimal solutions by the Non-Dominated Sorting Genetic Algorithm (NSGA-II). The cooling capacity and the refrigerant charge are predicted by the Air Conditioning Heat Pump (ACHP) model. Through the Radial Basis Function (RBF) surrogate model, the cooling capacity and charge become possible to be estimated in a given design space, which allows the NSGA-II to choose the optimal solutions by numerous evaluations. The selected best solution attained 10.9% and 21.6% of $\dot{Q}_{eva}$ and COP improvement, respectively, while minimizing 7.4% of $m_{r,sys}$.

This chapter will be submitted for publication in the International Journal of

Refrigeration.

4.1 Introduction

A number of studies have been carried out to optimize charge in a heat pump; yet most studies placed weight on improvement of system performance through charge optimization rather than reduction of charge. Often optimal charge refers to the charge to maximize system performance (Poggi et al., 2008). Charge-optimization studies have focused on determination optimal charge with respect to maximizing system performance (Kim and Braun, 2012; Yin et al., 2021; Li et al., 2020; Prabakaran and Mohan Lal, 2018; Hu et al., 2018; Lee, Lee, Cho and Kim, 2021; He et al., 2020).

In the past, a few studies investigated charge reduction without compromising system performance. Goswami et al. (2001) experimentally studied and reported 10% of charge reduction allowing 2% increase in COP . Lately, several studies emphasized charge reduction and performance improvement with the advent of low-GWP refrigerants. Saravanan et al. (2017) used capillary tubes and condenser tubes for charge reduction while maximizing performance. Cho et al. (2020) reduced refrigerant charge of R600 in a domestic refrigerator-freezer by optimizing condenser geometry, minimizing energy consumption and charge. Hermes (2015) accomplished charge reduction in vapor compression refrigeration cycles via liquid-to-suction heat exchange. Ghoubali et al. (2017) experimentally studied charge reduction and capacity improvements in propane heat pump water heaters by evaluating three different types of condensers including a tank-wrapped D-tube, a roll-bond, and a microchannel heat exchanger. Jiang (2015) presented charge reduction in small commercial refrigeration systems by using a flattened-finless-round-tube heat exchanger without compromising system performance.

Although these studies dealt with both charge reduction and performance improvement, they focused on device modifications.

There are few studies on simultaneous optimization of both charge and capacity of a heat pump by optimizing the vapor-compression cycle in the open literature. A step toward investigation between input (design) variables and objective functions such as cooling capacity and charge would improve system performance and charge reduction.

Two input variables, ΔT_{sc} and ΔT_{sh}, are suggested for this optimization study to design the vapor compression system since they are critical to both $\dot{Q}_{eva}$ and $m_{r,sys}$. For instance, ΔT_{sc} and ΔT_{sh} are both charge indicators (Mei et al., 2005), $\dot{Q}_{eva}$ is significantly affected by controlling of ΔT_{sh} (Rasmussen and Larsen, 2009), and ΔT_{sc} is one of the prime factors to affect $\dot{Q}_{eva}$ (Cho et al., 2020).

In a heat pump, the improvement of cooling capacity and charge reduction are conflicting each other; in other words, they are trade-off. For instance, high ΔT_{sh} and low ΔT_{sc} result in charge reduction in a heat pump (Hu et al., 2018), whereas $\dot{Q}_{eva}$ tends to decrease in the combination of high ΔT_{sh} and low ΔT_{sc} (Liu and Cai, 2021; Qureshi et al., 2013).

Hence, it is challenging to find a single solution for satisfying the multiple targets, objective functions that include $\dot{Q}_{eva}$ and $m_{r,sys}$ in the trade-off problem (Juan and Qin, 2014; do Nascimento et al., 2020). To deal with this trade-off, a multi-objective optimization is proposed. The multi-objective optimization is generally used in engineering, economics, computer science, logistics, and many other fields to solve trade-off problems.

In recent studies related to both a multi-objective optimization and a heat pump, Li et al. (2021) employed the multi-objective optimization to maximize an energy-efficiency ratio and minimize flammability of low-GWP refrigerant in a system, modifying a refrigerant mixture composition and heat exchanger circuitry configuration. They reported an enhancement of 5.9% in cycle efficiency and a 48.6% reduction in refrigerant flammability with a GWP of 268.

Bahman et al. (2022) took advantages of concurrent-optimization capability of multi-objective optimization framework, assisted by the Non-dominated Sorting Genetic Algorithm-II (NSGA-II), to propose optimal solutions for solving a trade-off between a heating coefficient of performance and unit cost of heat in a cold-climate two-stage economized heat pump for residential heating applications. In the multi-objective problem, the ΔT_{sc} and the ΔT_{sh} were included as input variables for a heat pump. Bahman et al. (2022) presented that the optimization framework lead to an improvement of heating performance and energy consumption of a heat pump using R290 refrigerant.

In short, to the authors' best knowledge, there are few investigations to explain a method optimizing cooling capacity and refrigerant charge concurrently in a heat pump by modifying the vapor-compression cycle; for this reason, this study fills the gap by introducing a novel multi-objective optimization framework.

To start with, the history of the evolving multi-objective optimization methods are summarized in Cui et al. (2017). According to Cui et al. (2017), in the past, multi-objective optimization problems were solved by converting a multi-objective problem into single objective problems and utilizing conventional optimization algorithms along with pre-defined importance degree of each objective to deal with a trade-off between objectives, which is known as an *a priori* method. In the last 30 years, intelligent algorithms have been dominating the multi-objective optimization methods due to the fact that they are flexible, robust, and well-converged compared to the classical a priori method. The intelligent algorithms include swarm-based and evolution-based algorithms. The swarm-based algorithms mimic collective behavior of populations, *e.g.* bird flocks and honey bees, that the swarm individual collaborates each other to find optimal solutions.

The evolution-based algorithms represented by popular Genetic Algorithms (GA) are stochastic search method inspired from survival in natural ecosystems. The GA for

multi-objective optimization was introduced by Goldberg David and Henry (1988). In other words, it is a nature-inspired optimization algorithm to imitate natural selection and evolutionary processes for selecting optimal solutions (Juan and Qin, 2014).

The GA generates a population of candidate solutions that advances from generation to generation. Superior candidate solutions are stochastically chosen from the population in terms of fitness to objective functions for each generation. Subsequently, the chosen candidate solutions produce a new generation of the candidate solutions by mutation and crossover. This evolving process is repeated till either reaching maximum resources or achieving target fitness (Shojaeefard et al., 2017).

The Non-dominated Sorting Genetic Algorithm-II (NSGA-II) is an advanced version of the GA to search global optimal solutions with high fidelity, in addition to the basic GA capability, by fast non-dominated sorting and crowded sorting (Deb et al., 2002). The fast non-dominated sorting method yields an individual candidate solution that is not dominated by any other candidates in terms of an objective function; besides, the crowded sorting method determines crowding distance of each candidate solution by estimating distances between neighboring solutions in an objective space, thus leading to a good spreading of solutions. This whole process makes certain that superior capability of global search to find optimal solutions in a multi-objective optimization (Deng et al., 2020; Blank and Deb, 2020).

Common optimization algorithms include the NSGA-II, the Particle Swarm and the Grey Wolf (Mirjalili et al., 2014). Among them, the NSGA-II is distinguished as an attractive optimization tool owing to its performance recognized by plentiful studies over wide range of area (Safikhani, 2016; Damavandi et al., 2017; Shojaeefard and Zare, 2018; Deng et al., 2020; Dong et al., 2021).

The intelligent algorithms require numerous evaluations of objective functions in a design space to ensure their high fidelity and random search capability (Dong et al., 2021).

To address this need, a surrogate model method along with effective data sampling has become a widely used workhorse for the optimization algorithms owing to their capability of approximation or interpolation of the objective functions, thus leading to computationally effective evaluations of objective functions (Kyprioti et al., 2020; Jiang et al., 2018; Zhou et al., 2017).

The surrogate model is a method to produce approximation of an objective function. In the surrogate model, observed design variables and a corresponding objective function are formulated with a mathematical expression, thus yielding rapid evaluations of the approximated objective function (Dong et al., 2021); to put it another way, the surrogate model is a method of building a computationally efficient mathematical model through approximation of data (Tyan and Lee, 2019). Popular surrogate models, also known as metamodels, include support vector regression (Xiao et al., 2015), Kriging model (Kyprioti et al., 2020), polynomial response surface model (Eddy et al., 2015), and Radial Basis Function (RBF) model (Qasem et al., 2012; Zhou et al., 2017; Cai et al., 2017).

Advantages of multi-objective optimization accompanied with a surrogate model have been recognized in a great deal of studies: Deng et al. (2020) argued computational efficiency in use of surrogate model since it enables NSGA-II to compute evaluations within milliseconds rather than days of a CFD simulation. Damavandi et al. (2017) claimed that a surrogate model coupled with NSGA-II makes fast calculation and consumes fewer computation resources. Peng and Ling (2008) asserted that direct evaluations by simulation is time consuming and low-efficient, whereas a surrogate model can effectively solve it.

Aute et al. (2013) maintained that a surrogate model can reduce computational effort for multi-objective genetic algorithm on trade-off between airside-pressure drop and volume of a novel air-to-water heat exchanger. Often the intelligent algorithms demand thousands evaluations of objective functions; however in some application area,

those evaluations take enormous computation time. The surrogate model method allows efficient evaluations of objective functions with less data calling/calculations (Tyan and Lee, 2019; Dong et al., 2021).

Among the various surrogate models, the RBF surrogate model has been utilized in diverse research fields due to its efficiency and accuracy (Jin et al., 2001; Holmström, 2008; Cai et al., 2017): for instance, compressor blades (Liu et al., 2016), pressure vessels and airfoils (Zhou et al., 2017), as well as propellers (Cai et al., 2017). The RBF surrogate model comprises linear combinations of a radially symmetric function to approximate an objective function (Jin et al., 2001).

Owing to its symmetry and linearity, the RBF surrogate model has advantages such as simplicity and ease of implementation in multivariate data (Hardy, 1971), capability to accommodate on higher dimensions with scarce data (Rocha, 2009), and good fitting performance and robust for non-linear problems. These advantages of the RBF surrogate model lead to an adoption to this optimization study to approximate both cooling capacity and refrigerant charge.

In summary, the literature review results in this development of the multi-objective optimization framework to attain both maximizing cooling capacity and minimizing charge in a heat pump, supported by the NSGA-II and the surrogate model as well as a vapor-compression system model—the Air Conditioning Heat Pump (ACHP) model (Bell, 2015; Bahman et al., 2018).

This paper is organized as follows. Section 4.2 introduces an overall methodology including the ACHP model and the surrogate model as well as the NSGA-II. Subsequently Section 4.3 presents the outcomes of the optimization such as the developed surrogate model and the optimal solutions as well as the selected best solution. Finally, this study is concluded with final remarks in Section 4.4.

4.2 Methodology

4.2.1 Overall Method

The trade-off between cooling capacity, $\dot{Q}_{eva}$ and refrigerant charge in a heat pump, $m_{r,sys}$ is converted into a multi-objective optimization problem that is solved by the NSGA-II. $\dot{Q}_{eva}$ and $m_{r,sys}$ are treated as objective functions to be maximized and minimized, respectively as given in Equation 4.1. The input variables include subcooling in a condenser, ΔT_{sc} and superheat in an evaporator, ΔT_{sh}. Figure 4.1 presents the overall method used for the multi-objective optimization.

A validated ACHP model will provide both cooling capacity and charge predictions. The objective functions are mapped on the design space, covered by the ΔT_{sc} and ΔT_{sh}, for enabling many evaluations of objective functions instantly, which is done by the proposed surrogate model method. Based on the generated surrogate models, the NSGA-II genetically produces a set of optimal solutions, and the best solution is selected among them by comparing COPs with each other.

The multi-objective optimization to be carried out is expressed mathematically in the following form:

$$\begin{aligned} &Objective-1: Maximize,\ \dot{Q}_{eva} = f_1\left(\Delta T_{sc}, \Delta T_{sh}\right) \\ &Objective-2: Minimize,\ m_{r,sys} = f_2\left(\Delta T_{sc}, \Delta T_{sh}\right) \\ &Subject\ to: \Delta T_{sc,min} \leq \Delta T_{sc} \leq \Delta T_{sc,max} \ \cap\ \Delta T_{sh,min} \leq \Delta T_{sh} \leq \Delta T_{sh,max}. \end{aligned} \tag{4.1}$$

A range of the input variables are given in Table 4.7.

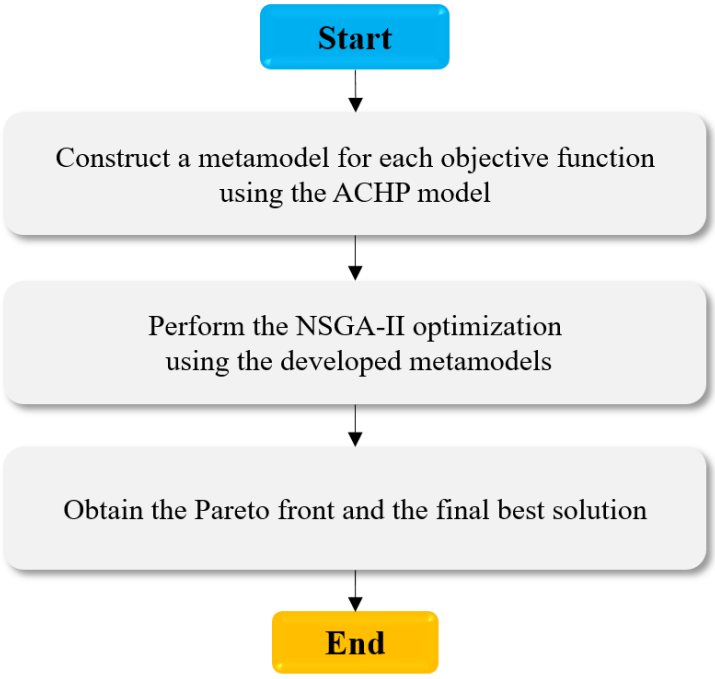

Figure 4.1: Flowchart for the proposed multi-objective optimization approach

Specifically, the scope of this work focuses on an air-source-split heat pump with 3-ton capacity, whose experimental validation data is available by Alabdulkarem et al. (2013), under the ASHRAE standard 116's A condition (ASHRAE, 1995) in cooling mode using R410A refrigerant.

4.2.2 ACHP Model Description

A validated vapor-compression system model, the Air Conditioning Heat Pump (ACHP) model (Bell, 2015; Bahman et al., 2018), is adopted in this study to simulate a heat pump. The ACHP model employs the $\varepsilon - NTU$ method and the moving boundary method on both refrigerant and airside to predict performance of a heat exchanger (Bell, 2015; Sarfraz et al., 2018). The next sections briefly introduce the configuration of the ACHP model.

4.2.2.1 Assumptions

The assumptions of the ACHP model are listed as follows.

- Isenthalpic process through the expansion device
- Uniform distribution on both air and refrigerant side
- Lumped approach on each refrigerant phase

4.2.2.2 Compressor Model

The 10-coefficient AHRI compressor map is applied to the compressor model (AHRI, 2015). The coefficients and equation are expressed in Table 4.1, respectively where X denotes the power input in Watt or refrigerant mass flow rate in lbm/hr, T_s and T_d are the suction and discharge dew point temperatures in degrees Fahrenheit, respectively, and C_1-C_{10} are coefficients acquired from least squares regression (AHRI, 2015) given in Table B.2. In the ACHP model, the map prediction is used after superheat correction (Dabiri and Rice, 1981) for universal use.

Table 4.1: AHRI 10-coefficient model (AHRI, 2015)

AHRI Formulation
$X = C_1 + C_2T_s + C_3T_d + C_4T_s^2 + C_5T_sT_d + C_6T_d^2 + C_7T_s^3 + C_8T_s^2T_d + C_9T_sT_d^2 + C_{10}T_d^3$

4.2.2.3 Heat Exchanger Model

The heat exchanger type is a Round-Tube-Plate-Fin Heat Exchanger (RTPF). The Moving boundary method is used to precisely predict performance of heat exchangers, accounting for phase change of fluids. The divided sections of a heat exchanger by

the moving boundary method are solved by applying the $\varepsilon - NTU$ method and empirical correlations summarized in Table 4.2, thus leading to computationally efficient calculations and satisfactory predictions.

Table 4.2: Correlations used in the model

Fluids	**Correlations**	**References**
Air	Heat transfer	Wang et al. (1998)
	Pressure drop	Wang et al. (1998)
	Fin efficiency	Perrotin and Clodic (2003)
Refrigerant	Heat transfer in single phase	Gnielinski (1976)
	Evaporation heat transfer in two-phase	Shah (1976)
	Condensation heat transfer in two-phase	Shah (1979)
	Pressure drop in single phase	Churchill (1977)
	Pressure drop in two-phase	Lockhart and Martinelli (1949)
	Void fraction in two-phase	Zivi (1964)

4.2.2.4 Charge Model

The ACHP model determines charge as the product of density and volume. Particularly in two-phase, the average density is defined as

$$\bar{\rho} = \rho_g \bar{\alpha} + \rho_f (1 - \bar{\alpha}), \tag{4.2}$$

where ρ_g and ρ_f are refrigerant densities in vapor and liquid phase, respectively, and $\bar{\alpha}$ is the average void fraction between inlet and outlet qualities. The Zivi void fraction model (Zivi, 1964) is used to estimate the void fraction in two-phase.

4.2.2.5 Cycle Solver Model

The direct-expansion-cycle solver is employed for the study. Two independent variables of the cycle solvers are refrigerant dew temperatures for evaporation, T_{eva} and condensation, T_{cnd}, respectively. The cycle solver adopts initial guess values of those dew temperatures to enable robust and efficient cycle calculation. The guess values

are obtained by solving a preconditioner using simple component models and two energy balances such as refrigerant to air and condenser heat transfer to a combination of compressor power and evaporator heat transfer.

Additionally, the main solver entails the two inputs, ΔT_{sc} and ΔT_{sh}. Based on the acquired dew temperatures and inputs, the solver calculation begins along the refrigerant flow from the evaporator model, followed by the compressor, condenser, expansion valve, and evaporator model. The cycle is updated for solving those independent variables, T_{eva} and T_{cnd}, by applying two constraints, an energy balance over the cycle and charge balance for the input subcooling (Bell, 2015). The ACHP model produces main output variables such as $\dot{Q}_{eva}$ and $m_{r,sys}$ as well as COP. Further details of the ACHP model are presented in Bell (2015).

4.2.3 ACHP Validation

This section confirms validations of the ACHP model in terms of $\dot{Q}_{eva}$ and $m_{r,sys}$ as well as COP. The prediction performance of the ACHP model in cooling mode was validated by an experimental data of an air source heat pump reported by Alabdulkarem et al. (2013). They presented experimental data of a 3-ton capacity split heat pump tested in accordance with ASHRAE standard 116 (ASHRAE, 1995). Detailed descriptions of the heat pump used in this validation are presented in Appendix B along with Tables B.1—B.4. The COP and $\dot{Q}_{eva}$ were evaluated by the ACHP model on ASHRAE standard cooling conditions (ASHRAE, 1995) as listed in Table 4.3 along with R410A as a working fluid; the corresponding experimental validation data set used in this validation are also presented in Table 4.4.

Table 4.3: Test matrix (Alabdulkarem et al., 2013)

Test classification	Indoor		Outdoor
	DB (°C)	WB (°C)	DB (°C)
A	26.7	19.4	35.0
B	26.7	19.4	27.8
C	26.7	13.9	27.8
Extended condition	26.7	19.4	46.1

Table 4.4: Experimental test conditions (Alabdulkarem et al., 2013) for validation of cooling capacity and COP

Test ID	**A**	**B**	**C**	**Extended**
ΔT_{sc} (K)	2.79	3.06	2.93	2.38
$\Delta T_{sh,out}$ (K)	2.05	2.04	0.65	2.09
$Q_{air,cnd}$ (m^3/s)	1.570	1.570	1.570	1.405
$T_{air,db,in}$ of condenser $(°C)$	34.7	27.1	26.9	46.8
RH_{in} of condenser	0.44	0.53	0.52	0.60
$Q_{air,eva}$ (m^3/s)	0.566	0.585	0.562	0.570
$T_{air,db,in}$ of evaporator $(°C)$	26.4	26.4	26.4	26.4
RH_{in} of evaporator	0.51	0.51	0.10	0.51

In addition, the validation of charge prediction by the ACHP model was performed on the standard A cooling condition (ASHRAE, 1995) as listed in Table 4.5 with variations of ΔT_{sc} and ΔT_{sh}.

Table 4.5: Experimental test conditions for validation of charge

Test ID	**A-0**	**A-1**	**A-2**	**A-3**	**A-4**
ΔT_{sc} (K)	2.8	0.7	2.9	3.4	4.4
$\Delta T_{sh,out}$ (K)	2.0	6.7	6.5	6.2	6.0
$Q_{air,cnd}$ (m^3/s)	1.570	1.570	1.570	1.570	1.570
$T_{air,db,in}$ of condenser $(°C)$	34.7	34.7	34.7	34.7	34.7
RH_{in} of condenser	0.44	0.44	0.44	0.44	0.44
$Q_{air,eva}$ (m^3/s)	0.566	0.566	0.566	0.566	0.566
$T_{air,db,in}$ of evaporator $(°C)$	26.4	26.4	26.4	26.4	26.4
RH_{in} of evaporator	0.51	0.51	0.51	0.51	0.51

The MAPE is employed to evaluate the prediction performance of the ACHP model. The MAPE is defined as

$$MAPE = \sum_{i=1}^{n} \left| \frac{Y_i - \hat{Y}_i}{Y_i} \right| \cdot \frac{100(\%)}{n} \tag{4.3}$$

where Y_i is an experimental validation data, $\hat{Y}_i$ is a predicted value and n is the number of test points used in the validation.

The validation results are presented in Figure 4.2 with prediction performance of the ACHP model; the MAPEs of $\dot{Q}_{eva}$, COP, and $m_{r,sys}$ are 4.5%, 2.5%, and 39.2%, respectively.

Systematic biases between the experimental data and predictions were observed, particularly showing underestimations of charge with a 39.2% MAPE. The systematic biases of the $\dot{Q}_{eva}$ and the COP were addressed by applying a tuning multiplier to the predicted value. The tuning multipliers are presented in Table 4.6.

Table 4.6: Tuning multipliers for the ACHP model

$\dot{Q}_{eva}$ (kW)	0.96
COP (-)	0.98

The charge of the heat exchangers in the $m_{r,sys}$ is tuned separately by using the $C_{regress,Zivi}$ introduced in Equation 3.21.

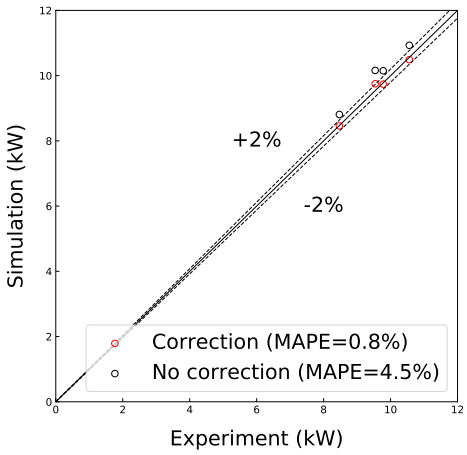

(a) $\dot{Q}_{eva}$

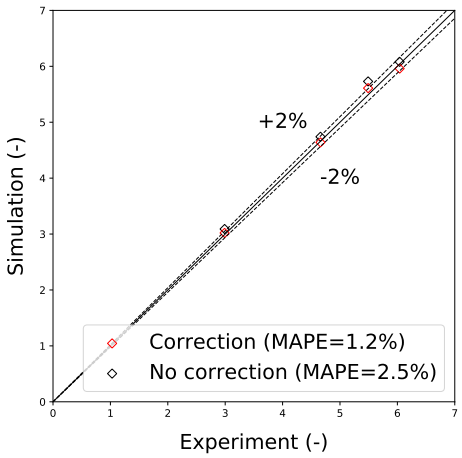

(b) COP

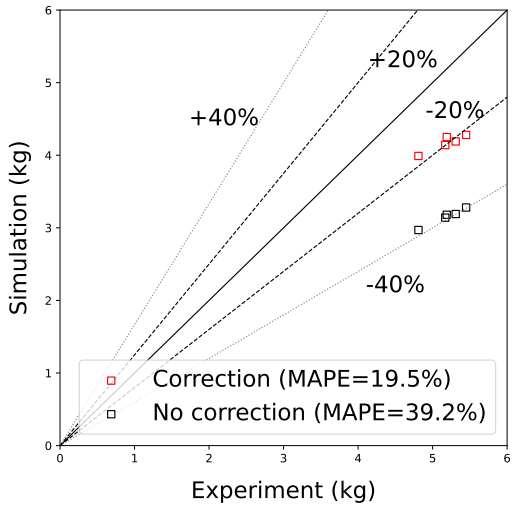

(c) $m_{r,sys}$

Figure 4.2: Comparison of prediction of the ACHP model with experimental data (Alabdulkarem et al., 2013)

As a result, the tuned ACHP model can provide sufficiently accurate predictions with 0.8%, 1.2%, and 19.5% of MAPE in terms of the $\dot{Q}_{eva}$, the COP, and the $m_{r,sys}$, respectively as demonstrated in Figure 4.2. In the following sections, the proposed multi-objective optimization takes advantage of the tuned ACHP model.

4.2.4 Surrogate Model Description

Surrogate models have been used to produce approximation of objective functions. The RBF surrogate model is one of the popular surrogate models. It was initially introduced by Hardy (1971) to interpolate irregular topographic contour of geographical data.

According to Hardy (1971) and Rocha (2009), the RBF surrogate model is described as follows; $\hat{f}(\mathbf{X})$ approximates an original objective function for point $\mathbf{X}$, $f(\mathbf{X})$ by a linear combination of radial basis function with coefficients expressed as

$$\hat{f}(\mathbf{X}) = \sum_{j=1}^{N} \alpha_j \varphi \left(\left\| \mathbf{X} - \mathbf{X}^j \right\| \right), \tag{4.4}$$

where $\mathbf{X}$ is the input variable (ΔT_{sc}, ΔT_{sh}) in a vector form, $\mathbf{X}^j$ are the N sampled points, j=1,...,N, α_j are coefficients to be determined, and $\varphi(\cdot)$ represents a radial basis function.

The Thin-plate spline function is used as radial basis function defined as $\varphi(r)$=r^2log(r); $\|\mathbf{X} - \mathbf{X}^j\|$ denotes the Euclidean distance between $\mathbf{X}$ and $\mathbf{X}^j$ expressed as

$$\left\| \mathbf{X} - \mathbf{X}^j \right\| = \sqrt{\sum_{p=1}^{n} \left(\mathbf{X}_p - \mathbf{X}_p^j \right)^2} \tag{4.5}$$

where p represents n-dimensional space. The Euclidean distance refers to the "normal" distance; for instance, it is the actual distance between two points in 2-D or 3-D space (Patel and Upadhyay, 2020; Song et al., 2022).

In Equation 4.4, α_j is the only-unknown coefficients to be solved. It can be obtained by solving the following linear system of interpolation equations along with the given objective function:

$$\sum_{j=1}^{N} \alpha_j \varphi \left(\left\| \mathbf{X}^k - \mathbf{X}^j \right\| \right) = f(\mathbf{X}^k), for\ k = 1, ..., N \tag{4.6}$$

where $f(\mathbf{X}^k)$ is the given k-th objective function of $\mathbf{X}$.

In other words, Equation 4.6 can be rewritten in a matrix form as

$$\Phi \begin{pmatrix} \alpha_1 \\ \alpha_2 \\ \vdots \\ \alpha_N \end{pmatrix} = \begin{pmatrix} f(\mathbf{X}^1) \\ f(\mathbf{X}^2) \\ \vdots \\ f(\mathbf{X}^N) \end{pmatrix} \tag{4.7}$$

where Φ is the interpolation matrix expressed as

$$\Phi = \begin{pmatrix} \varphi\left(\|\mathbf{X}^1 - \mathbf{X}^1\|\right) & \varphi\left(\|\mathbf{X}^1 - \mathbf{X}^2\|\right) & \cdots & \varphi\left(\left\|\mathbf{X}^1 - \mathbf{X}^N\right\|\right) \\ \varphi\left(\|\mathbf{X}^2 - \mathbf{X}^1\|\right) & \varphi\left(\|\mathbf{X}^2 - \mathbf{X}^2\|\right) & \cdots & \varphi\left(\left\|\mathbf{X}^2 - \mathbf{X}^N\right\|\right) \\ \vdots & \vdots & \ddots & \vdots \\ \varphi\left(\left\|\mathbf{X}^N - \mathbf{X}^1\right\|\right) & \varphi\left(\left\|\mathbf{X}^N - \mathbf{X}^2\right\|\right) & \cdots & \varphi\left(\left\|\mathbf{X}^N - \mathbf{X}^N\right\|\right) \end{pmatrix}. \tag{4.8}$$

In short, α_j are the only unknowns. Accordingly, once α_j is numerically calculated from the matrix, $\hat{f}(\mathbf{X})$ at any arbitrary $\mathbf{X}$ in the design space can be estimated by Equation 4.4. The obtained α_j are presented in Table C.2 and C.3.

The RBF surrogate model is constructed via the SciPy package in Python (Virtanen et al., 2020) for each $\dot{Q}_{eva}$ and $m_{r,sys}$ to facilitate the NSGA-II.

4.2.5 Active-Learning Data Sampling

The surrogate model needs to be accompanied by an effective data sampling, evaluations for $\dot{Q}_{eva}$ and $m_{r,sys}$ by the ACHP, since the accuracy of a surrogate model is influenced by a data sampling method (Gopakumar et al., 2018; Zhang et al., 2020).

Conventional design of experiments such as the Box-Behnken or the factorial designs are limited in this application due to their lack of iterative adaptation for data sampling; for this reason, an adaptive design of experiment, also known as active-

learning data sampling (Arboretti et al., 2022), is utilized to improve the global accuracy of the surrogate model by Zhou et al. (2017).

The active-learning data sampling based on the Space-Filling Cross-Validation Tradeoff (SFCVT) method (Aute et al., 2013) assists the surrogate model. This outperforms conventional data sampling methods due to their gradual adaptation along with their global search and excellent local refinement capabilities. Details of the active-learning data sampling are provided in Appendix D.

4.2.6 Non-dominated Sorting Genetic Algorithm (NSGA)-II

The optimal solutions to minimize $m_{r,sys}$ and maximize $\dot{Q}_{eva}$ simultaneously are selected through a myriad of heuristic search and evaluations of the objective functions that imitates the evolution and natural selection. In other words, the NSGA-II is accompanied with a host of evaluations of objective functions: for instance, Bahman et al. (2022) utilized a total of 10,000 different cases for choosing optimal solutions in their investigation. The numerous calculations of the NSGA-II can be burdensome in terms of time and resources; however, thanks to the surrogate model developed earlier, even countless calculations of the NSGA-II can be performed quickly and efficiently since the surrogate model provides an estimation of an objective function as a functional form such as Equation 4.4 rather than direct simulations by the ACHP model.

The main steps of the NSGA-II algorithm (Deb et al., 2002) to solve the optimization problem are presented in Figure 4.3 and below:

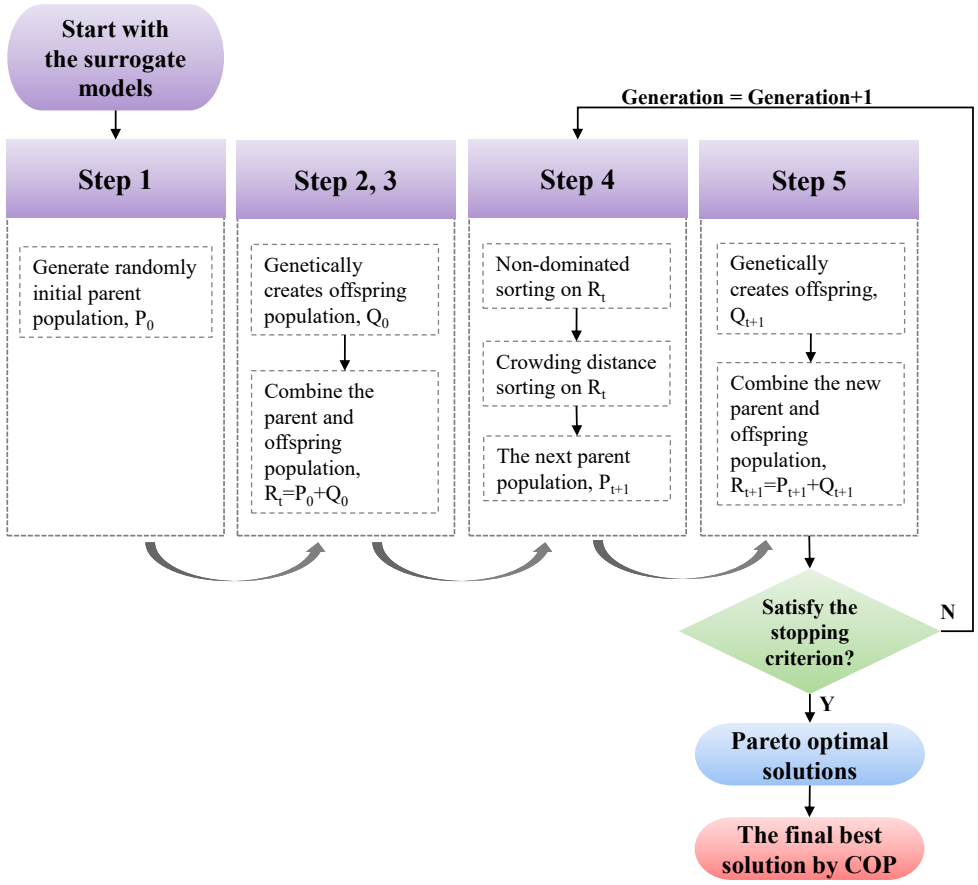

Figure 4.3: Flowchart of the NSGA-II for the current work

Step 1: A random parent population, P_0 is generated; then evaluations of objective function on the population is conducted by using the developed surrogate models.

Step 2: An offspring population, Q_0 is created from the parent population by genetic selection, crossover and mutation.

Step 3: P_0 and Q_0 are combined to form a combined population, R_t.

Step 4: The non-dominated sorting is performed on R_t by filtering the population ac-

cording to fitness with respect to the goal of the objective function. Subsequently, the crowding distance sorting is applied to R_t by estimating distances between neighboring populations, thus resulting in the next parent population, P_{t+1} that is genetically superior and well-scattered population.

Step 5: Again P_{t+1} yields the next offspring, Q_{t+1} by mutation and crossover, and then the next combined population, R_{t+1} is created by combining P_{t+1} and Q_{t+1}.

Step 6: Steps 4 and 5 are repeated until a maximum iteration count is satisfied.

Step 7: Lastly, the NSGA-II yields a set of optimal solutions, also known as the Pareto front, in which all the optimal solutions are non-dominated each other with respect to the objective functions. Inside the Pareto front, the solution to have the highest COP is selected as the best solution.

4.3 Result

4.3.1 Development of Surrogate Model for Cooling Capacity and Charge

A surrogate model is constructed according to the previously described method from Sections 4.2.4 and 4.2.5 for each $\dot{Q}_{eva}$ and $m_{r,sys}$. The surrogate model identifies the relationship between the objective function and the input variables for the 3-ton capacity heat pump described in Appendix B, particularly operating on the ASHRAE A condition (ASHRAE, 1995), shown earlier in Table 4.3.

While developing the surrogate models, the tuned ACHP model provides prediction of $\dot{Q}_{eva}$ and $m_{r,sys}$ as well as COP as a data sample with respect to ΔT_{sc} and ΔT_{sh}. The two input variables are bounded for keeping numerical stability, see Table 4.7.

Table 4.7: Range of input variables

$\Delta T_{sc,min}$	$\Delta T_{sc,max}$	$\Delta T_{sh,min}$	$\Delta T_{sh,max}$
1 K	10 K	2 K	20 K

The active-learning data sampling leads the development of the surrogate models along with 4 random initial samples and 15 random validation samples. In the end, the development of the surrogate models is terminated once a desirable accuracy of each surrogate model is achieved. The Root-Mean-Square Error (RMSE) is used for the stopping criterion along with the MAPE; the errors are evaluated on the random validation samples. The desirable RMSEs for each $\dot{Q}_{eva}$ and $m_{r,sys}$ are determined as 0.08 kW and 0.06 kg, the maximum experimental uncertainty (Alabdulkarem et al., 2013). Figure 4.4 verifies the sufficient accuracy, under the desirable RMSE, of the developed surrogate models at the 20 samples ($\mathbf{X}^j$), $X^1 \cdots X^{20}$ in Equation 4.4. The samples are presented in Table C.1.

Consequently, the trend of the accuracy along the number of samples, evaluations by ACHP, implies that the $\dot{Q}_{eva}$ and the $m_{r,sys}$ vary quite linearly without considerable non-linearity on the design space as demonstrated in Figure 4.5, thus resulting in the acquisition of the desirable accuracy of the surrogate model in the early stage of sampling data as shown Figure 4.4.

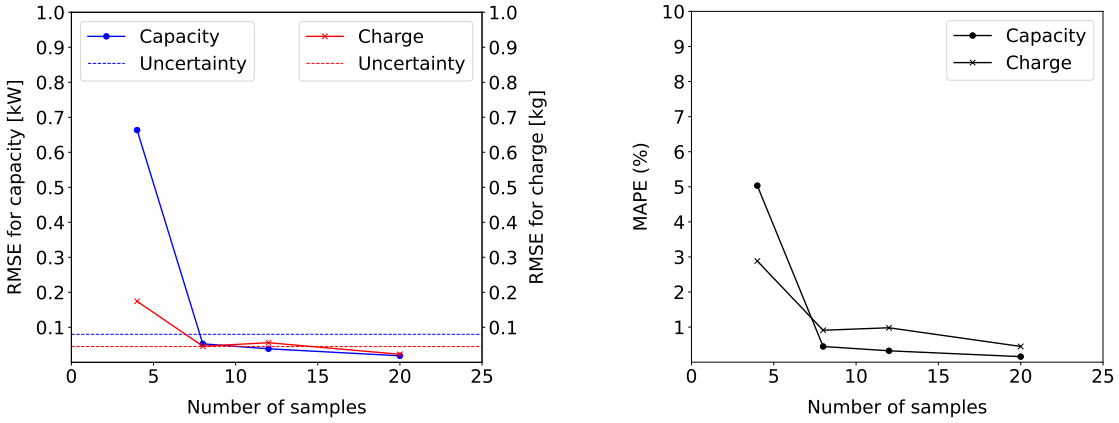

(a) RMSE (b) MAPE

Figure 4.4: Accuracy trend of the surrogate models according to the change in the number of samples acquired from ACHP. The experimental uncertainties are given as 0.08 kW and 0.06 kg for $\dot{Q}_{eva}$ and $m_{r,sys}$, respectively (Alabdulkarem et al., 2013).

Furthermore, the greatest merit of the surrogate model is to enable predictions of $\dot{Q}_{eva}$ and $m_{r,sys}$ at any point within the design space, a covered space by the

input variables. As a result, the estimated values of $\dot{Q}_{eva}$ and $m_{r,sys}$ by the surrogate models can be mapped on each contour plot as depicted in Figure 4.5. This fulfills the requirement of the NSGA-II to evaluate countless solutions instantaneously for solving the multi-objective optimization problem efficiently.

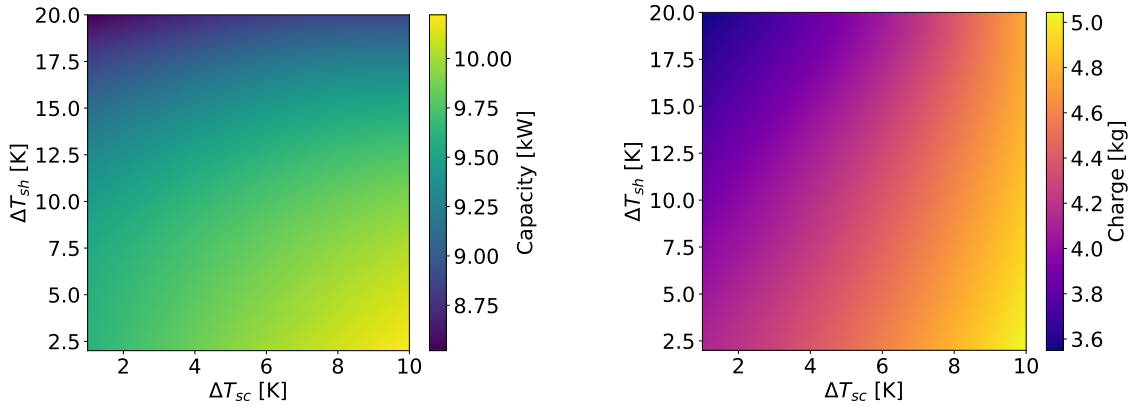

(a) $\dot{Q}_{eva}$ (b) $m_{r,sys}$

Figure 4.5: Contour plot of the predictions for each $\dot{Q}_{eva}$ and $m_{r,sys}$ by the developed surrogate models with 20 evaluations of ACHP

4.3.2 Trade-off between Cooling Capacity and Charge

Through the developed surrogate models, the trade-off between $\dot{Q}_{eva}$ and $m_{r,sys}$ can be seen clearly as shown in Figure 4.6. High ΔT_{sc} and low ΔT_{sh} are advantageous to $\dot{Q}_{eva}$. However this is not the case for $m_{r,sys}$; charge reduction can occur conversely in low ΔT_{sc} and high ΔT_{sh} as can be seen in Figure 4.6. These contrasting results give rise to a trade-off between $\dot{Q}_{eva}$ and $m_{r,sys}$. It is difficult to satisfy both objectives simultaneously; therefore the following multi-objective genetic algorithm is needed to solve this trade-off problem.

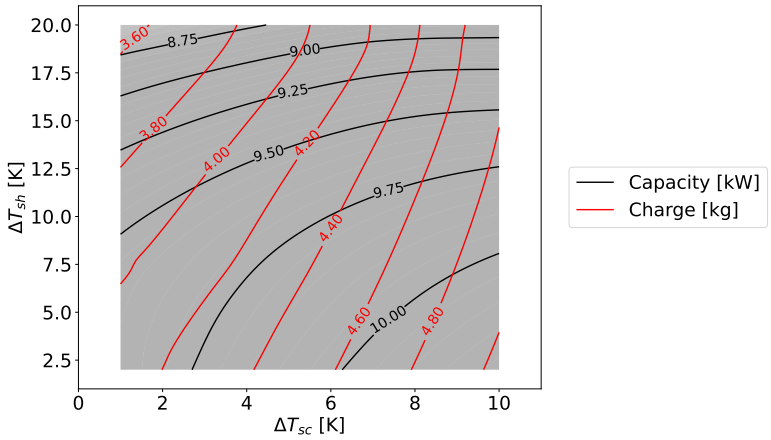

Figure 4.6: Overlapped contour plot of the surrogate models

4.3.3 Pareto Front

It is all set to have the NSGA-II run its algorithm to produce optimal solutions, non-dominated each other in terms of the objective functions. The optimization process is carried out over 100 generations with 100 offspring in each generation with a probability of 90% and 20% for crossover and mutation, respectively, through a total of 10,000 evaluations. This huge number of evaluations is challenging in case of using individual evaluation by the ACHP, while the surrogate model allows quick evaluations within a second, 10,000,000 times faster than the ACHP as indicated in Table 4.8.

The surrogate model assists the NSGA-II to create a set of optimal solutions, also known as Pareto front, presented in Figure 4.7; in addition, selected optimal solutions are depicted for illustration purposes.

Table 4.8: Calculation time for the 10,000 evaluations by a PC equipped with Xeon CPU 3.70GHz with RAM 16GB

	ACHP	Surrogate model
Estimated absolute calculation time	27.8 hr	0.01 s
Relative calculation time	100%	0.00001%

It is noted that the optimal solutions in the Pareto front are the prime solutions that can be obtained within the simulation conditions; however they are not supe-

rior to each other in terms of objective functions. In other words, the evidence is insufficient to find the best solution among them given in Figure 4.7. In the following section, the additional decision making process is described for selecting the best solution.

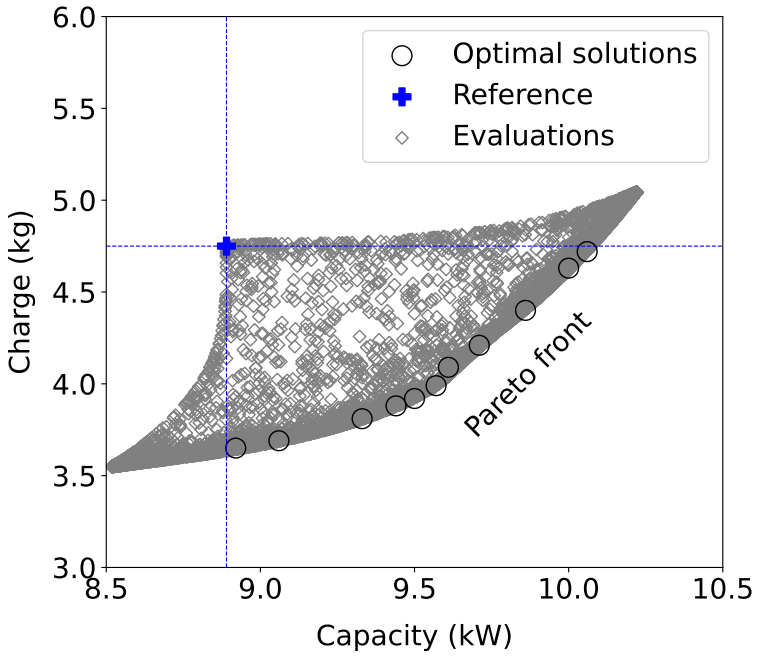

Figure 4.7: Pareto front with selected optimal solutions in the objective-function space

4.3.4 Decision Making for the Best Solution

Figure 4.8 presents the objective-function space including optimal solutions and reference point as well as the best solution. First of all, some distinct optimal solutions among the Pareto front are chosen as representatives for illustration purposes; the representative optimal solutions A and B are depicted in Figure 4.8 and Table 4.9 along with a reference point as a baseline having the maximum of ΔT_{sc} and ΔT_{sh}.

The solution A represents a maximum charge reduction with a minimal improvement of cooling capacity; on the contrary to this, the solution B represents a maximum improvement of cooling capacity with a marginal charge reduction; in other words,

they stand for each solution focused on charge-reduction and capacity-enhancement, respectively.

Other remaining optimal solutions are placed between the two solutions with respect to the objective functions. In order to pick the best solution among the Pareto front, the COP is adopted as a decision variable. Higher COP is beneficial; thus COPs are evaluated on the selected optimal solutions as exhibited in Figure 4.8; those are also listed in Table 4.9 for the representative solutions. Consequently, an optimal solution in the Pareto front having the highest COP is selected as the best solution of this multi-objective optimization on the trade-off between cooling capacity improvement and refrigerant charge reduction in a heat pump.

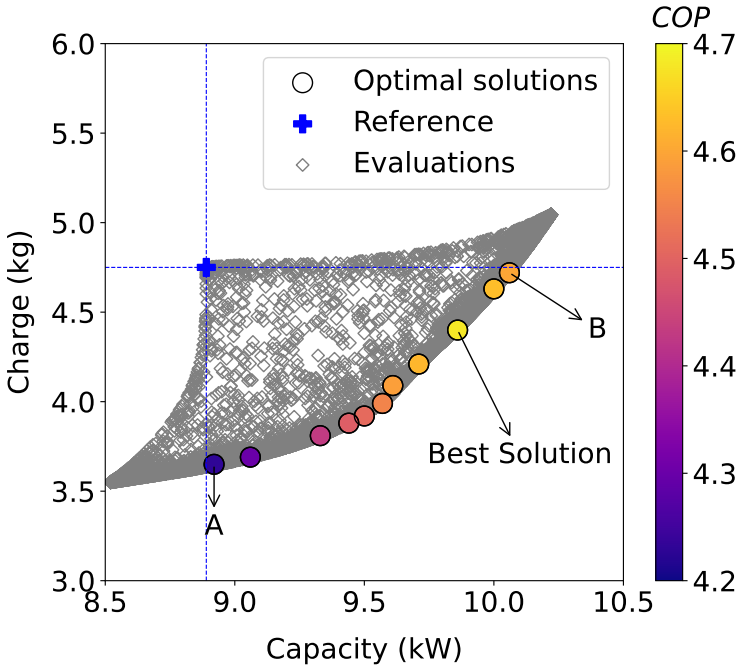

Figure 4.8: Selection of the best solution

Table 4.9: Representative optimal solutions and the reference

	ΔT_{sc} **[K]**	ΔT_{sh} **[K]**	$\dot{Q}_{eva}$ **[kW]**	$m_{r,sys}$ **[kg]**	**COP [-]**
Reference	10.0	20.0	8.89	4.75	3.85
Best solution	4.3	2.1	9.86	4.40	4.68
Solution A	1.1	17.1	8.92	3.65	4.23
Solution B	7.9	2.7	10.06	4.72	4.60

The best solution achieves an improvement with 10.9% and 21.6% of $\dot{Q}_{eva}$ and COP, respectively, while reducing $m_{r,sys}$ by 7.4% as summarized in Table 4.10. The best solution created by the NSGA-II along with the surrogate model is validated by comparison with a separate evaluation by the ACHP model as listed in Table 4.11; both deviations of $\dot{Q}_{eva}$ and $m_{r,sys}$ against the predictions of the ACHP fall under the accuracy of the tuned ACHP model presented in Section 4.2.3; accordingly this confirms validity of the best solution.

Table 4.10: Improvement of representative optimal solutions based on the reference

	$\dot{Q}_{eva}$	$m_{r,sys}$	**COP**
Best solution	10.9%	7.4%	21.6%
Solution A	0.3%	23.2%	9.9%
Solution B	13.2%	0.6%	19.5%

Table 4.11: Verification of the best solution predicted by the surrogate models against the prediction of the ACHP

	Predicted value	**Error**
$\dot{Q}_{eva}$ by the surrogate model	9.86 kW	0.1%
$\dot{Q}_{eva}$ by the ACHP	9.85 kW	
$m_{r,sys}$ by the surrogate model	4.40 kg	0.7%
$m_{r,sys}$ by the ACHP	4.37 kg	

The optimal solutions are explained on the design space including the ΔT_{sc} and ΔT_{sh} as shown in Figure 4.9.

Figure 4.9 shows, in overall, the $\dot{Q}_{eva}$ is more sensitive to the ΔT_{sh} than the ΔT_{sc}; on the other hand, $m_{r,sys}$ is more sensitive to the ΔT_{sc} than the ΔT_{sh} or impact of each input variable to $m_{r,sys}$ is relatively similar. It seems that the trend of $\dot{Q}_{eva}$

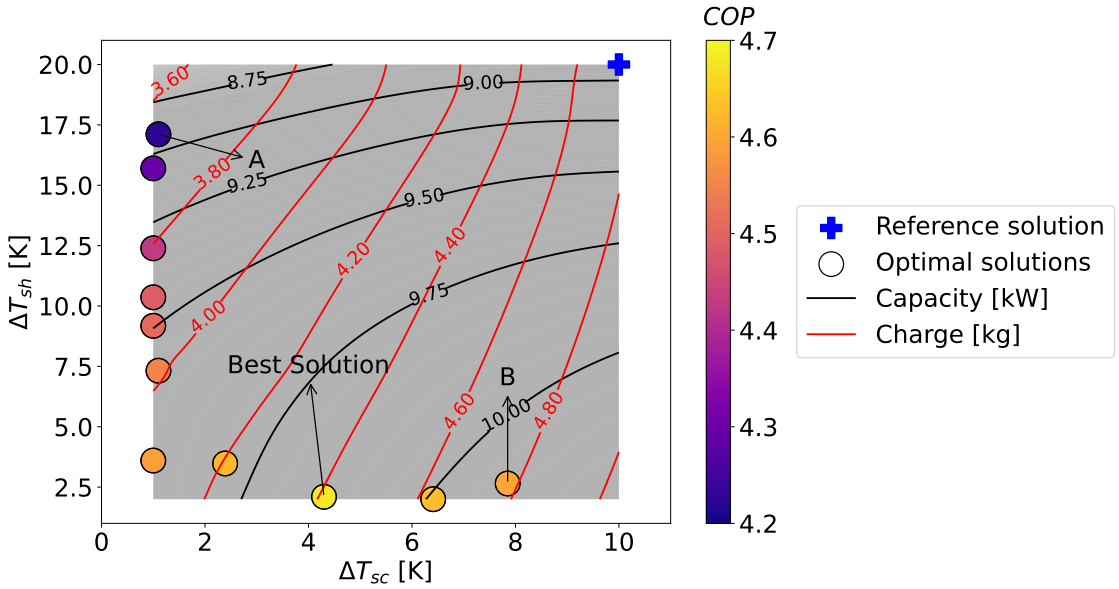

Figure 4.9: Optimal solutions on the design space along with the contour plot of $\dot{Q}_{eva}$ and $m_{r,sys}$

and $m_{r,sys}$ pushes the optimal solutions onto the boundary of the design space to be non-dominated by other solutions.

That is, the charge-reduction-focused solution, the solution A, is located in the low ΔT_{sc} region since the $m_{r,sys}$ is considerably affected by the ΔT_{sc} (Mei et al., 2005; Alabdulkarem et al., 2013); whereas, the cooling capacity-improvement-focused solution, the solution B, is placed in the low ΔT_{sh}. This might be due to the fact that the performance of the evaporator improves when ΔT_{sh} is kept as low as possible, thus yielding an increased two-phase refrigerant region in the evaporator (Rasmussen and Larsen, 2009).

In practice, the minimum ΔT_{sh} is dictated by many factors including non-linearity due to the point of operation, the evaporator design, and the characteristic of the expansion valve; moreover the minimum ΔT_{sh} is also affected by a safety margin to avoid two-phase suction of a compressor for a certain type of compressor.

In consequence, the best solution is located between the two extreme solutions, the solution A and B, while minimizing ΔT_{sh} and adjusting ΔT_{sc}, which is determined

by the maximum COP.

4.4 Conclusion

Refrigerant charge in a heat pump is highly correlated with cooling capacity of a heat pump in the trade-off relationship. This study developed a framework to optimize simultaneously both cooling capacity and charge in a heat pump in cooling mode by changing the ΔT_{sc} and ΔT_{sh}.

For predicting $\dot{Q}_{eva}$ and $m_{r,sys}$, the experimentally validated ACHP model is employed. Using the ACHP model, each surrogate model for each $\dot{Q}_{eva}$ and $m_{r,sys}$ is created and validated against the prediction of ACHP model.

The validated surrogate models enable sufficient evaluations (10,000) of objective functions almost instantaneously, thus assisting the NSGA-II to sufficiently and effectively evaluate the candidate solutions. With the aid of the surrogate models, the NSGA-II selects globally optimal solutions on the basis of the genetic algorithm combining the two criteria, non-dominated sorting and crowding distance sorting.

Among the optimal solutions, the best solution is chosen by considering COP, thus resulting in the best solution to maximize $\dot{Q}_{eva}$ and COP while minimizing $m_{r,sys}$ in the heat pump. Then, a separate evaluation by the ACHP confirms the best solution, although there is an underlying uncertainty in the charge prediction of the ACHP with an MAPE of 19.5% against the experimental data (Alabdulkarem et al., 2013), as stated in the validation of the ACHP.

In addition, the developed surrogate models allow estimation of both $\dot{Q}_{eva}$ and $m_{r,sys}$ in a heat pump throughout the entire design space, including ΔT_{sc} and ΔT_{sh}. The developed surrogate models for $\dot{Q}_{eva}$ and $m_{r,sys}$ demonstrate that the best solution can be acquired by minimizing ΔT_{sh} and adjusting ΔT_{sc} according to the sensitivity of the objective functions to the input variables, for the specific heat pump used in this study.

Furthermore, the developed surrogate models allow one to design or operate a system on not only the best point but also other optimal points with respect to $\dot{Q}_{eva}$ and $m_{r,sys}$ as well as other criteria, assisted by this validated framework.

In conclusion, the experimentally validated multi-objective optimization framework is developed for increasing $\dot{Q}_{eva}$ and reducing $m_{r,sys}$ without compromising COP. This validated framework also can be applied to many other multi-objective-multivariate engineering problems.

Future work will include conducting an experimental test on the obtained best solution to evaluate the performance of the optimization framework and provide feedback to the initial stage of the framework, extending the boundary of the design space for investigation of further improvement of the solutions, finding an optimal evaporator inlet quality, and developing a scalable multi-objective optimization framework to accommodate more objective functions and input variables.

Additionally, the sensitivity of the surrogate model was not analyzed in this work. The common surrogate models include support vector regression (Xiao et al., 2015), Kriging model (Kyprioti et al., 2020), polynomial response surface model (Eddy et al., 2015), and Radial Basis Function (RBF) model (Qasem et al., 2012; Zhou et al., 2017; Cai et al., 2017). The effects of the surrogate model on accuracy, numerical stability, and Pareto front will be investigated.

Likewise, future work will focus on explaining the sensitivity of the void-fraction model. Only the Zivi model was employed in this optimization work. Various void-fraction models will be used to discuss the effect of the void-fraction model on the Pareto front of the optimization framework.

CHAPTER V

CONCLUSIONS

5.1 Summary

This dissertation presented the experimentally validated refrigerant charge model for the RTPF heat exchanger and the experimental charge validation data as well as the optimization of refrigerant charge and cooling capacity in a heat pump.

Chapter 1 explains the result of literature review and niche the study tries to fill. Thus the research objectives are developed and stated. Subsequently, Chapter 2 provides a set of, high-quality, R410A experimental charge data. This experimental data includes a total of 42 tests of refrigerant charge for the RTPF heat exchanger, operating in both evaporator and condenser mode. The validated differential mass evacuation sampling method results in 0.1% of relative uncertainty with respect to measured charge and 1.3% of charge measurement repeatability. Additionally, charge sensitivity to independent variables was analyzed; in evaporator mode, charge is most sensitive to refrigerant inlet quality followed by outlet superheat. In condenser mode, subcooling followed by refrigerant mass flow rate is strongly correlated with charge. Chapter 3 adds the high-accuarcy refrigerant charge model tuned by high-fidelity experimental charge data for low-GWP refrigerants, R1234yf and R468C in addition to R410A as a reference. The complete and high-fidelity experimental charge data of the RTPF is first presented with ±2.2% of relative-charge measurement uncertainty of measured and 0.8% of charge-measurement repeatability. Thereafter, the accurate charge model is developed, tuned by the high-fidelity experimental charge data with

12.3%, 12.8%, and 12.9% of MAPE based on the Taitel-Barnea, the Zivi, and the Baroczy void-fraction model, respectively.

This experimentally validated and high-fidelity tuned charge model supports charge prediction of the optimization of refrigerant charge in a heat pump in Chapter 4. The developed framework solves concurrently two objectives, minimizing refrigerant charge and maximizing cooling capacity in a heat pump, and two input variables of the heat pump, subcooling in a condenser and superheat in an evaporator playing a determining role in performance and charge of a heat pump. The best solution is picked based on the COP after selecting a set of optimal solutions using the NSGA-II. The ACHP model allows predicting the cooling capacity and the refrigerant charge in a heat pump on various operating conditions, thus enabling the development of the surrogate model to expedite the algorithm of the NSGA-II. As a result, a set of optimal solutions are generated by the NSGA-II through 10,000 evaluations. Subsequently the best solution is selected by considering COP of the heat pump. The selected best solution obtains the improvement of 11.3% and 21.0% of $\dot{Q}_{eva}$ and COP, respectively, while reducing 17.2% of $m_{r,sys}$ from the reference point.

5.2 Conclusions

This research was initiated to fill the research gap found from the literature review: an insufficient charge-prediction accuracy of charge models and lack of experimental charge validation data for heat pumps in both evaporator and condenser mode and both indoor and outdoor RTPF heat exchangers to improve the accuracy of the charge models.

To acquire the experimental charge data, the study developed a novel charge measurement method, a differential mass evacuation sampling method. The method allows rapid and accurate charge measurements. The charge measurement facility was developed to execute the method. Prior to performing experimental campaign,

the charge measurement method was validated by comparison with a commercial refrigerant scale, thus yielding an error of 2.7 ± 1.7 g at 95% confidence interval with respect to 119 g of the mean measured charge by a refrigerant scale.

With this validated method and charge measurement facility, the experimental campaign was executed, producing a total of 52 test points including both evaporator and condenser mode, two RTPFs, and R410A refrigerant as well as low-GWP refrigerants, R1234yf and R468C. The repeatability and uncertainty of the charge measurement data verifies its high-fidelity and high-precision with a charge-measurement repeatability of 0.8% and a relative-charge measurement uncertainty of ±2.2%.

This high-quality database evaluated the existing charge model with six different void-fraction models. The result demonstrates that the Baroczy model shows the best agreement with the MAPE of 17.3%. Meanwhile, all of the void-fraction models require a correction for accurate charge prediction. Accordingly the high-fideliy charge data was used to tune the charge model. The adjusted correction factor was proposed for the tuning method; the correction factor is generated by a data-driven method that includes a regression equation and the ANN. As a result, the tuned T-B model shows the best agreement with the experimental data with the MAPE of 12.3%.

Finally, the developed high-fidelity charge model assists identifying an optimal charge by taking into account maximizing cooling capacity and COP of a heat pump on the developed multi-objective optimization framework, by changing the ΔT_{sc} and ΔT_{sh} according to the NSGA-II. As a result, it creates the globally best solution in the design space.

5.3 Future Work

Future work can focus on further improvement of accuracy of charge prediction for promising new low-GWP refrigerants. In addition, other factors for accurate charge prediction can be considered such as geometrical effects with additional heat ex-

changer tests and evaluating additional void-fraction models as well as investigating return bend and flow pattern effect. Moreover, the multi-objective optimization framework can be extended to accommodate generic engineering problems with many objective functions and input variables.

REFERENCES

Abdelaziz, O., Aute, V. and Radermacher, R. (2008), Effect of void fraction model on the dynamic performance of moving boundary heat exchanger, *in* 'Proceedings of 12^{th} International Refrigeration and Air Conditioning Conference', Purdue University.

AHRI (2015), *Performance rating of positive displacement refrigerant compressors and compressor units*, AHRI, AHRI Standard: Arlington, VA, USA.

Alabdulkarem, A., Hwang, Y. and Radermacher, R. (2013), System drop-in tests of refrigerants r-32, d2y-60, and l-41a in air source heat pump, *in* 'Air-Conditioning, Heating, and Refrigeration Institute (AHRI) Low-GWP Alternative Evaluation Program'.

Arboretti, R., Ceccato, R., Pegoraro, L. and Salmaso, L. (2022), 'Design of experiments and machine learning for product innovation: A systematic literature review', *Quality and Reliability Engineering International* **38**(2), 1131–1156.

ASHRAE (1995), *Standard 116-1995; Method of Testing for Rating Seasonal Efficiency of Unitary Air Conditioners and Heat Pumps*, ASHRAE Standard: Atlanta, GA, USA.

ASHRAE (2016), *Standard33; Methods of Testing Forced Circulation Air Cooling and Air Heating Coils*, ASHRAE Standard: Atlanta, GA, USA.

ASME-PTC-19.1 (2013), *Test Uncertainty – Performance Test Codes*, American Society of Mechanical Engineers, New York, USA.

Aute, V., Saleh, K., Abdelaziz, O., Azarm, S. and Radermacher, R. (2013), 'Cross-validation based single response adaptive design of experiments for kriging metamodeling of deterministic computer simulations', *Structural and Multidisciplinary Optimization* **48**(3), 581–605.

Bahman, A. M., Parikhani, T. and Ziviani, D. (2022), 'Multi-objective optimization of a cold-climate two-stage economized heat pump for residential heating applications', *Journal of Building Engineering* **46**, 103799.

Bahman, A. M., Ziviani, D. and Groll, E. A. (2018), Validation of a charge-sensitive vapor-injected compression cycle model with economization, *in* 'Proceedings of 17^{th} International Refrigeration and Air Conditioning Conference', Purdue University.

Baroczy, C. (1963), *Correlation of liquid fraction in two-phase flow with application to liquid metals*, Atomics International, Washington, D.C., USA.

Bell, I. (2015), 'Air conditioning and heat pump model (achp),[online; accessed 22-sep2019]'.
URL: *https://github.com/CenterHighPerformanceBuildingsPurdue/ACHP*

Bell, I. H., Wronski, J., Quoilin, S. and Lemort, V. (2014), 'Pure and pseudo-pure fluid thermophysical property evaluation and the open-source thermophysical property library coolprop', *Industrial & Engineering Chemistry Research* **53**(6), 2498–2508.
URL: *http://pubs.acs.org/doi/abs/10.1021/ie4033999*

Blank, J. and Deb, K. (2020), 'Pymoo: Multi-objective optimization in python', *IEEE Access* **8**, 89497–89509.

Blasius, H. (1913), Das Ähnlichkeit bei Reibungsvorgängen in Flüssigkeiten, *in* 'Mitteilungen über Forschungsarbeiten auf dem Gebiete des Ingenieurwesens', Springer, pp. 1–41.

Cai, X., Qiu, H., Gao, L., Wei, L. and Shao, X. (2017), 'Adaptive radial-basis-function-based multifidelity metamodeling for expensive black-box problems', *AIAA journal* **55**(7), 2424–2436.

Cho, W., Jang, D. S., Lee, S. H., Yun, S. and Kim, Y. (2020), 'Refrigerant charge reduction in r600a domestic refrigerator-freezer by optimizing hot-wall condenser geometry', *International Journal of Refrigeration* **117**, 295–306.

Chollet, F. et al. (2015), 'Keras', *GitHub* .
URL: *https://github.com/fchollet/keras*

Chua, K. J., Chou, S. K. and Yang, W. (2010), 'Advances in heat pump systems: A review', *Applied energy* **87**(12), 3611–3624.

Chua, K. J., Chou, S. K., Yang, W. and Yan, J. (2013), 'Achieving better energy-efficient air conditioning–a review of technologies and strategies', *Applied Energy* **104**, 87–104.

Churchill, S. W. (1977), 'Friction-factor equation spans all fluid-flow regimes.', *Chemical Engineering* **84**(24), 91–92.

Cioncolini, A. and Thome, J. R. (2012), 'Void fraction prediction in annular two-phase flow', *International Journal of Multiphase Flow* **43**, 72–84.

Coddington, P. and Macian, R. (2002), 'A study of the performance of void fraction correlations used in the context of drift-flux two-phase flow models', *Nuclear Engineering and Design* **215**(3), 199–216.

Cowan, A. et al. (2004), 'Review of recent commercial roof top unit field studies in the pacific northwest and california', *White Salmon, Wash: New Buildings Institute* .

Crombecq, K., Gorissen, D., Deschrijver, D. and Dhaene, T. (2011), 'A novel hybrid

sequential design strategy for global surrogate modeling of computer experiments', *SIAM Journal on Scientific Computing* **33**(4), 1948–1974.

Cui, Y., Geng, Z., Zhu, Q. and Han, Y. (2017), 'Multi-objective optimization methods and application in energy saving', *Energy* **125**, 681–704.

Currin, C., Mitchell, T., Morris, M. and Ylvisaker, D. (1988), A bayesian approach to the design and analysis of computer experiments, Technical report, Oak Ridge National Lab., TN (USA).

Dabiri, A. and Rice, C. (1981), 'A compressor simulation model with corrections for the level of suction gas superheat', *ASHARE Transactions* **87**(Part 2), 771–782.

Damavandi, M. D., Forouzanmehr, M. and Safikhani, H. (2017), 'Modeling and pareto based multi-objective optimization of wavy fin-and-elliptical tube heat exchangers using cfd and nsga-ii algorithm', *Applied Thermal Engineering* **111**, 325–339.

Deb, K., Pratap, A., Agarwal, S. and Meyarivan, T. (2002), 'A fast and elitist multiobjective genetic algorithm: NSGA-II', *IEEE transactions on evolutionary computation* **6**(2), 182–197.

Deng, Y., Yu, B. and Sun, D. (2020), 'Multi-objective optimization of guide vanes for axial flow cyclone using CFD, SVM, and NSGA-II algorithm', *Powder Technology* **373**, 637–646.

Ding, G., Ma, X., Zhang, P., Han, W., Kasahara, S. and Yamaguchi, T. (2009), 'Practical methods for measuring refrigerant mass distribution inside refrigeration system', *International Journal of Refrigeration* **32**(2), 327–334.

do Nascimento, C. A. R., Mariani, V. C. and dos Santos Coelho, L. (2020), 'Integrative numerical modeling and thermodynamic optimal design of counter-flow plate-fin

heat exchanger applying neural networks', *International Journal of Heat and Mass Transfer* **159**, 120097.

Dong, H., Wang, P., Chen, W. and Song, B. (2021), 'SGOP: Surrogate-assisted global optimization using a pareto-based sampling strategy', *Applied Soft Computing* **106**, 107380.

Eddy, D. C., Krishnamurty, S., Grosse, I. R., Wileden, J. C. and Lewis, K. E. (2015), 'A predictive modelling-based material selection method for sustainable product design', *Journal of Engineering Design* **26**(10-12), 365–390.

Eom, Y. H., Yoo, J. W., Hong, S. B. and Kim, M. S. (2019), 'Refrigerant charge fault detection method of air source heat pump system using convolutional neural network for energy saving', *Energy* **187**, 115877.

Ghadiri, M., Bach, C. K. and Bradshaw, C. R. (2022), R468C as a low-GWP replacement of R410A in fin-and-tube evaporators, *in* 'Proceedings of 19^{th} International Refrigeration and Air Conditioning Conference', Purdue University.

Ghoubali, R., Byrne, P. and Bazantay, F. (2017), 'Refrigerant charge optimisation for propane heat pump water heaters', *International Journal of Refrigeration* **76**, 230–244.

Gnielinski, V. (1976), 'New equations for heat and mass transfer in turbulent pipe and channel flow', *International Chemical Engineering* **16**(2), 359–368.

Goldberg David, E. and Henry, H. (1988), 'Genetic algorithms and machine learning', *Machine Learning* **3**(2), 95–99.

Gopakumar, A. M., Balachandran, P. V., Xue, D., Gubernatis, J. E. and Lookman, T. (2018), 'Multi-objective optimization for materials discovery via adaptive design', *Scientific Reports* **8**(1), 1–12.

Goswami, D., Ek, G., Leung, M., Jotshi, C., Sherif, S. and Colacino, F. (2001), 'Effect of refrigerant charge on the performance of air conditioning systems', *International Journal of Energy Research* **25**(8), 741–750.

Gramacy, R. B. and Lee, H. K. (2009), 'Adaptive design and analysis of supercomputer experiments', *Technometrics* **51**(2), 130–145.

Hardy, R. L. (1971), 'Multiquadric equations of topography and other irregular surfaces', *Journal of geophysical research* **76**(8), 1905–1915.

Harms, T. M. (2002), Charge inventory system modeling and validation for unitary air conditioners, PhD thesis, Purdue University.

Harms, T. M., Groll, E. A. and Braun, J. E. (2003), 'Accurate charge inventory modeling for unitary air conditioners', *HVAC&R Research* **9**(1), 55–78.

He, Y.-J., Liang, X.-Y., Cheng, J.-H., Shao, L.-L. and Zhang, C.-L. (2020), 'Approaching optimum COP by refrigerant charge management in transcritical co_2 heat pump water heater', *International Journal of Refrigeration* **118**, 161–172.

Heath, E. A. (2017), 'Amendment to the montreal protocol on substances that deplete the ozone layer (Kigali amendment)', *International Legal Materials* **56**(1), 193–205.

Hermes, C. J. (2015), 'Refrigerant charge reduction in vapor compression refrigeration cycles via liquid-to-suction heat exchange', *International Journal of Refrigeration* **52**, 93–99.

Hervas-Blasco, E., Pitarch, M., Navarro-Peris, E. and Corberán, J. M. (2018), 'Study of different subcooling control strategies in order to enhance the performance of a heat pump', *International Journal of Refrigeration* **88**, 324–336.

Holmström, K. (2008), 'An adaptive radial basis algorithm (arbf) for expensive black-box global optimization', *Journal of Global Optimization* **41**(3), 447–464.

Hu, X., Zhang, Z., Yao, Y. and Wang, Q. (2018), 'Non-azeotropic refrigerant charge optimization for cold storage unit based on year-round performance evaluation', *Applied Thermal Engineering* **139**, 395–401.

Hughmark, G. et al. (1962), 'Holdup in gas-liquid flow', *Chemical Engineering Progress* **58**(4), 62–65.

Jassim, E., Newell, T. and Chato, J. (2006), 'Refrigerant pressure drop in chevron and bumpy style flat plate heat exchangers', *Experimental Thermal and Fluid Science* **30**(3), 213–222.

Jiang, C., Cai, X., Qiu, H., Gao, L. and Li, P. (2018), 'A two-stage support vector regression assisted sequential sampling approach for global metamodeling', *Structural and Multidisciplinary Optimization* **58**(4), 1657–1672.

Jiang, L. (2015), Refrigerant charge reduction in small commercial refrigeration systems, Master's thesis, University of Illinois.

Jin, R., Chen, W. and Simpson, T. W. (2001), 'Comparative studies of metamodelling techniques under multiple modelling criteria', *Structural and multidisciplinary optimization* **23**(1), 1–13.

Jin, S. and Hrnjak, P. (2016), 'Refrigerant and lubricant charge in air condition heat exchangers: Experimentally validated model', *International journal of refrigeration* **67**, 395–407.

Juan, D. and Qin, Q. Z. (2014), 'Multi-objective optimization of a plain fin-and-tube heat exchanger using genetic algorithm', *Thermal Engineering* **61**(4), 309–317.

Kim, W. and Braun, J. E. (2012), 'Evaluation of the impacts of refrigerant charge on air conditioner and heat pump performance', *International Journal of Refrigeration* **35**(7), 1805–1814.

Kim, W., Han, Y., Kim, K. J. and Song, K.-W. (2020), 'Electricity load forecasting using advanced feature selection and optimal deep learning model for the variable refrigerant flow systems', *Energy Reports* **6**, 2604–2618.

Kingma, D. P. and Ba, J. (2014), 'Adam: A method for stochastic optimization', *arXiv preprint arXiv:1412.6980* .

Klein, S. A. and Alvarado, F. (1992), *EES: Engineering equation solver for the Microsoft Windows operating system*, F-Chart software, Madison, WI.

Kyprioti, A. P., Zhang, J. and Taflanidis, A. A. (2020), 'Adaptive design of experiments for global kriging metamodeling through cross-validation information', *Structural and Multidisciplinary Optimization* **62**(3), 1135–1157.

Lee, A. J., Bach, C. K. and Bradshaw, C. R. (2018), 'CFD case study: heat exchanger inlet air velocity distribution for ducted tests in a psychrometric chamber (ASHRAE RP-1785)'.

Lee, A. J., Bach, C. K. and Bradshaw, C. R. (2019), 'Study of heat exchanger inlet air velocity distribution for ducted tests in a psychrometric chamber.', *ASHRAE Transactions* **125**(2).

Lee, A. J., Bach, C. K. and Bradshaw, C. R. (2020), 'Differential mass evacuation sampling technique for measuring refrigerant charge and oil retention of round tube plate fin heat exchangers (ashrae rp-1785)', *Science and Technology for the Built Environment* **26**(6), 790–804.

Lee, A. J., Bach, C. K. and Bradshaw, C. R. (2021), Differential mass measurement scale for measuring refrigerant charge and oil retention of round tube plate fin heat exchangers (ASHRAE RP-1785), *in* 'Proceedings of 18^{th} International Refrigeration and Air Conditioning Conference', Purdue University.

Lee, A. J., Bach, C. K. and Bradshaw, C. R. (2022), Differential mass evacuation sampling method for measuring refrigerant charge in round tube plate fin heat exchangers (ASHRAE RP-1785), *in* 'Proceedings of 19^{th} International Refrigeration and Air Conditioning Conference', Purdue University.

Lee, D., Lee, M., Cho, W. and Kim, Y. (2021), 'Performance improvement of heat pumps by optimizing refrigerant charge using novel variable liquid-line length system', *Applied Thermal Engineering* **196**, 117287.

Lemmon, E., Bell, I. H., Huber, M. and McLinden, M. (2018), 'NIST standard reference database 23: Reference fluid thermodynamic and transport properties-REFPROP, version 10.0', *Standard Reference Data Program, Gaithersburg, MD* .

Li, G., Aute, V. and Azarm, S. (2010), 'An accumulative error based adaptive design of experiments for offline metamodeling', *Structural and Multidisciplinary Optimization* **40**(1), 137–155.

Li, K., Yu, J., Liu, M., Xu, D., Su, L. and Fang, Y. (2020), 'A study of optimal refrigerant charge amount determination for air-conditioning heat pump system in electric vehicles', *Energies* **13**(3), 657.

Li, W. and Hrnjak, P. (2021), 'Transient refrigerant and oil distribution in a residential heat pump water heater system: Experiments and model', *International Journal of Refrigeration* **129**, 184–193.

Li, Z., Shen, B. and Gluesenkamp, K. R. (2021), 'Multi-objective optimization of low-gwp mixture composition and heat exchanger circuitry configuration for improved system performance and reduced refrigerant flammability', *International Journal of Refrigeration* **126**, 133–142.

Lifferth, S. O. (2009), Design and construction of a new psychrometric chamber, Master's thesis, Oklahoma State University.

Liu, H. and Cai, J. (2021), 'Improved superheat control of variable-speed vapor compression systems in provision of fast load balancing services', *International Journal of Refrigeration* **132**, 187–196.

Liu, H., Xu, S., Ma, Y., Chen, X. and Wang, X. (2016), 'An adaptive bayesian sequential sampling approach for global metamodeling', *Journal of Mechanical Design* **138**(1), 011404.

Lockhart, R. and Martinelli, R. (1949), 'Proposed correlation of data for isothermal two-phase, two-component flow in pipes.', *Chemical Engineering Progress* **45**(1), 39–48.

Long, T., Wu, D., Guo, X., Wang, G. G. and Liu, L. (2015), 'Efficient adaptive response surface method using intelligent space exploration strategy', *Structural and Multidisciplinary Optimization* **51**(6), 1335–1362.

Ma, J., Ding, X., Horton, W. T. and Ziviani, D. (2020), 'Development of an automated compressor performance mapping using artificial neural network and multiple compressor technologies', *International Journal of Refrigeration* **120**, 66–80.

Ma, X., Ding, G., Zhang, P., Han, W., Kasahara, S. and Yamaguchi, T. (2009), 'Experimental validation of void fraction models for r410a air conditioners', *International journal of refrigeration* **32**(5), 780–790.

MacArthur, J. W. (1984), 'Transient heat pump behaviour: a theoretical investigation', *International Journal of refrigeration* **7**(2), 123–132.

Mackman, T. J., Allen, C. B., Ghoreyshi, M. and Badcock, K. (2013), 'Comparison

of adaptive sampling methods for generation of surrogate aerodynamic models', *AIAA journal* **51**(4), 797–808.

McLinden, M. O., Brown, J. S., Brignoli, R., Kazakov, A. F. and Domanski, P. A. (2017), 'Limited options for low-global-warming-potential refrigerants', *Nature Communications* **8**(1), 14476.

Mei, V., Chen, F. and Gao, Z. (2005), 'Development of a nonintrusive refrigerant charge indicator', *ASHRAE Transactions* **111**, 276.

Meng-ting, C., Xiao-wei, F., Zhong-hua, D., Xi, L., Xiao-long, W., Yuan-wu, X. and Tao, X. (2019), Data-driven fault detection for sofc system based on random forest and svm, *in* '2019 Chinese Automation Congress (CAC)', IEEE, pp. 2829–2834.

Miller, W. (1985), 'The laboratory evaluation of the heating mode part-load operation of an air-to-air heat pump', *ASHRAE Trans.;(United States)* **91**(CONF-850606-).

Minitab (2021), 'Minitab (version 20.2)', *Minitab LLC., State College, PA* .
URL: *https://www.minitab.com*

Mirjalili, S., Mirjalili, S. M. and Lewis, A. (2014), 'Grey wolf optimizer', *Advances in engineering software* **69**, 46–61.

Mousavi, S. M., Niaei, A., Salari, D., Panahi, P. N. and Samandari, M. (2013), 'Modelling and optimization of mn/activate carbon nanocatalysts for no reduction: comparison of rsm and ann techniques', *Environmental technology* **34**(11), 1377–1384.

Patel, S. P. and Upadhyay, S. H. (2020), 'Euclidean distance based feature ranking and subset selection for bearing fault diagnosis', *Expert Systems with Applications* **154**, 113400.

Pedregosa, F., Varoquaux, G., Gramfort, A., Michel, V., Thirion, B., Grisel, O., Blondel, M., Prettenhofer, P., Weiss, R., Dubourg, V., Vanderplas, J., Passos, A., Cournapeau, D., Brucher, M., Perrot, M. and Duchesnay, E. (2011), 'Scikit-learn: Machine learning in Python', *Journal of Machine Learning Research* **12**, 2825–2830.

Peng, H. and Ling, X. (2008), 'Optimal design approach for the plate-fin heat exchangers using neural networks cooperated with genetic algorithms', *Applied thermal engineering* **28**(5-6), 642–650.

Pereira, L., Humia, G., Khosravi, A., Revellin, R., Bonjour, J., Machado, L. and Pabon, J. J. G. (2019), 'A study on the fluid refrigerant charge in a two-phase mechanically pumped loop system using r134a and r1234yf', *Applied Thermal Engineering* **158**, 113727.

Perrotin, T. and Clodic, D. (2003), Fin efficiency calculation in enhanced fin-and-tube heat exchangers in dry conditions, *in* 'International Congress of Refrigeration', Vol. 18, Citeseer.

Peuker, S. (2010), *Experimental and analytical investigation of refrigerant and lubricant migration*, University of Illinois at Urbana-Champaign.

Poggi, F., Macchi-Tejeda, H., Leducq, D. and Bontemps, A. (2008), 'Refrigerant charge in refrigerating systems and strategies of charge reduction', *International Journal of Refrigeration* **31**(3), 353–370.

Prabakaran, R. and Mohan Lal, D. (2018), 'A novel exergy based charge optimisation for a mobile air conditioning system', *Journal of Thermal Analysis and Calorimetry* **132**(2), 1241–1252.

Premoli, A., Francesco, D. and Prina, A. (1971), 'A dimensional correlation for evaluating two-phase mixture density', *La Termotecnica* **25**(1), 17–26.

Proctor, J. P. (1997), 'Field measurements of new residential air conditioners in phoenix, arizona', *ASHRAE transactions* **103**, 406.

Qasem, S. N., Shamsuddin, S. M. and Zain, A. M. (2012), 'Multi-objective hybrid evolutionary algorithms for radial basis function neural network design', *Knowledge-Based Systems* **27**, 475–497.

Qureshi, B. A., Inam, M., Antar, M. A. and Zubair, S. M. (2013), 'Experimental energetic analysis of a vapor compression refrigeration system with dedicated mechanical sub-cooling', *Applied Energy* **102**, 1035–1041.

Rasmussen, H. and Larsen, L. F. (2009), Nonlinear superheat and capacity control of a refrigeration plant, *in* '2009 17th Mediterranean Conference on Control and Automation', IEEE, pp. 1072–1077.

Rice, C. (1987), 'The effect of void fraction correlation and heat flux assumption on refrigerant charge inventory predictions', *ASHRAE transactions* **93**(1), 341–367.

Rocha, H. (2009), 'On the selection of the most adequate radial basis function', *Applied Mathematical Modelling* **33**(3), 1573–1583.

Saad Yatim, A., Shashikant Deokar, P. and Cremaschi, L. (2017), 'Oil retention in a microchannel type condenser and its effects on heat transfer rate performance and on the pressure drop', *Science and Technology for the Built Environment* **23**(1), 166–180.

Safikhani, H. (2016), 'Modeling and multi-objective pareto optimization of new cyclone separators using CFD, ANN and NSGA-II algorithm', *Advanced Powder Technology* **27**(5), 2277–2284.

Saleem, S., Sarfraz, O., Bradshaw, C. R. and Bach, C. K. (2020), 'Development of novel experimental infrastructure for collection of high-fidelity experimental

data for refrigerant to air heat exchangers', *International Journal of Refrigeration* **114**, 189–200.

Saravanan, A. L., Murugan, R. S. and Lal, D. M. (2017), 'Investigations on charge reduction strategies to use R290 as an alternative to R22 in a split air conditioner', *Experimental Heat Transfer* **30**(2), 126–138.

Sarfraz, O. (2020), Development and Validation of a Reduced Order Fin-And-Tube Heat Exchanger Model, PhD thesis, Oklahoma State University.

Sarfraz, O., Bach, C. K. and Bradshaw, C. R. (2018), A literature review of numerical modeling techniques for vapor compression systems with focus on heat exchanger modeling, *in* 'Proceedings of 17^{th} International Refrigeration and Air Conditioning Conference', Purdue University.

Sarfraz, O., Bach, C. K. and Bradshaw, C. R. (2019), 'Discrete modeling of fin-and-tube heat exchangers with cross-fin conduction functionality', *International Journal of Refrigeration* **104**, 270–281.

Scire, F. J. (1968), 'Hermetic refrigeration compressors as applied to self-contained room air-conditioners', *IEEE Transactions on Industry and General Applications* (5), 567–574.

Shah, M. M. (1976), 'A new correlation for heat transfer during boiling flow through pipes', *ASHRAE Transactions* **82**(2), 66–86.

Shah, M. M. (1979), 'A general correlation for heat transfer during film condensation inside pipes', *International Journal of Heat and Mass Transfer* **22**(4), 547–556.

Shah, M. M. (1982), 'Chart correlation for saturated boiling heat transfer: equations and further study', *ASHRAE Trans.;(United States)* **88**(CONF-820112-).

Shen, B., Braun, J. E. and Groll, E. A. (2006), 'A method for tuning refrigerant charge in modeling off-design performance of unitary equipment (RP-1173)', *HVAC&R Research* **12**(3), 429–449.

Shojaeefard, M. H. and Zare, J. (2018), 'An investigation of the potential of improving an R1234yf parallel flow condenser performance using modeling and hybrid procedure of the modified nsga-ii and topsis', *Heat Transfer Engineering* **39**(15), 1405–1422.

Shojaeefard, M., Molaeimanesh, G., Yarmohammadi, A. and Changizian, S. (2017), 'Multi-objective optimization of an automotive louvered fin-flat tube condenser for enhancing HVAC system cooling performance', *Applied Thermal Engineering* **125**, 546–558.

Song, X., Wu, S., Li, G. and Lin, L. (2022), 'A calibration set selection method fusing multi-component based on euclidean distance in spectral analysis of complex solution', *Infrared Physics & Technology* **123**, 104116.

Taitel, Y. and Barnea, D. (1990*a*), Two-phase slug flow, *in* 'Advances in heat transfer', Vol. 20, Elsevier, pp. 83–132.

Taitel, Y. and Barnea, D. (1990*b*), Two-phase slug flow, *in* 'Advances in heat transfer', Vol. 20, Elsevier, pp. 83–132.

Tandon, T., Varma, H. and Gupta, C. (1985), 'A void fraction model for annular two-phase flow', *International Journal of Heat and Mass Transfer* **28**(1), 191–198.

Thom, J. (1964), 'Prediction of pressure drop during forced circulation boiling of water', *International Journal of Heat and Mass Transfer* **7**(7), 709–724.

Tyan, M. and Lee, J.-W. (2019), 'Efficient multi-response adaptive sampling algo-

rithm for construction of variable-fidelity aerodynamic tables', *Chinese Journal of Aeronautics* **32**(3), 547–558.

Virtanen, P., Gommers, R., Oliphant, T. E., Haberland, M., Reddy, T., Cournapeau, D., Burovski, E., Peterson, P., Weckesser, W., Bright, J., van der Walt, S. J., Brett, M., Wilson, J., Millman, K. J., Mayorov, N., Nelson, A. R. J., Jones, E., Kern, R., Larson, E., Carey, C. J., Polat, İ., Feng, Y., Moore, E. W., VanderPlas, J., Laxalde, D., Perktold, J., Cimrman, R., Henriksen, I., Quintero, E. A., Harris, C. R., Archibald, A. M., Ribeiro, A. H., Pedregosa, F., van Mulbregt, P. and SciPy 1.0 Contributors (2020), 'SciPy 1.0: Fundamental Algorithms for Scientific Computing in Python', *Nature Methods* **17**, 261–272.

Wang, C.-C., Fu, W. and Chang, C. (1997), 'Heat transfer and friction characteristics of typical wavy fin-and-tube heat exchangers', *Experimental thermal and fluid science* **14**(2), 174–186.

Wang, C.-C., Tsai, Y.-M. and Lu, D.-C. (1998), 'Comprehensive study of convex-louver and wavy fin-and-tube heat exchangers', *Journal of Thermophysics and Heat transfer* **12**(3), 423–430.

Wojtan, L., Ursenbacher, T. and Thome, J. R. (2005), 'Investigation of flow boiling in horizontal tubes: Part I—A new diabatic two-phase flow pattern map', *International Journal of Heat and Mass Transfer* **48**(14), 2955–2969.

Woldesemayat, M. A. and Ghajar, A. J. (2007), 'Comparison of void fraction correlations for different flow patterns in horizontal and upward inclined pipes', *International Journal of Multiphase Flow* **33**(4), 347–370.

Worthington, K. (2011), Calibration of the OSU psychrometric chamber and first experiments, PhD thesis, Oklahoma State University.

Wu, D., Hu, B. and Wang, R. (2021), 'Vapor compression heat pumps with pure low-gwp refrigerants', *Renewable and Sustainable Energy Reviews* **138**, 110571.

Xiao, M., Gao, L., Xiong, H. and Luo, Z. (2015), 'An efficient method for reliability analysis under epistemic uncertainty based on evidence theory and support vector regression', *Journal of Engineering Design* **26**(10-12), 340–364.

Yao, W., Chen, X. and Luo, W. (2009), 'A gradient-based sequential radial basis function neural network modeling method', *Neural Computing and Applications* **18**(5), 477–484.

Yin, X., Wang, A., Fang, J., Cao, F. and Wang, X. (2021), 'Coupled effect of operation conditions and refrigerant charge on the performance of a transcritical co_2 automotive air conditioning system', *International Journal of Refrigeration* **123**, 72–80.

Zhang, Z., Cheng, Q. S., Chen, H. and Jiang, F. (2020), 'An efficient hybrid sampling method for neural network-based microwave component modeling and optimization', *IEEE Microwave and Wireless Components Letters* **30**(7), 625–628.

Zhou, Q., Wang, Y., Jiang, P., Shao, X., Choi, S.-K., Hu, J., Cao, L. and Meng, X. (2017), 'An active learning radial basis function modeling method based on self-organization maps for simulation-based design problems', *Knowledge-Based Systems* **131**, 10–27.

Zivi, S. (1964), 'Estimation of steady-state steam void-fraction by means of the principle of minimum entropy production', *Journal of Heat Transfer* **86**, 247–251.

APPENDICES

APPENDIX A

EXPERIMENTAL CHARGE VALIDATION DATA FOR R410A REFRIGERANT

The appendices serves as valuable resources for further exploration and in-depth analysis of the research conducted. It offers a repository of supplementary materials, including raw data, extended tables, and additional figures, which enrich the understanding of this refrigerant charge study.

Table A.1: IC1 charge information in evaporator mode

	$\mathbf{m_{RTPF}}$	$\mathbf{u_{m,RTPF}}$	$\mathbf{u_{m,rel,RTPF}}$	$\mathbf{m_{RHXCT}}$	$\mathbf{u_{m,RHXCT}}$	$\mathbf{u_{m,RSV}}$	$\mathbf{\Delta m_{TW}}$	$\mathbf{u_{\Delta m_{TW}}}$	$\mathbf{\Delta m_{CW}}$	$\mathbf{u_{\Delta m_{CW}}}$
	g	g	%	g	g	g	g	g	g	g
IC1-1	401	±4.8	1.2	529.5	±4.7	±0.3	311.5	±3.4	841.0	±3.2
IC1-2	238	±4.8	2.0	344.6	±4.7	±0.2	309.7	±3.4	654.3	±3.3
IC1-3	371	±4.9	1.3	492.5	±4.8	±0.4	311.5	±3.4	804.0	±3.4
IC1-4	251	±4.8	1.9	355.5	±4.8	±0.4	311.6	±3.3	667.1	±3.4
IC1-5	364	±4.8	1.3	476.7	±4.7	±0.6	308.9	±3.3	785.6	±3.3
IC1-6	272	±4.7	1.7	376.5	±4.6	±0.6	324.5	±3.2	701.0	±3.3

Table A.2: IC1 charge information in condenser mode

	$\mathbf{m_{RTPF}}$	$\mathbf{u_{m,RTPF}}$	$\mathbf{u_{m,rel,RTPF}}$	$\mathbf{m_{RHXCT}}$	$\mathbf{u_{m,RHXCT}}$	$\mathbf{u_{m,RSV}}$	$\mathbf{\Delta m_{TW}}$	$\mathbf{u_{\Delta m_{TW}}}$	$\mathbf{\Delta m_{CW}}$	$\mathbf{u_{\Delta m_{CW}}}$	$\mathbf{m_{off}}$
	g	g	%	g	g	g	g	g	g	g	g
IC1-7	1165	±5.4	0.5	1456.9	±4.6	±0.1	472.3	±3.2	929.2	±3.3	1000
IC1-8	1124	±5.5	0.5	1414.2	±4.7	±0.1	579.8	±3.4	994	±3.3	1000
IC1-9	637	±5.4	0.9	923.4	±4.7	±0.1	584.9	±3.3	508.3	±3.3	1000
IC1-10	505	±5.4	1.1	787.8	±4.7	±0.5	584.9	±3.3	372.7	±3.3	1000
IC1-11	731	±5.4	0.7	1021.3	±4.7	±0.5	344.1	±3.2	365.4	±3.4	1000
IC1-12	769	±5.5	0.7	1057.4	±4.8	±0.5	579.8	±3.4	637.2	±3.3	1000
IC1-13	1504	±5.5	0.4	1797.7	±4.7	±0.1	506.5	±3.3	804.2	±3.3	1500
IC1-14	942	±5.5	0.6	1235.4	±4.7	±0.5	579.8	±3.4	815.2	±3.2	1000
IC1-15	497	±5.5	1.1	780.1	±4.7	±0.3	589.8	±3.3	369.9	±3.4	1000
IC1-16	1080	±5.5	0.5	1372.4	±4.7	±0.3	584.9	±3.3	957.3	±3.3	1000
IC1-17	514	±5.3	1	797.1	±4.5	±0.3	566.5	±3.2	363.6	±3.2	1000
IC1-18	1037	±5.5	0.5	1327.7	±4.7	±0.3	566.5	±3.2	894.2	±3.4	1000
IC1-19	684	±5.4	0.8	970.8	±4.6	±0.3	588.3	±3.3	559.1	±3.2	1000
IC1-20	638	±5.5	0.9	923	±4.8	±0.3	579.8	±3.4	502.8	±3.4	1000
IC1-21	581	±5.4	0.9	862.9	±4.7	±0.4	567.8	±3.2	430.7	±3.4	1000
IC1-22	955	±5.4	0.6	1246.1	±4.6	±0.3	566.5	±3.2	812.6	±3.3	1000

OC1 charge information

Table A.3: OC1 charge information in evaporator mode

	$\mathbf{m_{RTPF}}$	$\mathbf{u_{m,RTPF}}$	$\mathbf{u_{m,rel,RTPF}}$	$\mathbf{m_{RHXCT}}$	$\mathbf{u_{m,RHXCT}}$	$\mathbf{u_{m,RSV}}$	$\mathbf{\Delta m_{TW}}$	$\mathbf{u_{\Delta m_{TW}}}$	$\mathbf{\Delta m_{CW}}$	$\mathbf{u_{\Delta m_{CW}}}$	$\mathbf{m_{off}}$
	g	g	%	g	g	g	g	g	g	g	g
OC1-1	441	±6.6	1.5	508.5	±6.6	±0.3	462.6	±5.2	471.1	±4.1	500
OC1-2	299	±6.6	2.2	363.7	±6.6	±0.3	462.6	±5.2	326.3	±4.0	500
OC1-3	785	±5.3	0.7	854.9	±5.3	±0.8	649.4	±3.2	504.3	±4.2	1000
OC1-4	432	±4.6	1.1	498.1	±4.6	±0.5	729.7	±3.5	727.8	±3.0	500
OC1-5	843	±5.4	0.6	913.4	±5.4	±1.0	652.7	±4.0	566.1	±3.5	1000
OC1-6	619	±4.3	0.7	687.0	±4.3	±0.9	729.0	±3.0	916.0	±3.0	500

Table A.4: OC1 charge information in condenser mode

	$\mathbf{m_{RTPF}}$	$\mathbf{u_{m,RTPF}}$	$\mathbf{u_{m,rel,RTPF}}$	$\mathbf{m_{RHXCT}}$	$\mathbf{u_{m,RHXCT}}$	$\mathbf{u_{m,RSV}}$	$\mathbf{\Delta m_{TW}}$	$\mathbf{u_{\Delta m_{TW}}}$	$\mathbf{\Delta m_{CW}}$	$\mathbf{u_{\Delta m_{CW}}}$	$\mathbf{m_{off}}$
	g	g	%	g	g	g	g	g	g	g	g
OC1-7	4380	±5.3	0.1	4549	±5.2	±0.4	754.2	±3.7	302.7	±3.7	5000
OC1-8	4346	±4.3	0.1	4513	±4.3	±0.4	459.5	±3.0	472	±3.0	4500
OC1-9	2965	±4.5	0.2	3131	±4.5	±0.4	608.5	±3.2	739.2	±3.1	3000
OC1-10	1809	±4.4	0.2	1971	±4.4	±1.2	811.9	±3.1	783.2	±2.9	2000
OC1-11	2302	±4.3	0.2	2469	±4.3	±1.2	807.4	±2.8	276.5	±3.0	3000
OC1-12	2341	±4.8	0.2	2506	±4.8	±1.3	806.5	±3.2	312	±3.4	3000
OC1-13	4741	±4.1	0.1	4910	±4.1	±0.4	751.1	±2.9	661.2	±2.9	5000
OC1-14	3586	±5.1	0.1	3755	±5.0	±1.3	806	±3.5	560.9	±3.4	4000
OC1-15	1935	±4.1	0.2	2100	±4.1	±0.8	646.6	±2.8	246.9	±2.9	2500
OC1-16	4142	±4.9	0.1	4312	±4.9	±0.8	637.2	±3.9	449	±2.9	4500
OC1-17	2330	±6.9	0.3	2493	±6.9	±0.8	648.6	±5.8	641.9	±3.7	2500
OC1-18	4032	±4.8	0.1	4199	±4.7	±0.8	634.3	±3.5	333.2	±3.1	4500
OC1-19	3334	±5.6	0.2	3501	±5.6	±0.8	529.4	±4.5	530.5	±3.2	3500
OC1-20	3942	±4.7	0.1	4110	±4.7	±0.8	799.8	±3.6	909.5	±2.9	4000

Table A.5: Auxiliary charge information in the IC1 RHXCT in evaporator mode

	$\mathbf{m_{AUX}}$	$\mathbf{u_{m_{AUX}}}$	$\mathbf{m_{vap,cap}}$	$\mathbf{m_{liq}}$	$\mathbf{u_{m_{liq}}}$	$\mathbf{m_{vap}}$	$\mathbf{u_{m_{vap}}}$	$\mathbf{m_{tp}}$	$\mathbf{u_{m_{tp}}}$
	g	g	g	g	g	g	g	g	g
IC1-1	128.8	±1.0	0.9	64.4	±0.8	12.4	±0.1	51.1	±0.5
IC1-2	106.9	±0.9	0.8	61.7	±0.8	10.7	±0.1	33.7	±0.4
IC1-3	121.2	±0.9	0.8	64.8	±0.8	11	±0.1	44.6	±0.5
IC1-4	104.6	±0.9	0.7	62.8	±0.8	9.7	±0.1	31.3	±0.3
IC1-5	112.3	±0.9	0.8	64	±0.8	10.4	±0.1	37.2	±0.4
IC1-6	104.1	±0.9	0.7	64	±0.8	9	±0.1	30.5	±0.3

Auxiliary charge information

Table A.6: Auxiliary charge information in the IC1 RHXCT in condenser mode

	$\mathbf{m_{AUX}}$	$\mathbf{u_{m_{AUX}}}$	$\mathbf{m_{liq,cap}}$	$\mathbf{m_{liq}}$	$\mathbf{u_{m_{liq}}}$	$\mathbf{m_{vap}}$	$\mathbf{u_{m_{vap}}}$
	g	g	g	g	g	g	g
IC1-7	291.7	±2.8	17.2	256.8	±2.8	17.7	±0.2
IC1-8	289.7	±2.8	17.3	256.8	±2.8	15.6	±0.1
IC1-9	286.6	±2.8	17.4	253.4	±2.8	15.8	±0.1
IC1-10	282.4	±2.7	16.7	243.7	±2.7	22	±0.2
IC1-11	289.8	±2.8	16.7	250.1	±2.8	23	±0.2
IC1-12	287.9	±2.8	16.8	250.1	±2.8	21	±0.2
IC1-13	293.7	±2.9	16.9	258.6	±2.8	18.3	±0.2
IC1-14	293.9	±2.8	16.6	255.1	±2.8	22.1	±0.2
IC1-15	282.7	±2.7	16.8	245.3	±2.7	20.6	±0.2
IC1-16	292.6	±2.8	16.7	255.1	±2.8	20.8	±0.2
IC1-17	283	±2.7	17	248.5	±2.7	17.5	±0.2
IC1-18	291	±2.8	16.7	255.1	±2.8	19.2	±0.2
IC1-19	286.4	±2.8	16.7	250.1	±2.8	19.6	±0.2
IC1-20	284.7	±2.7	16.7	246.9	±2.7	21.1	±0.2
IC1-21	281.8	±2.7	16.6	242.2	±2.7	23	±0.2
IC1-22	290.7	±2.8	16.9	255.1	±2.8	18.7	±0.2

Table A.7: Auxiliary charge information in the OC1 RHXCT in evaporator mode

	$\mathbf{m_{AUX}}$	$\mathbf{u_{m_{AUX}}}$	$\mathbf{m_{vap,cap}}$	$\mathbf{m_{liq}}$	$\mathbf{u_{m_{liq}}}$	$\mathbf{m_{vap}}$	$\mathbf{u_{m_{vap}}}$	$\mathbf{m_{tp}}$	$\mathbf{u_{m_{tp}}}$
	g	g	g	g	g	g	g	g	g
OC1-1	67.1	±0.1	0.3	47.9	±0.1	4.7	±0.01	14.2	±0.03
OC1-2	64.2	±0.1	0.2	48.5	±0.1	3.9	±0.01	11.7	±0.03
OC1-3	70.2	±0.1	0.3	49.9	±0.1	4	±0.01	16	±0.04
OC1-4	66.2	±0.1	0.2	48.8	±0.1	4	±0.01	13.1	±0.03
OC1-5	70	±0.1	0.3	48.9	±0.1	4.4	±0.01	16.4	±0.04
OC1-6	68.4	±0.1	0.3	48.7	±0.1	4.1	±0.01	15.3	±0.04

Auxiliary charge information

Table A.8: Auxiliary charge information in the OC1 RHXCT in condenser mode

	$\mathbf{m_{AUX}}$	$\mathbf{u_{m_{AUX}}}$	$\mathbf{m_{liq,cap}}$	$\mathbf{m_{liq}}$	$\mathbf{u_{m_{liq}}}$	$\mathbf{m_{vap}}$	$\mathbf{u_{m_{vap}}}$
	g	g	g	g	g	g	g
OC1-7	169	±0.3	7.5	144.2	±0.3	17	±0.04
OC1-8	166	±0.3	7.5	143.9	±0.3	15.1	±0.04
OC1-9	166	±0.3	7.8	144.3	±0.3	14	±0.03
OC1-10	162	±0.3	7.4	137.7	±0.3	17	±0.04
OC1-11	167	±0.3	7.3	141.5	±0.3	18.6	±0.04
OC1-12	165	±0.3	7.3	140.9	±0.3	16.8	±0.04
OC1-13	169	±0.3	7.2	143.9	±0.3	18.3	±0.04
OC1-14	169	±0.3	7.1	142.7	±0.3	19	±0.04
OC1-15	166	±0.3	7.6	141.4	±0.3	16.5	±0.04
OC1-16	170	±0.3	7.2	143.2	±0.3	19.8	±0.05
OC1-17	163	±0.3	7.6	140.8	±0.3	14.6	±0.03
OC1-18	167	±0.3	7.2	142.7	±0.3	17.3	±0.04
OC1-19	167	±0.3	7.5	143.4	±0.3	16.3	±0.04
OC1-20	168	±0.3	7.3	143.2	±0.3	17.1	±0.04

Table A.9: Test result of IC1 in evaporator mode

	$\mathbf{P_{atm}}$	$\mathbf{T_{db,i}}$	$\mathbf{T_{wb,i}}$	$\mathbf{\dot{m}_{air}}$	$\mathbf{\dot{m}_r}$	$\mathbf{x_{in}}$	$\mathbf{P_{r,i}}$	$\mathbf{P_{r,o}}$	$\mathbf{T_{r,o}}$	$\mathbf{\Delta T_{sh,o}}$	$\mathbf{T_{r,sat,o}}$	$\mathbf{\dot{Q}_r}$	$\mathbf{\dot{Q}_a}$	$\mathbf{m_{RTPF}}$
	kPa	$°C$	$°C$	kg/s	kg/h	-	kPa	kPa	$°C$	K	$°C$	kW	kW	g
IC1-1	98	26.7	11.4	0.462	46.3	0.16	1394	1385	23.7	5.1	18.6	2.21	2.13	401
IC1-2	98	26.7	11.6	0.48	44.7	0.24	1253	1249	25.6	10.7	14.9	2.05	2	238
IC1-3	98	26.7	11	0.48	77.3	0.17	1252	1243	20.7	5.9	14.8	3.73	3.56	371
IC1-4	98	26.7	14.1	0.437	75.8	0.24	1155	1144	22.9	11	11.9	3.56	3.58	251
IC1-5	98	26.7	14.3	0.533	108.4	0.2	1181	1163	16.7	4.3	12.5	5.06	4.84	364
IC1-6	98	26.7	13.3	0.523	107.5	0.23	1080	1062	21.6	12.2	9.4	5.24	4.99	272

Test result

Table A.10: Test result of IC1 in condenser mode

	$\mathbf{P_{atm}}$	$\mathbf{T_{db,i}}$	$\mathbf{T_{wb,i}}$	$\mathbf{\dot{m}_{air}}$	$\mathbf{\dot{m}_r}$	$\mathbf{T_{r,i}}$	$\mathbf{P_{r,i}}$	$\mathbf{P_{r,o}}$	$\mathbf{T_{r,o}}$	$\mathbf{\Delta T_{sh,i}}$	$\mathbf{\Delta T_{sc}}$	$\mathbf{T_{r,sat,o}}$	$\mathbf{\dot{Q}_r}$	$\mathbf{\dot{Q}_a}$	$\mathbf{m_{RTPF}}$
	kPa	$°C$	$°C$	kg/s	kg/h	$°C$	kPa	kPa	$°C$	K	K	$°C$	kW	kW	g
IC1-7	97.2	21.1	14.8	0.27	24.2	46.7	1848	1847	22.6	17.4	6.7	29.3	1.44	1.43	1165
IC1-8	97.3	21.1	14	0.464	25	59.7	1796	1796	22.1	31.4	6.2	28.3	1.6	1.65	1124
IC1-9	97.6	21.1	15.4	0.284	22.7	52.4	1757	1755	24.4	25	3	27.4	1.38	1.38	637
IC1-10	97.3	21.1	15.4	0.569	91.4	60	2147	2147	32.6	24.8	2.7	35.2	5.27	5.27	505
IC1-11	98	21.1	15.3	0.609	89	51.3	2143	2141	28.5	16.2	6.6	35.1	5.04	5	731
IC1-12	96.7	21.1	15.4	0.835	84.1	64.7	2084	2082	27.4	30.7	6.6	34	5.21	5.07	769
IC1-13	98	21.1	15.4	0.283	22.7	57.8	2025	2023	21.8	25	11.1	32.9	1.42	1.43	1504
IC1-14	98	21.1	15.3	0.852	89.8	60.9	2181	2180	24.8	25	11.1	35.8	5.53	5.43	942
IC1-15	96.8	21.1	15.2	0.277	56.5	51.5	2099	2095	31.7	17.2	2.5	34.3	3.13	3.02	497
IC1-16	97.7	21.1	15.4	0.463	56.5	51.8	2121	2119	23.6	17.1	11.2	34.7	3.35	3.38	1080
IC1-17	97.7	21.1	15.4	0.459	56.9	65.2	1974	1971	28.8	33.4	3	31.9	3.52	3.55	514
IC1-18	98	21.1	15.4	0.46	56.7	69.1	2167	2165	24.1	33.6	11.5	35.6	3.67	3.62	1037
IC1-19	98	20.8	15.4	0.31	56.6	60.1	2115	2113	27.9	25.5	6.7	34.6	3.4	3.28	684
IC1-20	98.1	21.1	15.4	0.274	59.5	53.3	2158	2156	30	17.9	5.4	35.4	3.37	3.29	638
IC1-21	98	21.1	15.4	0.368	76.7	55.4	2210	2208	33.6	19	2.7	36.3	4.24	4.28	581
IC1-22	98	21.1	15.3	0.46	52.6	59.6	2045	2044	23.8	26.4	9.5	33.3	3.27	3.29	955

Table A.11: Test result of OC1 in evaporator mode

	$\mathbf{P_{atm}}$	$\mathbf{T_{db,i}}$	$\mathbf{T_{wb,i}}$	$\mathbf{\dot{m}_{air}}$	$\mathbf{\dot{m}_r}$	$\mathbf{x_{in}}$	$\mathbf{P_{r,i}}$	$\mathbf{P_{r,o}}$	$\mathbf{T_{r,o}}$	$\mathbf{\Delta T_{sh,o}}$	$\mathbf{T_{r,sat,o}}$	$\mathbf{\dot{Q}_r}$	$\mathbf{\dot{Q}_a}$	$\mathbf{m_{RTPF}}$
	kPa	$°C$	$°C$	kg/s	kg/h	-	kPa	kPa	$°C$	K	$°C$	kW	kW	g
OC1-1	96.3	8.5	4.3	0.816	58.5	0.27	889	872	6.9	3.9	3	2.63	2.71	441
OC1-2	96.7	8.3	3.4	0.823	51.5	0.28	747	732	5.4	7.9	-2.5	2.4	2.38	299
OC1-3	96.7	9	4.8	0.865	141.5	0.22	832	746	2.1	4.4	-1.9	6.8	6.56	785
OC1-4	97.2	8.4	4.8	0.665	90	0.26	788	748	4.5	6.3	-1.8	4.22	4.11	432
OC1-5	97.7	13.3	7.2	0.941	181.4	0.24	928	808	2.9	2.4	0.5	8.33	8.1	843
OC1-6	97.9	11.5	6.6	1.075	167.4	0.25	896	772	6.5	7.4	-0.9	7.88	7.63	619

Test result

Table A.12: Test result of OC1 in condenser mode

	$\mathbf{P_{atm}}$	$\mathbf{T_{db,i}}$	$\mathbf{T_{wb,i}}$	$\mathbf{\dot{m}_{air}}$	$\mathbf{\dot{m}_{r}}$	$\mathbf{T_{r,i}}$	$\mathbf{P_{r,i}}$	$\mathbf{P_{r,o}}$	$\mathbf{T_{r,o}}$	$\mathbf{\Delta T_{sh,i}}$	$\mathbf{\Delta T_{sc}}$	$\mathbf{T_{r,sat,o}}$	$\mathbf{\dot{Q}_{r}}$	$\mathbf{\dot{Q}_{a}}$	$\mathbf{m_{RTPF}}$
	kPa	$°C$	$°C$	kg/s	kg/h	$°C$	kPa	kPa	$°C$	K	K	$°C$	kW	kW	g
OC1-7	98.1	35	23.6	1.017	68.1	61.5	2739	2735	38	16.3	7.2	45.2	3.57	3.63	4380
OC1-8	98	35	23.6	1.015	68	79.6	2781	2775	38.4	33.8	7.4	45.8	3.99	4.03	4346
OC1-9	97.4	35	23.7	1.004	67.7	64.6	2439	2432	37.1	24.3	3.2	40.3	3.76	3.64	2965
OC1-10	98	35	23.6	1.017	224.9	73.4	2937	2888	44.6	25.9	2.9	47.5	11.8	11.35	1809
OC1-11	97.4	35	23.7	1.007	223.3	65.3	2971	2929	41.2	17.2	6.9	48.1	11.4	10.88	2302
OC1-12	98.1	35	23.7	1.021	226.3	82.1	3045	3002	41.9	32.9	7.2	49.2	12.83	12.25	2341
OC1-13	97.3	35	23.7	1.003	68	75.8	3133	3126	39.2	24.9	11.8	50.9	3.77	3.95	4741
OC1-14	98.1	34.7	23.3	1.014	228.1	77.2	3243	3211	40.6	25.1	11.5	52.1	12.49	12.02	3586
OC1-15	98	35	23.5	1.014	147.4	60	2666	2641	40.5	16.3	3.2	43.7	7.51	7.32	1935
OC1-16	98	35	23.7	1.016	148.2	67.6	3146	3135	39.9	16.6	11.2	51.1	7.67	7.65	4142
OC1-17	97.2	35	23.7	1.004	146.7	78.5	2693	2671	41.1	34.3	3.1	44.2	8.39	8.02	2330
OC1-18	98.1	35	23.6	1.024	145.7	84.7	3153	3143	40.4	33.5	10.8	51.2	8.46	8.24	4032
OC1-19	98	35	23.6	0.962	147.2	71.9	2823	2809	39	25.6	7.4	46.3	8.17	7.89	3334
OC1-20	98.1	35	16.1	1.028	135.7	76.3	3000	2985	39.6	27.4	9.3	48.9	7.6	7.57	3942

Internal volume information

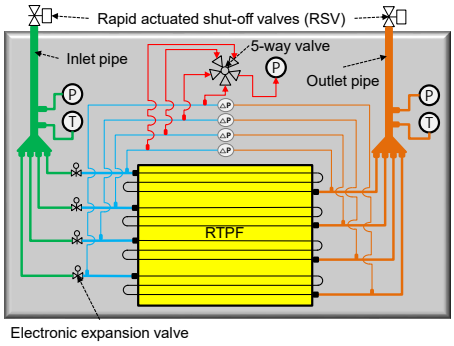

Color icon	Description of volume	Volume (ml)	Fractions (-)	Uncertainty (ml)
	Liquid subcooled	64.7	0.03	0.81
	Two-phase	189.4	0.08	2.20
	RTPF	1671.5	0.77	4.08
	Vapor superheated	238.9	0.11	2.63
	Vapor superheated in capillary pipe	16.6	0.01	-
	Total	**2181.1**	**1.00**	**5.39**

Figure A.1: Internal volume information of the IC1-RHXCT according to each refrigerant state in evaporator mode

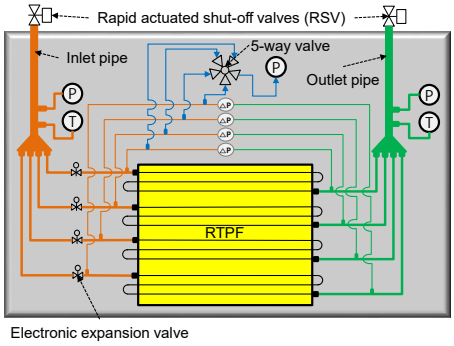

Color icon	Description of volume	Volume (ml)	Relative volume (-)	Uncertainty (ml)
	Liquid subcooled	238.9	0.11	2.63
	RTPF	1671.5	0.77	4.08
	Vapor superheated	254.1	0.11	2.34
	Liquid subcooled in capillary pipe	16.6	0.01	-
	Total	**2181.1**	**1.00**	**5.39**

Figure A.2: Internal volume information of the IC1-RHXCT according to each refrigerant state in condenser mode

Internal volume information

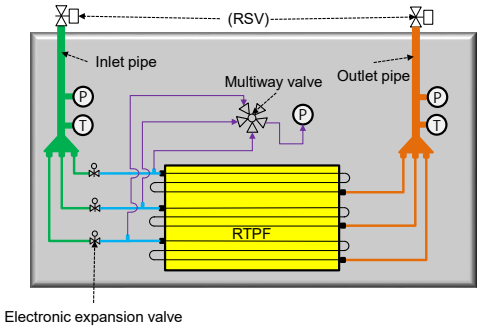

Color icon	Description of volume	Volume (ml)	Relative volume (-)	Uncertainty (ml)
	Subcooled liquid	48.8	0.01	0.1
	RTPF	4901	0.94	10.2
	Superheated vapor	145.4	0.03	0.3
	Superheated vapor in capillary pipe	8	0.00	-
	Two-phase	123.1	0.02	0.3
	Total	**5226**	**1.00**	**10.2**

Figure A.3: Internal volume information of the OC1-RHXCT according to each refrigerant state in evaporator mode

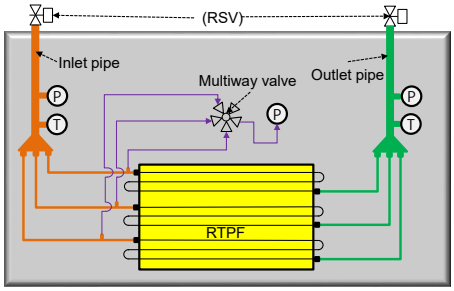

Color icon	Description of volume	Volume (ml)	Relative volume (-)	Uncertainty (ml)
	Subcooled liquid	145	0.03	0.3
	RTPF	4901	0.94	10.2
	Superheated vapor	171	0.03	0.4
	Subcooled liquid in capillary pipe	8	0.00	-
	Total	**5225**	**1.00**	**10.2**

Figure A.4: Internal volume information of the OC1-RHXCT according to each refrigerant state in condenser mode

APPENDIX B

INFORMATION OF ACHP VALIDATION

Detailed information of the ACHP's performance validation is presented based on Alabdulkarem et al. (2013)'s published data. The COP is defined as a ratio of cooling capacity to a compressor input power (Alabdulkarem et al., 2013).

Table B.1: Heat pump specifications

Heat pump manufacturer	Goodman
Heat exchangers type	Round tube plate fin
Outdoor unit model number	SSZ140361BA
Indoor unit model number	ARUF374316
Compressor manufacturer	Copeland
Compressor type	Single speed 3-ton scroll
Compressor model number	ZP29K5EPFV130
Working fluid	R410A

Table B.2: 10-coefficient AHRI compressor map for ZP29K5EPFV130

Coefficients	**Power (W)**	**Mass Flow (lbm/hr)**
C_1	-605.268	198.5648982
C_2	-16.7291	4.4706942
C_3	47.34564	-0.3769426
C_4	-0.1313	0.0331605
C_5	0.368906	-0.0080514
C_6	-0.43604	0.0056885
C_7	0.000798	0.0001354
C_8	0.000529	0.0000227
C_9	-0.00213	0.0000370
C_{10}	0.002256	-0.0000393

Table B.3: Condenser specifications

Number of tubes per bank	38
Number of bank	1
Number of circuits	4
Length of tubes	2.286 m
Outer diameter of tube	0.00913 m
Inner diameter of tube	0.00849 m
Tube spacing in air flow direction	0.0191 m
Tube spacing orthogonal to air flow direction	0.0254 m
Number of fins per inch	20
Amplitude of wavy fin	0.001 m
Half period of wavy fin	0.001 m
Fin thickness	0.00011 m
Fin type	Wavy louvered fins

Table B.4: Evaporator specifications

Number of tubes per bank	44
Number of bank	2
Number of circuits	5
Length of tubes	0.51 m
Outer diameter of tube	0.00913 m
Inner diameter of tube	0.00849 m
Tube spacing in air flow direction	0.0191 m
Tube spacing orthogonal to air flow direction	0.0254 m
Number of fins per inch	14
Amplitude of wavy fin	0.001 m
Half period of wavy fin	0.001 m
Fin thickness	0.00011 m
Fin type	Wavy louvered fins

APPENDIX C

SURROGATE MODEL

The unknown coefficients of the surrogate model, α_j are calculated by solving the following matrix using the RBF interpolator solver in SciPy package on Python platform (Virtanen et al., 2020).

$$\alpha_j = \begin{pmatrix} \alpha_1 \\ \alpha_2 \\ \vdots \\ \alpha_N \end{pmatrix} = \Phi^{-1} \begin{pmatrix} f(\mathbf{X}^1) \\ f(\mathbf{X}^2) \\ \vdots \\ f(\mathbf{X}^N) \end{pmatrix} \tag{C.1}$$

where $\mathbf{X}$ is the input variable (ΔT_{sc}, ΔT_{sh}), Φ^{-1} is the inverse matrix of the interpolation matrix given in Equation 4.8 and the $f(\mathbf{X}^k)$ is the given k-th each objective function of $\mathbf{X}$.

Table C.1: Used 20 ACHP samples for developing the surrogate models

$\mathbf{\Delta T_{sc}}$	$\mathbf{\Delta T_{sh}}$	$\mathbf{\dot{Q}_{eva}}$	$\mathbf{m_{r,sys}}$
7.0	19.0	9.02	4.22
8.5	18.0	9.20	4.50
7.8	17.6	9.24	4.39
8.0	17.0	9.32	4.44
1.3	2.0	9.63	4.15
1.0	2.0	9.61	4.13
1.6	2.0	9.66	4.17
1.0	2.6	9.61	4.12
9.7	20.0	8.89	4.70
10.0	20.0	8.89	4.75
10.0	19.4	8.99	4.76
9.4	20.0	8.89	4.64
1.7	7.0	9.61	4.04
1.9	7.5	9.61	4.04
1.9	7.0	9.62	4.06
1.6	7.6	9.59	4.02
1.0	18.8	8.70	3.59
1.3	20.0	8.54	3.57
1.0	20.0	8.52	3.55
1.0	19.4	8.61	3.57

The following Tables list the obtained coefficients for each objective function. A linearly combined the product of the coefficients and the radial basis function forms an RBF metamodel to produce approximate value of each objective function according to Equation 4.4.

Table C.2: The coefficients of the surrogate model for the $\dot{Q}_{eva}$

α_1	-0.06
α_2	1.84
α_3	-2.03
α_4	0.36
α_5	-6.54
α_6	7.84
α_7	2.80
α_8	-3.47
α_9	-38.19
α_{10}	25.17
α_{11}	-3.61
α_{12}	16.94
α_{13}	13.78
α_{14}	10.73
α_{15}	-13.09
α_{16}	-11.44
α_{17}	2.54
α_{18}	-4.45
α_{19}	9.96
α_{20}	-7.50

Table C.3: The coefficients of the surrogate model for the $m_{r,sys}$

α_1	0.207216
α_2	-0.12595
α_3	0.125146
α_4	-0.17253
α_5	-25.5596
α_6	15.64098
α_7	12.32413
α_8	-1.92107
α_9	-9.62314
α_{10}	5.447272
α_{11}	-0.94204
α_{12}	5.144594
α_{13}	2.022233
α_{14}	0.696467
α_{15}	-1.81746
α_{16}	-0.90305
α_{17}	2.565754
α_{18}	-2.36178
α_{19}	6.946469
α_{20}	-6.67869

APPENDIX D

ACTIVE-LEARNING DATA SAMPLING

This section details the active-learning data sampling; it refers to a data sampling method which gradually develop and adapt to improve a global accuracy of a surrogate model. It performs an initial sampling (pre-sampling) and then iteratively updating the surrogate model with more sampling points according to two crucial criteria , 'exploration' and 'exploitation' (Mackman et al., 2013; Long et al., 2015; Dong et al., 2021), and it is repeated until either termination of simulation resources or achievement of sufficient accuracy of the surrogate model (Gopakumar et al., 2018).

The 'exploration' criterion of the active-learning data sampling ensures spreading out sampling points throughout a design space for global-search capability, which is also known as space-filling sampling. Meanwhile, the 'exploitation' criterion, also known as refinement, of the active-learning data sampling focuses on improving local accuracy of a surrogate model by sampling (Crombecq et al., 2011).

In the open literature, the common exploration methods include the maximum entropy (Liu et al., 2016), the Voronoi partition (Cai et al., 2017), the Kriging variance (Kyprioti et al., 2020), and the Euclidean distance (Zhou et al., 2017; Eddy et al., 2015; Aute et al., 2013).

Meanwhile, the prevalent exploitation methods cover the maximum gradient (Yao et al., 2009), the maximum standard deviation and averaged squared errors (Gramacy and Lee, 2009), the estimation of non-linearity around data points (Crombecq et al., 2011), and the Leave-One-Out (LOO) errors in the cross-validation, e^{LOO} (Li et al., 2010; Aute et al., 2013; Liu et al., 2016; Cai et al., 2017; Kyprioti et al., 2020).

The inherent characteristic of the exploration and exploitation yields a trade-off between the exploration of 'global' samples and the exploitation of 'local' samples (Gopakumar et al., 2018; Zhang et al., 2020). Aute et al. (2013) well combined the two criteria in an optimization formulation and proposed an active-learning data sampling, called Space-Filling Cross-Validation Tradeoff (SFCVT). The SFCVT was then employed to construct surrogate models for both heat transfer coefficient and pressure drop of air to solve a problem for novel fin-and-tube heat exchanger design optimization (Aute et al., 2013). In a validation process of the optimization problem, the SFCVT produced high-fidelity surrogate models within 10% error, given 10-15% of experimental error (Aute et al., 2013).

Based on the verified SFCVT sampling, the proposed study developed a modified active-learning data sampling by adding adaptability to the exploration criterion for stable accommodation of various engineering problems. This approach is summarized in Figure D.1. It utilizes the Euclidean method as the exploration and e^{LOO} as the exploitation of data sampling.

According to the SFCVT method, a sample is optimally updated by finding the highest e_i^{LOO} while keeping a certain distance between the new sampling point and the existing points by the Euclidean distance method. The Euclidean method allows avoiding clustered sampling, finding candidate sample points while maintaining enough Euclidean distance from the existing points to the new sample points. Moreover it is easy to implement and numerically stable as well as the independence in type of surrogate model (Zhou et al., 2017; Eddy et al., 2015; Aute et al., 2013).

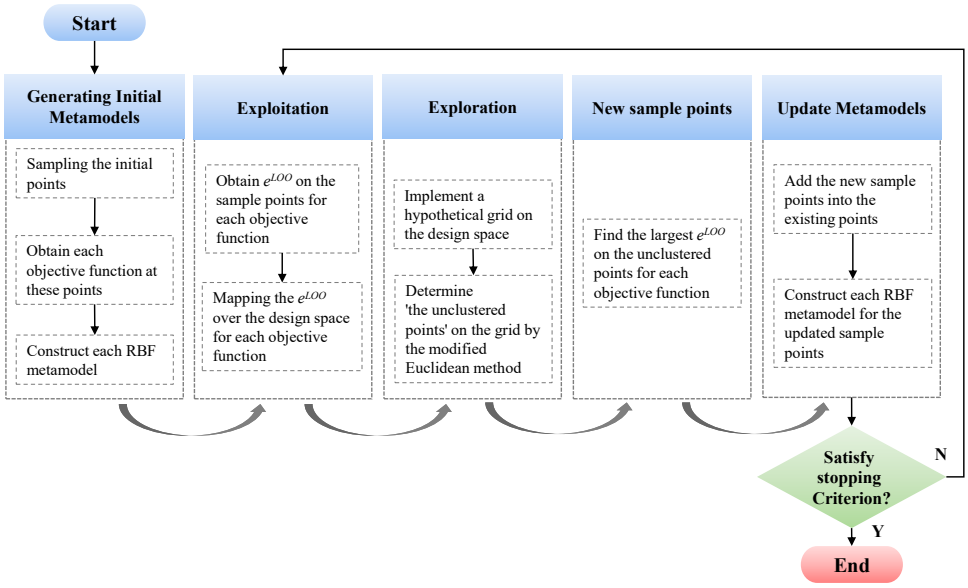

Figure D.1: Flowchart of the active-learning data sampling

The SFCVT method disclosed that it has better performance for 20 test problems compared to other design of experiments such as maximum entropy design and maximin scaled distance method (Aute et al., 2013).

In addition to the SFCVT, the proposed active-learning data sampling in this study adds adaptability to the exploration criterion by using a distance factor δ which can be adjusted according to a problem to be solved.

First of all, for efficient computation of the Euclidean method, points are created on a hypothetical-evaluation grid on the design space (Mackman et al., 2013). Then, all minimum distances from an existing point to all the grid points on the evaluation grid are calculated, averaged, and multiplied by a distance factor, δ to obtain a space-filling metric, S.

This process is carried out for each existing sample points. Finally the grid points on the evaluation grid that satisfies the space-filling metric, S are chosen for $x_{candidate}$ and ready to be combined with the exploitation criteria, e^{LOO} to select the next sampling points.

This exploration process is mathematically expressed as

$$
\begin{aligned}
ds(x_i) = min(\|x_i - x_{grid,i}\|),\ \forall\, x_i \in D\ , \forall\, x_{grid,i} \in G \\
S = \delta \cdot mean(ds(x_i)),\ \forall\, x_i \in D \\
\|x_i - x_{candidate,i}\| \geq S,\ \forall\, x_i \in D\ , \forall\, x_{candidate,i} \in G
\end{aligned}
\tag{D.1}
$$

where x_i is the existing sample points, $x_{grid,i}$ is the grid point on the evaluation grid, D is the design space, G is the evaluation grid, S is the space-filling metric, δ is the distance factor to be optimally determined along with G depending on a problem to be solved, and $x_{candidate,i}$ is the candidate sample point on the evaluation grid to fulfill S.

Eventually this process ensures all the selected candidate points are sufficiently far away from the existing sample points to avoid clustered sampling.

Separately, the LOO error in cross-validation, e_i^{LOO} is an error of the surrogate model prediction for an unsampled point in the Leave-One-Out Cross-Validation manner, indicating points of the surrogate model need to be improved by the cross-validation method. A large e_i^{LOO} at point $\boldsymbol{X}_i$ implies that the prediction of the surrogate model at the point is less-reliable; accordingly, more sampling points are needed to the region for improving accuracy (Liu et al., 2016).

In other words, the e_i^{LOO} is capable of capturing non-linear region, thus yielding a superior performance than the other design of experiments such as maximum entropy design method and maximum scaled distance method, for nine different test problems (Cai et al., 2017; Li et al., 2010).

Aute *et al.* (2013) defined the e_i^{LOO} expressed as

$$
e_i^{LOO} = \left| \frac{y(x_i) - \hat{y}_{D/x_i}(x_i)}{y(x_i)} \right|;\ x_i \in D \tag{D.2}
$$

where $y\,(x_i)$ is the true evaluation of objective function at point x_i , $\hat{y}_{D/x_i}\,(x_i)$ indicates the predicted objective value by the constructed RBF surrogate model using the whole sample points but x_i. Two different set of e_i^{LOO} are obtained on the sample points for each objective function.

Next, to merged with the exploration criteria, it is essential to predict e_i^{LOO} for any point in the design space in order for selecting the next sampling point.

Accordingly, each e_i^{LOO} for each objective function is mapped on the design space by using a separate RBF surrogate model. It is noteworthy that the RBF surrogate model used for approximating e_i^{LOO} is different from the RBF surrogate model to construct the objective function. For the sake of distinction, e_i^{LOO}, e^{LOO}, $\hat{e}_i^{LOO}$, $\hat{e}^{LOO}$ represent the LOO error at one sample point by the main RBF surrogate model, the collective expression of LOO error on the whole design space by the main RBF surrogate model, the LOO error at one sample point predicted by the separate surrogate model, and the collective expression of LOO error on the whole design space predicted by the separate surrogate model, respectively.

With the two criteria, e^{LOO} and S, the active-learning data sampling is carried out. The detailed steps of the procedure are presented in the following section. As an example, Figure D.2 shows the original test functions (Currin et al., 1988) to be constructed by the active-learning data sampling along with the RBF surrogate

model, also given in Equation D.3.

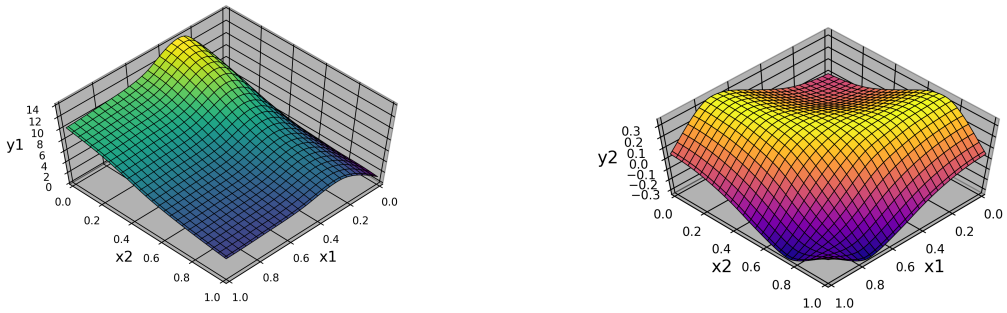

(a) (b)

Figure D.2: The original-test functions to be constructed by the active-learning data sampling along with the RBF surrogate model: (**a**) the first original test function, y_1 (**b**) the second original test function, y_2

$$y_1 = \left(1 - exp\left(\frac{-1}{2x^2}\right)\right) \frac{2300x_1^3 + 1900x_1^2 + 2092x_1 + 60}{100x_1^3 + 500x_1^2 + 4x_1 + 20};\ x_1, x_2 \in [0,1]$$
$$y_2 = \frac{sin\left(3\left(x_1^2 + x_2^2\right)\right)}{3};\ x_1, x_2 \in [0,1]. \tag{D.3}$$

Step 1: **Initial Sampling to Construct Each Initial RBF surrogate model for Each Objective Function**

Sample initial points arbitrarily in the design space and obtain each objective function value, y_1 and y_2 using Equation D.3 at the initial sample points. The RBF surrogate models are constructed based on the initial sample points as depicted in Figure D.3.

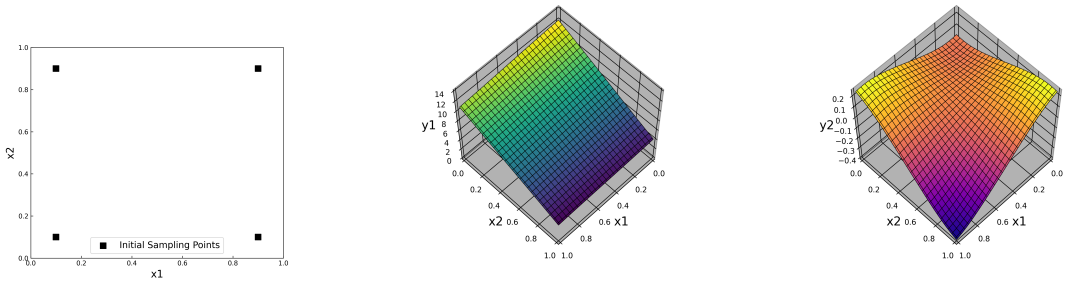

(a) (b) (c)

Figure D.3: (**a**) the initial sample points (**b**) Initial RBF surrogate model for y_1 (**c**) Initial RBF surrogate model for y_2

Step 2: **Exploitation**

Each e_i^{LOO} is evaluated on each sample point by Equation D.2. Then e_i^{LOO} is approximated on the entire design space by using a separate RBF surrogate model. The approximated values on the design space are the $\hat{e}^{LOO}$. This allows evaluations of e_i^{LOO} at any point in the design space, thus facilitating combination with the exploration for selecting the next sample points. Each $\hat{e}^{LOO}$ for each objective function is calculated as exhibited in Figure D.4.

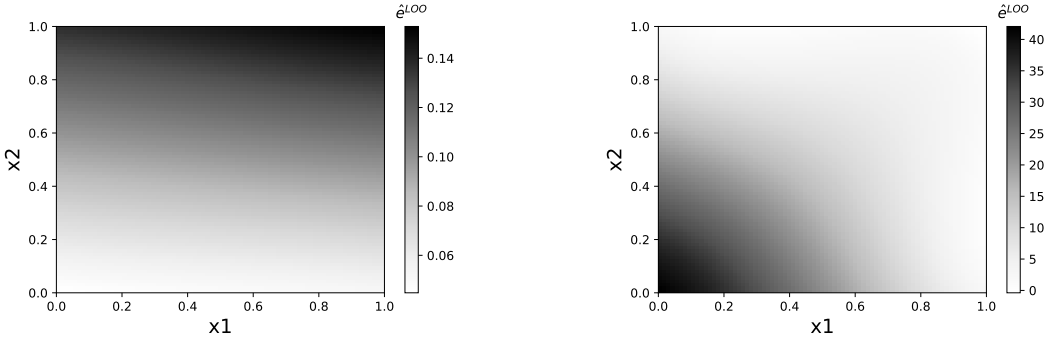

(a) (b)

Figure D.4: Exploitation result of the initial sample points: (**a**) $\hat{e}^{LOO}$ for y_1 over the design space (**b**) $\hat{e}^{LOO}$ for y_2 over the design space

Step 3: **Exploration**

The exploration process produces the $x_{candidate}$ according to Equation D.1 to be combined with the exploitation criteria for selecting the next sample points. Figure D.5 demonstrates the exploration process.

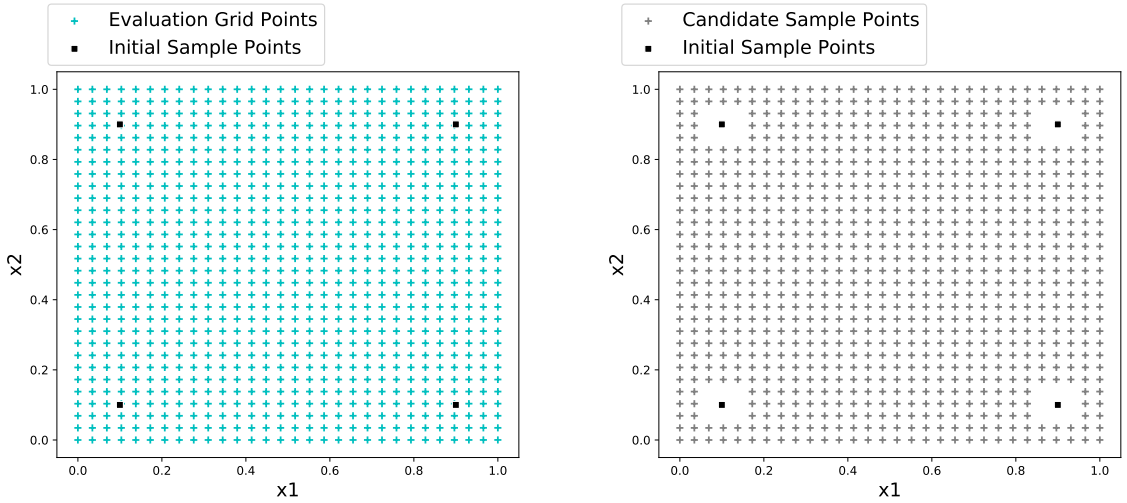

(a) (b)

Figure D.5: Exploration result with the initial sample points: (**a**) x_{grid} without applying S (**b**) $x_{candidate}$ with applying S

Step 4: **Determination of Next Sampling to Improve the Surrogate Model**

Using the developed exploitation and exploration criteria, the next sample points are determined; the largest $\hat{e}^{LOO}$ for each objective function is chosen among the candidate sample points that fulfill the exploration criteria, thus resulting in improvement of the surrogate model.

This step is illustrated in Figure D.6 and mathematically expressed as

$$\begin{aligned} x_{n+1} &= \arg \max_{x_{candidate}} \hat{e}^{LOO} \\ Subject\ to\ &||x_i - x_{candidate,i}|| \geq S, \forall x_i \in D, \forall x_{candidate,i} \in G. \end{aligned} \tag{D.4}$$

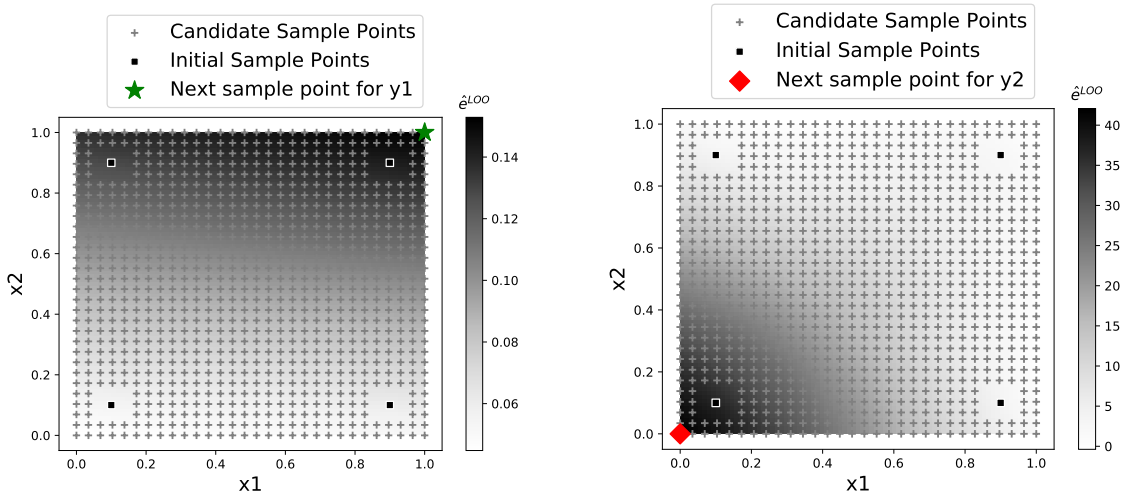

(a) (b)

Figure D.6: Next sample points by the exploration and the exploitation criteria from the initial sample points: (**a**) the next sample point for y_1 (**b**) the next sample point for y_2

Step 5: **Updates of the Surrogate Model**

Update each RBF surrogate model by evaluating each objective function on the updated sample points using Equation D.3. Figure D.7 describes the total sample points and the developed RBF surrogate model for each objective function after 40 evaluations.

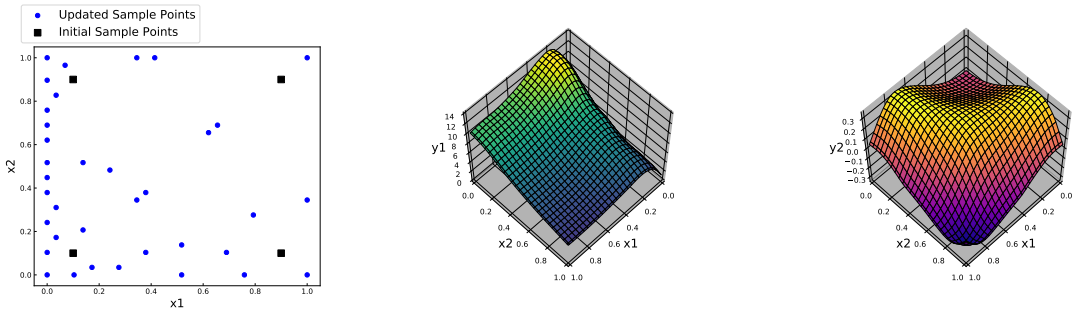

(a) (b) (c)

Figure D.7: The developed surrogate models by a total 40 evaluations of objective functions: (**a**) the total sample points used for developing the surrogate model (**b**) the developed surrogate model for y_1 (**c**) the developed surrogate model for y_2

Step 6: **Check the Stopping Criteria**

Stop developing surrogate models once the number of iteration reaches to the maximum iteration number determined by computer resources or a desirable accuracy of the surrogate model is achieved. The developed surrogate models are ready to be used for the multi-objective optimization utilizing the genetic algorithm.

APPENDIX E

EXPERIMENTAL CHARGE VALIDATION DATA FOR LOW-GWP REFRIGERANTS

This section details the charge calculation process and associated uncertainties. In order to calculate the final charge inside the RTPF, m_{RTPF} of interest, m_{RHXCT} is calculated differently depending on estimated m_{RHXCT} to account for the capacity of the load cell on the DMMS. When m_{RHXCT} is expected within the half of the limit of the load cell (1,000 g), m_{RHXCT} is given as Equation 3.2; whereas if the estimated m_{RHXCT} exceeds the half of the limit of the load cell, m_{RHXCT} is expressed as

$$m_{RHXCT} = \Delta m_{CW} + m_{\text{off}} - \Delta m_{TW} \tag{E.1}$$

where Δm_{CW} is a charge sampled weight of the RHXCT, Δm_{TW} is a tare weight of the RHXCT, and m_{off} is an offset weight, a standard mass, to offset the counter weight allowing an increase in measured charge range. Figure 2.22 illustrates the measurement process of Δm_{CW} and Δm_{TW} depending on the estimated charge weight to protect the load cell. The tests given in the test matrix employ Equation E.1 to calculate m_{RHXCT}, for initially those m_{RHXCT} were expected over the half of the limit of the load cell.

In either case, the counter weight should remain the same while measuring the Δm_{CW} and Δm_{TW} for obtaining the valid differential weights, Δm_{CW} and Δm_{TW}.

Separately, it is noted that, with the same charge inside the RHXCT m_{RHXCT}, Δm_{CW} and Δm_{TW} can change depending on the counter weight (*e.g.* if instrumentation or other mass is added to the RHXCT between tests). Table E.1 enumerates m_{RHXCT}, Δm_{CW}, Δm_{TW}, and other intermediate charge information as well as associated uncertainties.

Table E.1: Refrigerant charge data in the intermediate terms and the associated uncertainties

Test ID	$\mathbf{m_{RHXCT}}$ (g)	$\mathbf{u_{m,RHXCT}}$ ±(g)	$\mathbf{\Delta m_{CW}}$ (g)	$\mathbf{u_{\Delta m_{CW}}}$ ±(g)	$\mathbf{\Delta m_{TW}}$ (g)	$\mathbf{u_{\Delta m_{TW}}}$ ±(g)	$\mathbf{m_{off}}$ (g)	$\mathbf{u_{m,RSV}}$ ±(g)
yf-1	**1162**	**4.3**	797	3.1	635	2.9	1000.0	0.8
yf-2	**807**	**4.1**	920	2.9	613	2.9	500.0	0.6
yf-3	**567**	**5.7**	678	2.9	611	4.8	500.0	0.7
yf-4	**408**	**6.9**	318	3.6	411	5.9	500.0	0.4
yf-5	**448**	**6.6**	358	3.0	411	5.9	500.0	0.5
c-1	**682**	**4.5**	794	3.1	612	3.2	500.0	0.6
c-2	**547**	**5.1**	659	3.9	612	3.2	500.0	0.6
c-3	**405**	**4.1**	518	2.9	613	2.9	500.0	0.6
c-4	**416**	**4.1**	528	2.9	613	2.9	500.0	0.6
c-5	**486**	**4.5**	596	3.3	610	3.0	500.0	0.6

Uncertainty of m_{RHXCT}, $u_{m,RHXCT}$ is affected by the two charge measurements, Δm_{CW} and Δm_{TW}, as well as the uncertainty resulted from the actuation of RSVs, $u_{m,RSV}$; thus $u_{m,RHXCT}$ is given as

$$u_{m,RHXCT} = \sqrt{(u_{\Delta m_{TW}})^2 + (u_{\Delta m_{CW}})^2 + (u_{m,RSV})^2} \tag{E.2}$$

where $u_{m,RSV}$ is estimated by multiplying the refrigerant flow rate and a mean closing time difference, 0.02 sec, between the two RSVs; $u_{\Delta m_{TW}}$ is the uncertainty of Δm_{TW} and $u_{\Delta m_{CW}}$ is the uncertainty of Δm_{CW}. $u_{\Delta m_{TW}}$ is determined by a root sum squared of the measurement's random uncertainty and the maximum absolute error of the DMMS, 3.2 g (Lee, Bach and Bradshaw, 2021). $u_{\Delta m_{CW}}$ is also determined the same way as the $u_{\Delta m_{TW}}$. The uncertainty of m_{off} is ignored because of the negligible error of m_{off}, ±0.003 g the manufacturer reported.

m_{AUX} comprises a summation of multiple charges inside the RHXCT excluding m_{RTPF} according to each refrigerant state as presented in Figure E.1 and Equation E.3.

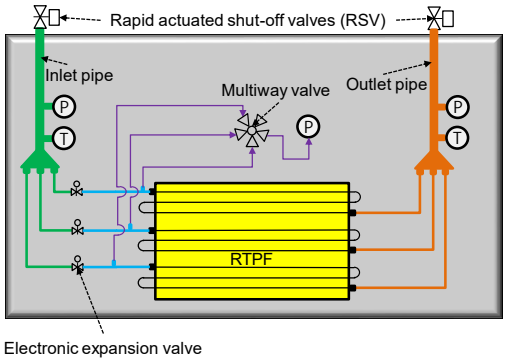

Color icon	Description of volume	Volume (ml)	Relative volume (-)	Uncertainty (ml)
	Subcooled liquid	48.8	0.01	0.1
	RTPF	4901	0.94	10.2
	Superheated vapor	145.4	0.03	0.3
	Superheated vapor in capillary pipe	8.0	0.00	-
	Two-phase	123.1	0.02	0.3
	Total	**5226**	**1.00**	**10.2**

Figure E.1: Internal-volume information of the RHXCT according to each refrigerant state

Figure E.1 contains the measurement information of the internal volume inside the RHXCT according to each refrigerant state.

$$m_{AUX} = m_{r,vap} + m_{r,vap,cap} + m_{r,liq} + m_{r,tp} \tag{E.3}$$

where $m_{r,vap}$ is the charge in superheated vapor state, $m_{r,liq}$ is the charge in subcooled liquid state, $m_{r,tp}$ is the charge in two-phase state, and $m_{r,vap,cap}$ is the charge inside capillary pipes assumed to be a saturated-vapor state. Those charges are estimated as the product of each density and volume: *e.g.* $m_{r,tp}$ is evaluated by using x_{in}, $P_{r,in}$, and the associated volume information given in Figure E.1. Those charges related in m_{AUX} and associated uncertainties are listed in Table E.2.

Table E.2: Refrigerant charge information in m_{AUX} and the associated uncertainties

Test ID	$\mathbf{m_{AUX}}$ (g)	$\mathbf{u_{m_{AUX}}}$ ±(g)	$\mathbf{m_{r,vap,cap}}$ (g)	$\mathbf{m_{r,liq}}$ (g)	$\mathbf{u_{m_{r,liq}}}$ ±(g)	$\mathbf{m_{r,vap}}$ (g)	$\mathbf{u_{m_{r,vap}}}$ ±(g)	$\mathbf{m_{r,tp}}$ (g)	$\mathbf{u_{m_{r,tp}}}$ ±(g)
yf-1	90	0.1	0.2	52.1	0.1	4.3	0.01	33.7	0.08
yf-2	73	0.1	0.3	49.9	0.1	4.5	0.01	18.8	0.05
yf-3	83	0.1	0.2	52.1	0.1	3.7	0.01	26.8	0.07
yf-4	67	0.1	0.2	49.9	0.1	3.8	0.01	13.3	0.03
yf-5	75	0.1	0.2	51.0	0.1	4.2	0.01	20.0	0.05
c-1	77	0.1	0.4	46.4	0.1	6.0	0.01	24.4	0.06
c-2	67	0.1	0.4	43.8	0.1	5.9	0.01	16.8	0.04
c-3	67	0.1	0.3	46.4	0.1	4.5	0.01	15.8	0.04
c-4	62	0.1	0.3	44.0	0.1	4.9	0.01	13.2	0.03
c-5	66	0.1	0.3	45.1	0.1	5.1	0.01	15.7	0.04

Uncertainty of m_{AUX}, $u_{m,AUX}$ is given as

$$u_{m,AUX} = \sqrt{(u_{m_{r,vap}})^2 + (u_{m_{r,liq}})^2 + (u_{m_{r,tp}})^2} \tag{E.4}$$

where the uncertainties of each state of refrigerant, $u_{m_{r,vap}}$,$u_{m_{r,liq}}$, and $u_{m_{r,tp}}$, are given using a relative measurement uncertainty of each volume corresponding to each state of refrigerant presented in Figure E.1. The following is an example for the uncertainty of vapor-refrigerant mass in the auxiliary charge inside RHXCT, $u_{m_{r,vap}}$:

$$u_{m_{r,vap}} = \frac{u_{V_{vap}}}{V_{vap}} \cdot m_{r,vap} \tag{E.5}$$

where $u_{V_{vap}}$ is the measurement uncertainty of the volume occupied by the vapor refrigerant in m_{AUX}, V_{vap} is the volume occupied by the vapor refrigerant in m_{AUX}, and $m_{r,vap}$ is the vapor-refrigerant mass in m_{AUX}. Given the small amount of mass inside $m_{r,vap,cap}$, the uncertainty of vapor charge inside the capillary pipe, $u_{m_{r,vap,cap}}$ is neglected.

Based on the obtained intermediate charge information, m_{RTPF} is calculated according to Equation 3.1. The uncertainty of m_{RTPF}, $u_{m_{RTPF}}$ is defined as

$$u_{m,RTPF} = \sqrt{(u_{m_{RHXCT}})^2 + (u_{m_{AUX}})^2}. \tag{E.6}$$

Table 3.5 also presents m_{RTPF}, $u_{m_{RTPF}}$, and $u_{m,rel_{RTPF}}$, relative uncertainty of m_{RTPF}.

This section presents the complete information of the experimental data as summarized in Table E.3.

Table E.3: Experimental information of R1234yf and R468C tests

Test ID	$\mathbf{P_{atm}}$	$\mathbf{T_{db,i}}$	$\mathbf{T_{wb,i}}$	$\mathbf{\dot{m}_{air}}$	$\mathbf{\dot{m}_r}$	$\mathbf{x_{in}}$	$\mathbf{P_{r,i}}$	$\mathbf{P_{r,o}}$	$\mathbf{T_{r,o}}$	$\mathbf{\Delta T_{sh}}$	$\mathbf{T_{r,sat,o}}$	$\mathbf{\dot{Q}_r}$	$\mathbf{\dot{Q}_a}$	$\mathbf{m_{RTPF}}$
	kPa	°C	°C	kg/s	kg/h	-	kPa	kPa	°C	K	°C	kW	kW	g
yf-1	97.5	26.5	14.8	0.971	136.9	0.096	611	543	20.7	3.4	17.3	5.14	4.89	1072
yf-2	97.7	26.6	14.6	0.976	113.5	0.202	627	577	24.4	5.1	19.3	3.82	3.71	733
yf-3	97.6	26.7	14.4	0.974	131.7	0.119	565	484	23.6	10.1	13.5	5.09	5.22	484
yf-4	97.9	26.7	15.0	0.964	80.8	0.248	522	496	23.9	9.7	14.3	2.76	2.68	341
yf-5	98.0	26.7	14.7	0.961	81.6	0.172	573	541	24.5	7.3	17.2	2.95	2.96	372
c-1	97.9	26.7	14.5	0.652	109.9	0.167	1156	1119	22.1	4.2	18.0	5.40	5.14	605
c-2	97.8	26.7	15.2	0.650	107.4	0.258	1151	1105	22.3	4.8	17.5	4.74	4.57	480
c-3	97.9	26.7	14.5	0.652	107.1	0.216	926	879	19.8	10.0	9.8	5.37	5.38	338
c-4	98.0	26.7	15.3	0.655	106.8	0.285	983	939	20.8	8.9	12.0	4.83	4.84	353
c-5	97.8	26.7	14.6	0.650	112.6	0.242	1020	972	20.8	7.6	13.2	5.29	5.40	419

Table E.4: Experimental information of R410A tests

Variable	**Unit**	**Minimum value**	**Maximum value**
P_{atm}	kPa	96.3	97.9
$T_{db,i}$	°C	8.3	13.3
$T_{wb,i}$	°C	3.4	7.2
$\dot{m}_{air}$	kg/s	0.665	1.075
$\dot{m}_r$	kg/h	51.5	181.4
x_{in}	-	0.225	0.284
$P_{r,i}$	kPa	747	928
$P_{r,o}$	kPa	732	872
$T_{r,o}$	°C	2.1	6.9
ΔT_{sh}	K	2.4	7.4
$T_{r,sat,o}$	°C	-2.5	3.0
$\dot{Q}_r$	kW	2.40	8.33
$\dot{Q}_{air}$	kW	2.38	8.10
m_{RTPF}	g	299	843
T_{liquid}	°C	32.2	39.1

The descriptions of the ANN is presented in Table E.5.

Table E.5: ANN information

Number of neurons per each hidden layer	3
Number of hidden layers	3
Activation function	Tanh
Number of epochs	200
Batch size	6
Learning rate	0.09
Stochastic optimizer	Adam (Kingma and Ba, 2014)
ANN library	Keras (Chollet et al., 2015)

Table E.6: ANN weights(w) and biases(b)

	Neuron unit (j)	$\mathbf{w_{1j}}$	$\mathbf{w_{2j}}$	$\mathbf{w_{3j}}$	**b**
1st layer	1	-0.8445	-1.2958	-	1.1731
	2	-1.6871	-0.3943	-	1.0525
	3	-0.3633	-0.8196	-	0.7088
2nd layer	1	0.0733	0.6806	0.1089	0.3877
	2	-0.0919	0.1306	0.1545	0.1026
	3	1.0094	0.8801	0.7267	0.2087
3rd layer	1	-0.1094	0.1294	0.0685	0.0005
	2	0.2906	0.0331	0.6901	0.1189
	3	-0.3133	-0.2543	-0.1037	-0.2106
4th layer	1	-0.0270	0.0848	-0.1806	0.2731

VITA

Abraham Juseok Lee

Candidate for the Degree of

Doctor of Philosophy

Dissertation: AN EXPERIMENTALLY VALIDATED HEAT EXCHANGER REFRIGERANT CHARGE MODEL AND OPTIMIZATION OF REFRIGERANT CHARGE FOR A HEAT PUMP

Major Field: Mechanical and Aerospace Engineering

Biographical:

Education:
Completed the requirements for the Doctor of Philosophy in Mechanical and Aerospace Engineering at Oklahoma State University, Stillwater, Oklahoma in May, 2023.

Completed the requirements for the Master of Science in Mechanical Engineering at Korea University, Seoul, South Korea in 2010.

Completed the requirements for the Bachelor of Science in Mechanical Engineering at Korea University, Seoul, South Korea in 2008.

Experience:
Senior Research Engineer at LG Electronics, Jan. 2012 - July. 2017
Research Engineer at Seoul Semiconductor, Jan. 2010 - Oct. 2011

Professional Memberships:
Student member in American Society of Heating, Refrigerating, and Air-conditioning Engineers.